

University of Kentucky

UKnowledge

Theses and Dissertations--Chemistry

Chemistry

2020

UNCOVERING STRUCTURE-PROPERTY RELATIONSHIPS OF INORGANIC NANOMATERIALS VIA TRANSMISSION ELECTRON MICROSCOPY

Melonie Thomas

University of Kentucky, melonie.thomas@uky.edu

Author ORCID Identifier:

 <https://orcid.org/0000-0002-5264-1921>

Digital Object Identifier: <https://doi.org/10.13023/etd.2020.326>

[Right click to open a feedback form in a new tab to let us know how this document benefits you.](#)

Recommended Citation

Thomas, Melonie, "UNCOVERING STRUCTURE-PROPERTY RELATIONSHIPS OF INORGANIC NANOMATERIALS VIA TRANSMISSION ELECTRON MICROSCOPY" (2020). *Theses and Dissertations--Chemistry*. 128.

https://uknowledge.uky.edu/chemistry_etds/128

This Doctoral Dissertation is brought to you for free and open access by the Chemistry at UKnowledge. It has been accepted for inclusion in Theses and Dissertations--Chemistry by an authorized administrator of UKnowledge. For more information, please contact UKnowledge@lsv.uky.edu.

STUDENT AGREEMENT:

I represent that my thesis or dissertation and abstract are my original work. Proper attribution has been given to all outside sources. I understand that I am solely responsible for obtaining any needed copyright permissions. I have obtained needed written permission statement(s) from the owner(s) of each third-party copyrighted matter to be included in my work, allowing electronic distribution (if such use is not permitted by the fair use doctrine) which will be submitted to UKnowledge as Additional File.

I hereby grant to The University of Kentucky and its agents the irrevocable, non-exclusive, and royalty-free license to archive and make accessible my work in whole or in part in all forms of media, now or hereafter known. I agree that the document mentioned above may be made available immediately for worldwide access unless an embargo applies.

I retain all other ownership rights to the copyright of my work. I also retain the right to use in future works (such as articles or books) all or part of my work. I understand that I am free to register the copyright to my work.

REVIEW, APPROVAL AND ACCEPTANCE

The document mentioned above has been reviewed and accepted by the student's advisor, on behalf of the advisory committee, and by the Director of Graduate Studies (DGS), on behalf of the program; we verify that this is the final, approved version of the student's thesis including all changes required by the advisory committee. The undersigned agree to abide by the statements above.

Melonie Thomas, Student

Dr. Beth S. Guiton, Major Professor

Dr. Yinan Wei, Director of Graduate Studies

UNCOVERING STRUCTURE-PROPERTY RELATIONSHIPS OF INORGANIC
NANOMATERIALS *VIA* TRANSMISSION ELECTRON MICROSCOPY

DISSERTATION

A dissertation submitted in partial fulfillment of the
requirements for the degree of Doctor of Philosophy in the
College of Arts and Sciences
at the University of Kentucky

By
Melonie P. Thomas
Lexington, Kentucky
Director: Dr. Beth S. Guiton, Professor of Chemistry
Lexington, Kentucky
2020

Copyright © Melonie P. Thomas 2020
<https://orcid.org/0000-0002-5264-1921>

ABSTRACT OF DISSERTATION

UNCOVERING STRUCTURE-PROPERTY RELATIONSHIPS OF INORGANIC NANOMATERIALS *VIA* TRANSMISSION ELECTRON MICROSCOPY

The rapid increase of research in nanoscale devices and nanotechnology in the past few decades has revealed that nanomaterials may possess exceptional properties that are significantly different from the bulk counterpart, due to local rearrangements of the atoms at surfaces and defects. Transmission electron microscopy (TEM) is an indispensable tool when it comes to the characterization of nanomaterials, primarily due to its ability to resolve the local-structure of materials at the atomic-scale. To study dynamic processes, however, regular TEM experiments are inadequate, as they provide only before and after information rather than the real-time data essential to understanding a reaction or phase-transformation mechanism. This dissertation describes developments and applications of high-resolution and *in situ* TEM techniques to track the atomic rearrangements of nanomaterials in real-time, to determine the structure-property relationships of nanomaterials as they change during structural-transformations such as chemical reactions.

The four chapters in this dissertation will focus on the synthesis and characterization of nanomaterials with unique properties. The first project concentrates on designing a novel synthesis method to control the morphology of iron(II) sulfide (FeS) nanoplatelets by varying the starting material (Fe source) or the surfactant employed in the hydrothermal synthesis. The following three chapters cover detailed TEM analyses of three distinctive nanomaterials: catalytic hetero-atom doped carbon nano-onions, thermoelectric $\text{La}_{3-x}\text{Te}_4$ with Ni nanoparticle inclusions, and dielectric cubic HfO_2 . The work presented here gives insights on a novel morphology-controlled hydrothermal synthesis of FeS nanoplatelets and demonstrates the utilization of advanced electron microscopic techniques such as aberration-corrected TEM/Scanning TEM (STEM) and *in situ* TEM, to elucidate structure-property relationships of nanomaterials in atomic-resolution and in real-time.

KEYWORDS: transmission electron microscopy, TEM, STEM, *in situ*, structure-property relationship

Melonie P. Thomas

05/19/2020

Date

UNCOVERING STRUCTURE-PROPERTY RELATIONSHIPS OF INORGANIC
NANOMATERIALS *VIA* TRANSMISSION ELECTRON MICROSCOPY

By
Melonie P. Thomas

Dr. Beth S. Guiton

Director of Dissertation

Dr. Yinan Wei

Director of Graduate Studies

05/19/2020

Date

DEDICATION

To

My mom and late dad
for their endless love, encouragement, and countless sacrifices
for being my greatest source of happiness and inspiration

My husband Roshein
for being my strength
for his constant support in pursuing my dreams
for being my best friend and critique

My brother Arun
for his continuous love and support

My advisor Dr. Beth Guiton
for her invaluable mentorship
for making me the researcher I am today

ACKNOWLEDGMENTS

I would like to convey my heartfelt gratitude to Dr. Beth Guiton, my advisor, mentor, and inspiration, for the guidance and encouragement in this endeavor. I joined grad school with a background in organic chemistry and was quite tentative when Dr. Guiton introduced me to the fields of electron microscopy and solid-state chemistry. At the time of completing this dissertation, however, I feel that I have made this field my own and found my passion in the world of material sciences. The opportunity to work at ORNL was indeed the highlight of my doctoral studies. Dr. Guiton encouraged me to take autonomy in my research work and was always there to provide guidance and support whenever needed. She has been a caring friend and an outstanding role model in life outside the lab. Thank you, Beth, for molding me to be a strong woman not only in science but in life as well.

I would also like to thank my dissertation advisory committee members, Dr. Selegue, Dr. Graham, and Dr. Strachan, for the stimulating and constructive feedback, which proved essential in submitting a successful thesis. Furthermore, my sincere thanks to the staff of the UK Chemistry department, who were always happy to assist me, especially Jenny and Christine. I take this opportunity to congratulate the team for the fantastic support systems, which allows students to solely focus on their graduate studies.

Most of my research time was spent at ORNL, and I would like to express my gratitude to the incredible staff scientists, Dr. Karren More, Dr. David Cullen, Dr. Andrew Lupini, Dr. Juan-Carlos Idrobo, and Dr. Raymond Unocic, for taking time out of their busy schedules to train me on state-of-the-art microscopes and help me with troubleshooting whenever I run into issues during microscopy sessions. Special thanks to

Dr. David Cullen for the friendly guidance, Dr. Karren More for being a fantastic mentor, and Dr. Beth Hudak for always being there for me at ORNL, not only as a senior lab mate but a caring friend as well. Facility staff technicians, Shawn and Dorothy, for taking care of me at all times. To Drs. Chanaka Kumara and Buddhika Liyanage for the support and for being my family in Tennessee. I would like to express my gratitude to the UK EMC staff, especially Dr. Qian and Dr. Briot for their invaluable assistance with TEM and FIB-SEM experiments. I could not stress enough how lucky I was to have had the best lab mates and friends through-out grad school. They were my family away from home and the safety net for me to fall back whenever I was down. I will cherish the lovely memories forever.

Finally, my family. I feel honored and proud to be a first-generation graduate student. Dad, I wish you were here with us to see your dream come true. I hope I made you proud. Mom, my husband Roshein, and my little brother Arun for the constant support and sacrifices you have made, to see me pursue my dream. Love you all. This is for you!

TABLE OF CONTENTS

ACKNOWLEDGMENTS	iii
LIST OF TABLES	vii
LIST OF FIGURES	viii
CHAPTER 1.INTRODUCTION	1
1.1 Motivation	1
1.2 Synthesis of two-dimensional nanosized transition metal chalcogenides.....	4
1.2.1 Introduction.....	4
1.2.2 Hydrothermal synthesis	5
1.3 Transmission electron microscopy	7
1.3.1 Introduction.....	7
1.3.2 Z-contrast imaging.....	10
1.3.3 Aberration correction	11
1.3.4 Fourier filtering.....	12
1.3.5 Energy-dispersive X-ray spectroscopy	14
1.3.6 Electron energy loss spectroscopy	15
1.3.7 <i>In situ</i> TEM.....	16
CHAPTER 2.METHODS.....	19
2.1 Sample synthesis	19
2.1.1 Hydrothermal synthesis of FeS nanoplatelets.....	19
2.1.2 S-, N-, and, NS-CNO	20
2.1.3 Synthesis of cubic HfO ₂ and HfV ₂ O ₇	22
2.2 TEM/STEM sample preparation	25
2.2.1 Sample preparation on a 300 mesh TEM Cu grid.....	25
2.2.2 Sample preparation on a Protochips® heating e-chip.....	26
2.2.3 Nion UltraSTEM 100 (U100).....	26
2.2.4 Air sensitive La _{3-x} Te ₄ -Ni sample pellets.....	26
2.3 Characterization	30
2.3.1 Powder X-ray diffraction (PXRD).....	30
2.3.2 Scanning electron microscopy	33
2.3.3 Transmission electron microscopy	35
2.3.4 Catalytic activity determination.....	38
2.3.5 X-ray Photoelectron Spectroscopy	40

CHAPTER 3.MORPHOLOGY CONTROLLED HYDROTHERMAL SYNTHESIS OF IRON(II) SULFIDE NANOPATELETS	41
3.1 <i>Introduction</i>	41
3.2 <i>FeS Nanoplatelets</i>	44
3.3 <i>Conclusion</i>	54
CHAPTER 4.DIRECT IMAGING OF HETEROATOM DOPANTS IN CATALYTIC CARBON NANO-ONIONS.....	55
4.1 <i>Introduction</i>	55
4.2 <i>S-, N-, and, NS-CNO</i>	58
4.3 <i>Conclusions</i>	72
CHAPTER 5.UNCOVERING THE STRUCTURE AND STABILITY OF THERMOELECTRIC LANTHANUM(IV) TELLURIDE-NICKEL COMPOSITES USING HIGH-RESOLUTION AND <i>IN SITU</i> TEM	73
5.1 <i>Introduction</i>	73
5.2 <i>Structure and stability of thermoelectric $La_{3-x}Te_4-Ni$ composites</i>	78
5.3 <i>Conclusions</i>	89
CHAPTER 6.STABILIZATION OF METASTABLE CUBIC HAFNIA AND HAFNIUM PYROVANADATE FROM CORE-SHELL ARRANGEMENT OF PRECURSORS	90
6.1 <i>Introduction</i>	90
6.2 <i>Stabilizing metastable cubic HfO_2 from a core-shell nanorod precursor</i>	92
6.3 <i>Conclusions</i>	102
REFERENCES	103
VITA.....	120

LIST OF TABLES

Table 2.1 Operating conditions of transmission electron microscopes used.	35
Table 2.2 The EDS systems used in the present work.	38
Table 3.1 Summary of starting material and surfactant effect on platelet diagonal, thickness, and shape of FeS nanoplatelets.	46
Table 3.2 Rietveld analysis of powder x-ray diffraction pattern of iron sulfide samples synthesized using different ligand and iron sources.	50
Table 4.1 Dopant configuration and location on CNOs.	62
Table 4.2 Quantitative analysis of NS-CNO.	62
Table 4.3 Quantitative analysis of S-CNO.	64
Table 4.4 Quantitative analysis of N-CNO.	64

LIST OF FIGURES

Figure 1.1 Disassembled parts of the hydrothermal reactor and the Teflon liner.....	5
Figure 1.2 The interaction of the electron beam with the sample.....	7
Figure 1.3 Two principle imaging modes of TEM operation	8
Figure 1.4 A comparison of a perfect lens (a) with lenses with spherical (b) and chromatic (c) aberrations.	11
Figure 1.5 Generation of characteristic X-rays.....	14
Figure 1.6 An EELS spectrum illustrating the zero-loss peak, the low-loss, and the high-loss regions.....	15
Figure 2.1 FIB sample preparation for TEM/ <i>in situ</i> TEM.....	27
Figure 2.2 Air Protection (AP) holder compatible with both Hitachi FIB-SEM and TEM/STEM systems.....	29
Figure 2.3 Diagram of Bragg’s Law	30
Figure 2.4 The powder X-ray diffraction method.....	31
Figure 2.5 The schematic diagram of a scanning electron microscope	33
Figure 2.6 Ewald sphere construction.....	36
Figure 3.1 SEM images of FeS nanoplatelets.....	45
Figure 3.2 The platelet diagonal and thickness distribution histograms of the FeS platelets calculated by ImageJ® software.....	47
Figure 3.3 Rietveld refined PXRD pattern of the as-synthesized FeS sample from FeCl ₂ and DETA.. ..	48
Figure 3.4 FeCl ₃ DETA, (b) FeCl ₂ TEPA, (c) FeCl ₃ TEPA, (d) FeCl ₂ TETA and (e) FeCl ₃ TETA. T.....	49
Figure 3.5 TEM characterization of FeS nanoplatelets.	51
Figure 3.6 EDS analysis of an FeS nanoplatelet (sample D2).....	51
Figure 3.7 XPS spectra of FeS synthesized from FeCl ₂ using DETA surfactant (D2).....	52
Figure 4.1 HRSTEM images of CNO with heteroatom dopants	57
Figure 4.2 Fourier filtered HAADF image indicating single and grouped dopant atoms (yellow circles) in a N-CNO	59
Figure 4.3 Defect sites in CNO.....	60
Figure 4.4 EEL spectroscopy.....	60
Figure 4.5 Filtered IFFT images showing defects in CNO shells.....	61
Figure 4.6 STEM micrographs of pristine CNOs	66
Figure 4.7 Line scan across C and S atoms in S-CNO sample (HAADF image).....	67
Figure 4.8 Histograms of dopant proximity and configuration in the three CNO samples.. ..	67
Figure 4.9 Proximity to defect site histogram with equal bin size (0.01 nm).....	68
Figure 4.10 Determination of ORR activity by RRDE experiments.	69
Figure 5.1 Sample preparation.....	78

Figure 5.2 EDS spectrum of Figure 1 (d-g) showing the presence of La, Te, and Ni in the $\text{La}_{3-x}\text{Te}_4\text{-Ni}$ sample.....	79
Figure 5.3 EDS line scan across the interface of $\text{La}_{3-x}\text{Te}_4$ matrix and Ni particle.....	80
Figure 5.4 High-resolution TEM characterization of the $\text{La}_{3-x}\text{Te}_4\text{-Ni}$ interface.	80
Figure 5.5 Epitaxial relationship between $\text{La}_{3-x}\text{Te}_4$ and Ni at the $\text{La}_{3-x}\text{Te}_4/\text{Ni}$ interface. .	81
Figure 5.6 <i>In situ</i> TEM study of a pristine (non-oxidized) $\text{La}_{3-x}\text{Te}_4\text{-Ni}$ sample.	83
Figure 5.7 <i>In situ</i> TEM study of an oxidized $\text{La}_{3-x}\text{Te}_4\text{-Ni}$ sample.	84
Figure 5.8 <i>In situ</i> TEM study of a partially oxidized $\text{La}_{3-x}\text{Te}_4\text{-Ni}$ sample.....	85
Figure 5.9 <i>In situ</i> TEM study of the partially oxidized $\text{La}_{3-x}\text{Te}_4\text{-Ni}$ sample (same area as Figure 5.8 or small area in the blue box shown in the figure 5.8a).	87
Figure 5.10 Two EDS spectra representing two areas from the ROI of the partially oxidized $\text{La}_{3-x}\text{Te}_4\text{-Ni}$ sample in Figure 6(a).....	88
Figure 6.1 Schematic depiction of the synthesis of cubic HfO_2 and HfV_2O_7 from VO_2 and HfO_2 precursors arranged in a core–shell arrangement.	94
Figure 6.2 Imaging and compositional mapping of $\text{V}_2\text{O}_3@\text{HfO}_2$ core–shell structures. .	95
Figure 6.3 Cross-sectional TEM image and EDS line scan of an ultramicrotomed $\text{V}_2\text{O}_3@\text{HfO}_2$ core-shell nanowire.	96
Figure 6.4 The interface of HfO_2 and V_2O_3	97
Figure 6.5 TEM images and accompanying FFTs corresponding to <i>in situ</i> heating of $\text{HfO}_2@\text{VO}_2$ core–shell particles.	98
Figure 6.6 Stabilized cubic hafnia.	99

CHAPTER 1. INTRODUCTION

1.1 Motivation

The design and synthesis of nanomaterials and nanotechnology itself are exclusively determined by the ability of the analytical instrumentation, tools, and approaches to synthesize, characterize, and manipulate the material at the nanoscale. Scaling of material to the nano regime provides a basis for the emergence of unique and novel properties in nanomaterials that are distinctive from the bulk counterpart.^{1,2} Owing to this size confinement, high-temperature metastable and thermodynamic phases with remarkable characteristics have become accessible at much lower temperatures than the bulk phase transition temperatures. Recent studies on HfO₂ reported scaling the material to ultrasmall dimensions of ~4 nm, as an approach to trap the high-temperature tetragonal phase of HfO₂ with a high dielectric constant ($\kappa=75$), which is otherwise accessible only in the temperatures above 1720 °C.^{3,4} Hudak *et al.* revealed that the size confinement and twin boundaries in the HfO₂ nanorod contribute towards stabilizing the metastable tetragonal phase kinetically.⁴ Chen *et al.* showed the coexistence of low-temperature (β -phase) and high-temperature (α -phase) in a nanosized wedge-shaped Cu₂Se single crystal, which according to Landau theory is impossible in bulk. Even though the surface and shape effects in an infinite bulk material are neglected in Landau theory, in a Cu₂Se single crystal with a nanosized thickness, these surface effects aid in driving α to β phase transition. This second-order phase transformation initiates at a low temperature of 383 K and is dependent on the thickness of the nanocrystal whereas the phase transition temperature of bulk is 400 K.⁵

Given that the structure often dictates the physical properties of a nanomaterial, a careful understanding of the structure is vital to design materials with superior properties suitable for desired applications. To fully uncover the structure of a crystalline solid, one should pay close attention to the crystal structure, atomic arrangement within the crystal, defects or impurities present, and the microstructure (such as grain boundaries, surfaces, interfaces, and chemical composition). Diffraction techniques-such as powder X-ray diffraction (PXRD) and neutron diffraction- often provide information on the average crystal structure or the sample as a whole. To explore the local structural aspects of a crystalline nanomaterial whose intrinsic structural details are modified at nanoscale-such as the atomic arrangement, defects and impurities in the crystal structure- transmission electron microscopy (TEM) is used.⁶

TEM is an indispensable and versatile material characterization technique that provides a high-resolution analysis of the local structure and the composition of the material at the nanometer or even at the atomic scale. When paired with other complementary characterization methods equipped in the instrumentation, such as electron energy-loss spectroscopy (EELS), energy-dispersive X-ray spectroscopy (EDS), and selected area electron diffraction (SAED), TEM can offer a complete characterization of materials. As advancements in this particular field, the state-of-the-art aberration-corrected scanning transmission electron microscopes (STEM) allows the imaging of atomically resolved columns of a crystalline solid and the high-angle annular dark-field (HAADF) detectors provide the opportunity for Z-contrast imaging where the intensities in the STEM HAADF micrograph can be directly correlated to the atomic numbers of elements present.⁶⁻⁸

Even though the *ex situ* characterization methods provide an insight into the structure of a material “before” and “after” a chemical reaction or a phase transformation, *in situ* techniques are needed to resolve mechanistic in-between steps to get a complete idea of the whole reaction or transformation process. For example, diffraction techniques- such as PXRD or SAED- can be used to identify the phase of the material before the experiment and after heating to the transition temperature where the phase transformation occurs. The use of a technique like *in situ* PXRD can help to identify the temperature range at which the phase transformation initiates, which could be significantly different from its bulk phase transition temperature.⁹ It should be noted that the *in situ* PXRD studies reveal information on the average structure or the whole sample.

When the necessity arises for the understanding of salient features of mechanistic steps of a critical reaction or a phase transformation, *in situ* TEM provides a way to monitor changes in the local structure - such as the movement and rearrangement of atoms, dynamic changes in the crystal lattice - as a function of temperature, as they evolve in time. *In situ* TEM techniques allows studying the material behavior from room temperature to elevated temperatures as high as 1200 °C in high vacuum conditions, or controlled gas or liquid environments. The vital information obtained by *in situ* TEM studies abets in filling gaps in understanding significant reaction and transformation mechanisms in nanocrystals, which may otherwise prove inaccessible.^{1,5,9-12}

1.2 Synthesis of two-dimensional nanosized transition metal chalcogenides

1.2.1 Introduction

Nanostructured transition metal chalcogenides have gained significant attention due to their enhanced optical, electronic, transport, and magnetic properties. During the past decade, metal chalcogenides with varied morphologies and sizes have led to tremendous applications in materials science including sensors, solar cells, light-emitting diodes, thermoelectric devices, lithium-ion batteries, and memory devices.¹³⁻¹⁵ When the size of these materials are scaled down to the nanometer level, new and enhanced chemical and physical properties are observed, compared with its bulk counterpart.¹⁶ Iron chalcogenides have been extensively studied due to their outstanding magnetic and transport properties, which can be tuned readily by defect, size, and shape control in the nanophase. Further, the conducting properties of these iron chalcogenides can vary from semiconducting to superconducting, opening a broad range of applications from biomedical to electronic.^{13,16}

The design and choice of the synthesis method are of significant importance to obtain better control over the morphology of the resulting nanomaterials with specific applications. Among the various synthetic pathways reported in the literature for iron chalcogenides synthesis, wet chemical methods such as hydrothermal synthesis have drawn much attention due to the many advantages it holds when compared with other synthesis methods.^{17,18} The use of surfactants in hydrothermal synthesis avoids particle agglomeration, thus, provides better control over the shape and size of the resulting nanomaterial. In addition, surfactants are also able to control the growth direction of the nanomaterial by manipulating the surface adsorption of crystal planes preferentially.^{19,20}

1.2.2 Hydrothermal synthesis

Solvothermal/hydrothermal reaction process is defined as a chemical reaction occurring at temperatures above room temperature and high-pressure conditions in a solvent contained in a closed container. The terms solvothermal and hydrothermal are referred to when the solvent being used is a non-aqueous solvent and water, respectively. The first reported hydrothermal synthesis was performed by Schafthaul in 1845, to grow



Figure 1.1 Disassembled parts of the hydrothermal reactor and the Teflon liner.

Quartz nanocrystals. In the 1900s, hydrothermal reactions achieved significant progress with the development of high-resolution microscopes and nanomaterial synthesis. Since

then, the hydrothermal process has gained a great interest in synthesizing highly crystalline nanomaterials with controlled size and morphology.^{21,22}

In hydrothermal synthesis, supercritical fluids provide outstanding reaction medium, allowing variation of equilibrium and reaction rates. Near the critical point, the fluids have different properties than those of under ambient conditions. The shift in the dielectric constant and solvent densities with pressure and temperature results in increased supersaturation, increased rates of nucleation of the particles, leading to reduced particle sizes.^{18,23} Due to the variation of the equilibrium with the temperature, particles formed at low temperatures dissolve and recrystallize at elevated temperatures, which are relatively insoluble under normal conditions. The advantages of the hydrothermal method over other synthetic routes include low process temperatures, low production cost, low energy consumption, control of products, large scale production, and environmentally benign.^{18,24} The hydrothermal reactor is a pressure vessel which is used to perform hydrothermal reactions at high temperature and high pressure. The reactor comprises of two parts, the outer metal autoclave and the inner Teflon liner (Figure 1.1). The Teflon liner prevents the corrosion of the autoclave by chemicals. Characteristics of an ideal hydrothermal reactor include inertness to the chemical being used, easy to assemble and disassemble, leak-proof, should withstand high temperature and pressure for a long time. When choosing a reactor, the corrosive resistance of the autoclave material, operating conditions of the reaction should be taken into consideration.¹⁸

1.3 Transmission electron microscopy

1.3.1 Introduction

The transmission electron microscope (TEM) is a central tool in material science to study the atomic-scale structure of materials. It uses high energy electrons to study defects, crystal structure, lattice parameters, and chemical composition of the material of interest. The instrument comprises three systems. The illumination system located at the top of the microscope produces high energy electrons (100-400 keV) and directs them towards the sample stage and the objective lens, with a set of condenser lenses and apertures. There are two types of electron sources, thermionic guns, and field emission guns. Thermionic guns are less expensive than field emission guns and more commonly used in TEMs. Field emission guns are used when high-resolution imaging is needed.

At the sample stage, electrons interact with the sample, and the resulting electrons form an image that is magnified on to the screen by the projection system (Figure 1.2). The

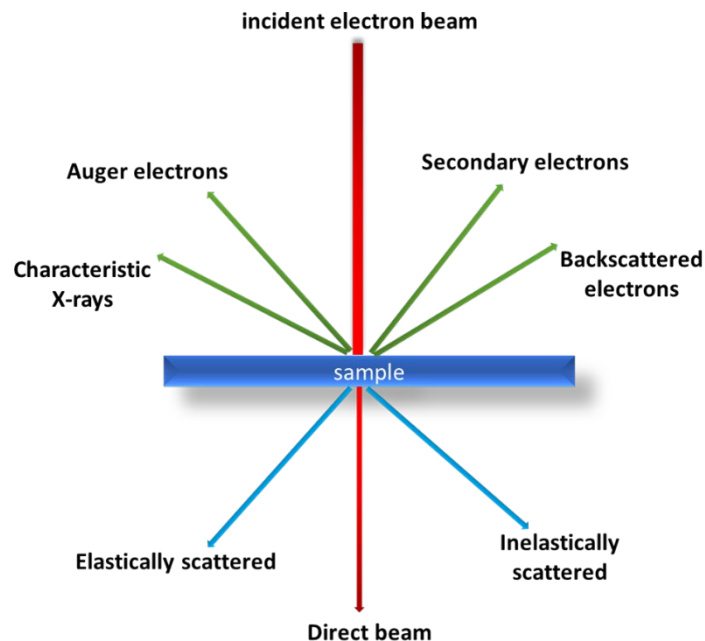


Figure 1.2 The interaction of the electron beam with the sample.

phosphorescent screen, which is located at the bottom of the microscope illuminates when electrons hit. The image is displayed on the screen and viewed through a glass screen.

In TEM, there are two principal modes of operation (Figure 1.3). In image mode, the objective lens gathers electrons resulting from sample-electron beam interactions and forms an image of the sample at the image plane. While in diffraction mode, the objective lens creates a diffraction pattern at the back focal panel of the lens. It is always possible to switch between these modes by focusing the intermediate lens on to the image plane or the back focal plane of the lens. The resolution of a TEM can be interpreted as the smallest distance that can be resolved (δ) and is given by the following equation (1.1):

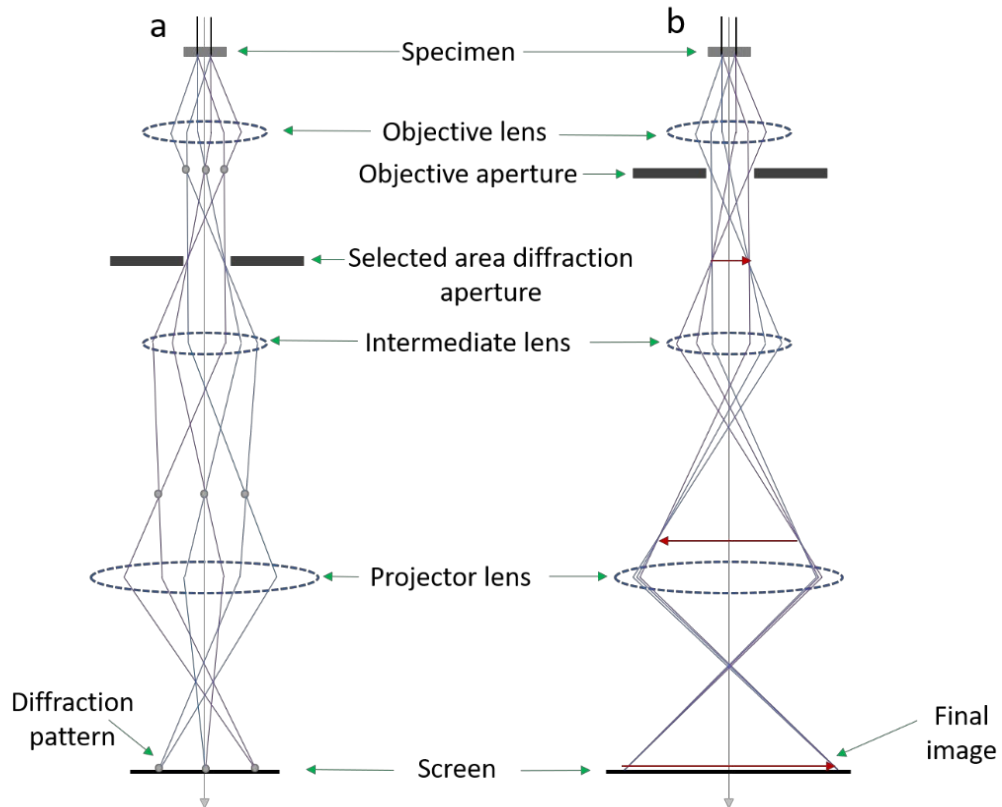


Figure 1.3 Two principle imaging modes of TEM operation (a) diffraction mode (b) imaging mode (reproduced with permission from Williams and Carter (1996)).⁶⁴

$$\delta = \frac{0.61\lambda}{\mu \sin \beta} \quad (1.1)$$

Where λ is the wavelength of radiation, μ is the refractive index of the sample, and β is the semi angle of the collection of the magnifying lens. The cutting-edge aberration correctors equipped in TEMs - spherical (C_s) and chromatic (C_c) - together with high accelerating voltages (200-400 kV) have contributed towards increasing the resolution below 1 Å.²⁵

The scanning transmission electron microscope (STEM) is an invaluable and highly versatile instrument used in atomic resolution imaging and characterization of nanomaterials. It is a combination of the scanning electron microscope (SEM) and TEM. The STEM performs in the same principle as SEM, where the lenses are adjusted to produce a focused convergent electron beam, which is raster-scanned over the sample, and resulting signals are collected to form an image. The main advantage of STEM over SEM is the enhanced spatial resolution. It requires very thin (electron-transparent) samples so that transmission imaging mode can be occupied. Therefore, most STEM detectors are placed after the sample to detect transmitted electrons. One of the main advantages of STEM is the availability of multiple detectors that can operate simultaneously to collect the maximum amount of information from a sample scan. The bright-field (BF) detector uses the transmitted beam while the annular dark-field (ADF) detector excludes the transmitted beam when collecting signals for image formation. Z-contrast or high-angle annular dark-field (HAADF) images are formed by the intensity of the signals from high-angle scattered electrons where image contrast can be correlated to the atomic number (Z).

1.3.2 Z-contrast imaging

Five decades ago, STEMs equipped with ADF detectors showed the ability to identify heavy elements in low atomic mass substrates by collecting elastically scattered electrons in the low angle regions. This technique, however, suffered from issues with the interference from inelastically scattered electrons. As a solution, HAADF detectors were introduced in the STEM, where the Bragg electrons can be avoided by collecting the scattered electrons at angles above 50 mrad. The signals detected by the HAADF detectors are converted to a STEM micrograph in which the image intensity strongly depends on the atomic numbers of the elements present in the sample and, thus, the name Z-contrast imaging.^{7,26}

Z-contrast imaging provides a compositional perspective of the sample. The relationship between the intensity of the signal in a HAADF micrograph and corresponding atomic number of the element present in the sample can be expressed as $I \propto Z^x$, where I is the intensity of the HAADF signal, Z is the atomic number of the element, and x is a value in the 1.6-1.9 region.^{7,27} The HAADF technique forms an incoherent image, and thus, is free from the phase problem, unlike in phase-contrast microscopy.⁸ HAADF or Z-contrast imaging has the added advantage of obtaining EELS and EDS spectral maps along with the HAADF image, simultaneously, such that every pixel of the HAADF micrograph has a corresponding EDS or EELS spectrum. These techniques combined can provide vital information on the structure, composition, and bonding of the material.²⁶⁻³⁰

1.3.3 Aberration correction

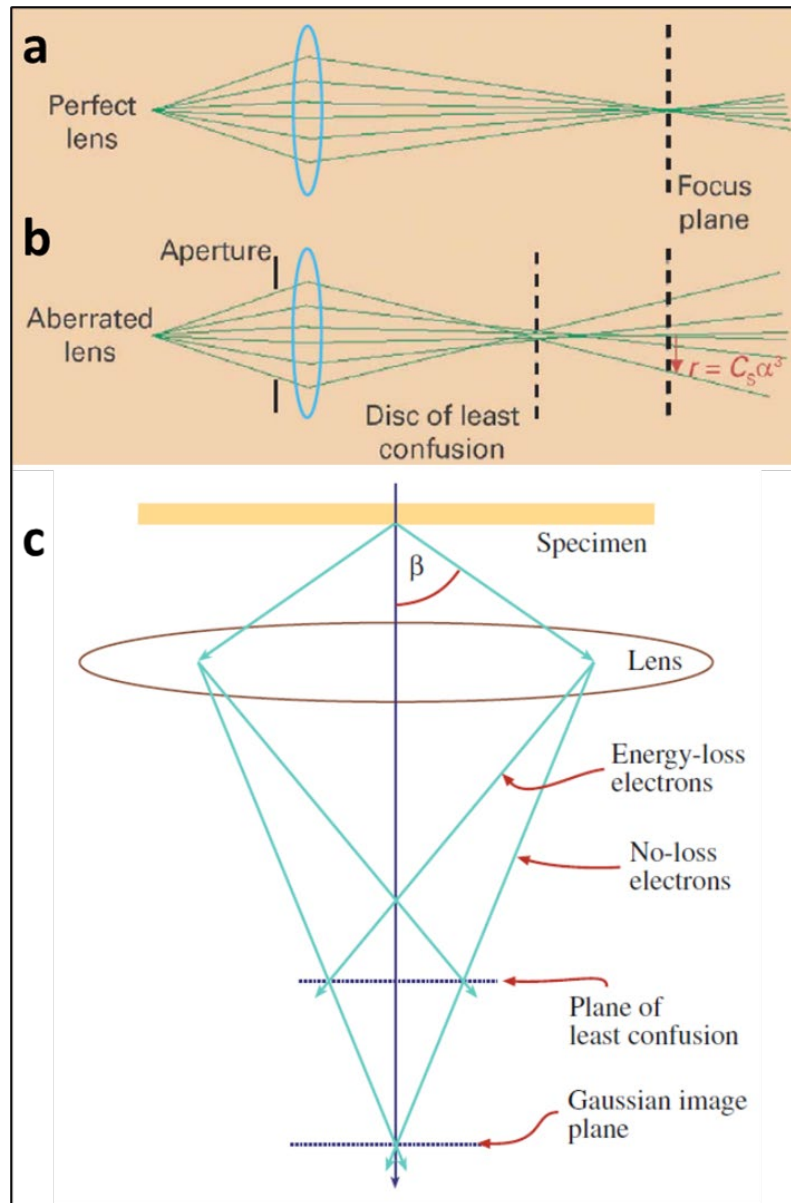


Figure 1.4 A comparison of a perfect lens (a) with lenses with spherical (b) and chromatic (c) aberrations. Copyright permission from Bleloch *et al.* (2004) and Williams and Carter (1996).^{31,32}

In the mid-1930s, Otto Scherzer demonstrated that any electron lens system would suffer from spherical and chromatic aberrations, which will limit the resolution of an electron microscope in considerable ways. A major breakthrough in the field of transmission electron microscopy was made with the introduction of aberration correctors,

which significantly improved the resolution of TEMs below 1 Å.³¹ In contrast to a perfect lens without any aberrations or imperfections (Figure 1.4a), a lens with spherical aberrations will cause off-axial rays to be focused at a different point than the paraxial rays leading to a premature focus (Figure 1.4b). As a consequence, a point specimen will be displayed as a finite-sized disk, and the ability to magnify details of the specimen would be compromised. A lens with chromatic aberration tends to deflect electrons with lower energies more than those with high energies. As a result, electrons with different energies will be focused in different planes, and therefore, a point object would be imaged with a blur (Figure 1.4c).^{32,33}

Aberration correctors are based on the principle of introducing negative aberrations to negate the positive aberrations created by the lens. In a conventional TEM, the aberration corrector is placed after the objective lens, whereas in a dedicated STEM, the multipole aberration corrector is located in between the condenser lens system and the probe-forming (“objective”) lens. This key development has enabled sub-angstrom resolution in TEMs, especially in STEM, where the newly achieved improved resolution with sub-angstrom probes, allows the ability to perform atomic-resolution imaging paired with spectroscopy and direct interpretation of Z-contrast imaging, which is of crucial significance in the field of material science.^{31,34-38}

1.3.4 Fourier filtering

Fourier transform is a mathematical algorithm that transforms a function to components of its frequencies. The Fourier filtering process eliminates noise from high-resolution TEM/STEM (HRTEM/HRSTEM) micrographs while retaining and enhancing other information such as lattice fringes and dopant atoms. In the fast Fourier transform

(FFT) process, the HRTEM/HRSTEM (HAADF) image (in the real-space) is Fourier transformed to get the bright spots in the reciprocal space such that the FFT is an effective means to calculate the form of the electron diffraction pattern. This process is equivalent to the formation of an image by the lenses of a TEM, meaning that the electron diffraction pattern is obtained by Fourier transforming the electron waves of which the image is formed.³⁹⁻⁴¹

For a particular TEM/STEM micrograph obtained, an FFT can be acquired using Gatan Digital Micrograph® software. In the FFT, rings/spots corresponding to the interlayer spacings of the region of interest (ROI) in the sample are masked, and an inverse FFT (IFFT) operation is performed to regenerate the parts of the image containing selected masked spatial frequencies.^{4,42} The size, shape, and edge sharpness of the aperture (i.e., the mask) can be chosen according to the information that might need to be retained or eliminated. These simulated masks or apertures in the program are analogous to the objective aperture in TEM.⁴⁰

1.3.5 Energy-dispersive X-ray spectroscopy

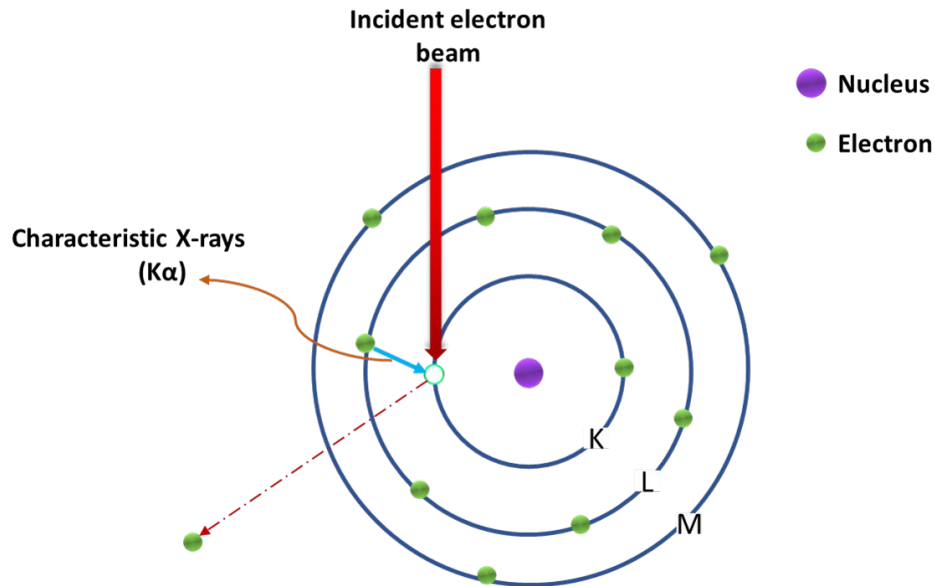


Figure 1.5 Generation of characteristic X-rays

Energy-dispersive X-ray spectroscopy (EDS) technique in TEM and SEM is used to analyze the chemical composition by analyzing the characteristic X-rays emitted by elements in the sample. When the electron beam hits the sample, electrons in the incident beam interact and eject atomic electrons in low energy levels, creating vacancies. Consequently, the electrons in high energy levels move to the low energy level to fill the generated vacancies. The movement of electrons from high to low energy levels leads to the emission of X-rays, which are characteristic of the energy level differences of each element present in the sample (Figure 1.5). The detector produces voltage pulses that correspond to these X-rays and is translated into signals using a computer system. The signal counts are then displayed as a spectrum, line scan, or an elemental spectral map allowing elemental analysis of the sample quantitatively and qualitatively. Each pixel of an EDS spectral map holds compositional information that can be extracted to an EDS spectrum, which provides the opportunity to monitor the subtle changes in the sample

composition by analyzing the EDS spectral image pixel by pixel. The quantitative elemental analysis can be performed after calibrating the detector using a proper standard.^{6,43}

1.3.6 Electron energy loss spectroscopy

Electron energy loss spectroscopy (EELS) is a technique that characterizes the energy distribution profiles of electrons after they interact with the solid specimen/sample. When a beam of electrons passes through the solid sample, it may undergo elastic and inelastic scattering processes. The elastic scattering of an electron occurs due to the Coulombic interactions with the nuclei; when the electron beam moves closer to the nuclei

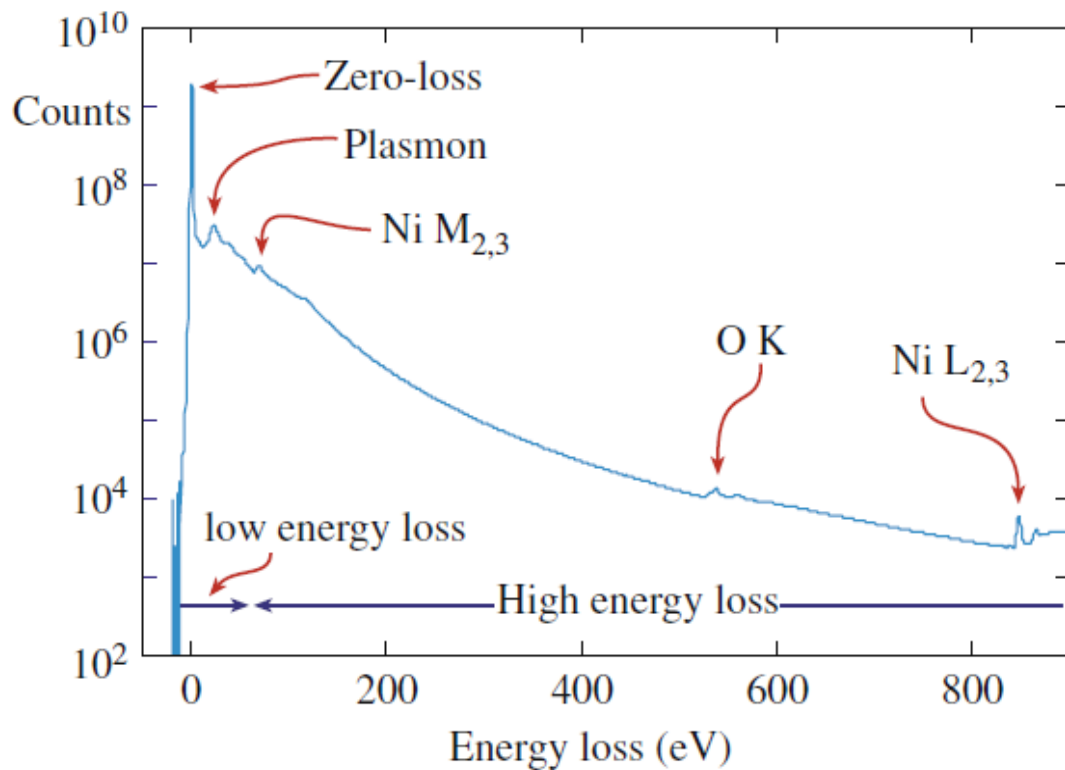


Figure 1.6 An EELS spectrum illustrating the zero-loss peak, the low-loss, and the high-loss regions. (Copyright permission @ Williams and Carter (1996))⁴⁸

of an atom, electrons lose a negligible amount of energy to the nuclei, and thus, get deflected from its course. In contrast, in the inelastic scattering process, the beam of electrons interacts with the atomic electrons and loses energy, which will be isolated to generate an energy distribution spectrum. In the sample, the path of the electron gets deflected due to Coulombic interactions, and these inelastically scattered electrons can reveal useful information about the local chemical and electronic environments of the sample, such as the valence/oxidation states, atomic structures of the surrounding atoms, and sample thickness.⁴⁴⁻⁴⁷

The EELS spectrum can be divided into two regions: a low-loss region with energies ranging up to ~ 50 eV and a high loss region with energy values higher than ~ 50 eV (Figure 1.6). The low-loss region reveals information about the band structure of the specimen. At the same time, the high-loss (also known as core-loss) region contains information on core electrons, which can be attributed to the distribution and bonding of atoms. The high-intensity peak at 0 eV represents the electrons that transmit without a significant energy loss, which corresponds to the elastically scattered electrons and, thus, called the zero-loss peak. In elemental composition analyses, EELS is often the preferred technique due to its ability to detect light elements and oxidation states, higher spatial resolution, and atomic level sensitivity, which is superior to the capabilities of EDS.^{44,45,48-50}

1.3.7 *In situ* TEM

In situ TEM uses the conventional TEM as the base instrument and combines it with a specific sample holder that has the capability of exerting external stimuli to the sample to observe and understand dynamic reactions in real-time. The use of varied external

stimuli – such as heat, mechanical strain, electrical biasing, and the introduction of liquid or gas environments with different holder systems opens up the ability to observe phase transformations, defects, deformations, and heating and cooling of nanostructures, directly.⁵¹⁻⁵³ *In situ* TEM techniques offer the opportunity to observe the dynamics of a reaction as they take place, rather than performing the reaction elsewhere (*ex situ*) and observing the starting material and end product using a TEM, and thus, not missing information on in-between mechanistic steps.⁵¹

In situ heating in the TEM, in particular, provides the ability to directly observe temporally-resolved reactions and transformations at the atomic-scale, with the use of a dedicated *in situ* heating TEM holder, which is capable of operating in the temperature region of 25-1200 °C. Breakthroughs have made in designing *in situ* heating holders to overcome a couple of critical issues such as high degree drift observed in the specimen and emission of high-intensity infrared (IR) radiation with increasing temperatures. The new semiconductor microelectromechanical systems (MEMS) based *in situ* heating systems have been able to resolve these issues to a significant extent.^{1,10,12,51,54-58}

Many advancements have seen in this field in improving the performances of *in situ* heating systems. Of particular interest, the Protochips® fusion system is capable in performing experiments up to 1200 °C with minimal thermal vibrations at high-resolution. The unique double-tilt holder permits both alpha (rotation about the axis of the sample holder) and beta (rotation about the axis normal to the sample holder) tilting during the heating experiment, which is crucial in tracking atomic rearrangements and structural phase transformations at atomic-resolution down the zone-axis. The latest Axon software platform designed by Protochips® linked with *in situ* heating systems is capable of

correcting the drift, enables auto-focus with synchronizing all *in situ* TEM datapoints automatically even at very high magnifications and allows the user to overlay metadata-such as temperature, pressure, scale - on to the TEM micrographs and videos recorded.⁵⁹

CHAPTER 2. METHODS

Parts of this chapter are taken from “M. P. Thomas, N. Wanninayake, M. De Alwis Goonatileke, D. Y. Kim and B. S. Guiton, *Nanoscale*, 2020, 12, 6144 DOI: 10.1039/D0NR00335B” Reproduced by permission of The Royal Society of Chemistry.

Parts of this chapter are taken from “N. A. Flear, M. P. Thomas, J. L. Andrews, G. R. Waetzig, O. Gonzalez, G. Liu, B. S. Guiton and S. Banerjee, *Nanoscale*, 2019, 11, 21354 DOI: 10.1039/C9NR07316G” Reproduced by permission of The Royal Society of Chemistry.

Parts of this chapter are taken from “M. P. Thomas, A. Ullah, R. H. Pham, H. Djieutedjeu, and B. S. Guiton; *Morphology controlled hydrothermal synthesis of FeS nanoplatelets*” Reproduced with permission from ACS Crystal Growth & Design, submitted for publication. Unpublished work copyright [2020] American Chemical Society.

2.1 Sample synthesis

2.1.1 Hydrothermal synthesis of FeS nanoplatelets

First, 0.3695 g $\text{Na}_2\text{S}\cdot x\text{H}_2\text{O}$ was stirred in Diethylenetriamine (DETA) (10 ml) at 150 °C for 15 minutes, followed by addition of 0.6324 g $\text{FeCl}_3\cdot 6\text{H}_2\text{O}$. After 15 minutes of stirring, deionized water (5 ml) was added to the above solution and stirred for another 15 minutes. The reaction mixture was transferred to a Teflon liner and sealed in a stainless-

steel autoclave (45 ml). The reaction mixture was maintained at 200 °C for 12 hours under hydrothermal treatment. After heating, it was allowed to cool to room temperature, and the resulting product was collected, washed with centrifugation with deionized water, ethanol and chloroform, respectively. The product was collected using a Büchner funnel, and annealed in a tube furnace at 200 °C for 12 hours with a 50 sccm Ar flow rate. After annealing, the product was collected and stored in a glove box under an N₂ atmosphere. The above procedure was repeated by replacing DETA with Triethylenetetramine (TETA) and Tetraethylenepentamine (TEPA).

To study the effect of starting material on morphology, the above procedure was carried out using 0.3695 g Na₂S.xH₂O powder and 0.3387 g FeCl₂.xH₂O in the presence of DETA, TEPA and TETA separately.

The six reaction starting material – surfactant combinations were: FeCl₂ DETA, FeCl₂ TEPA, FeCl₂ TETA, FeCl₃ DETA, FeCl₃ TEPA, and FeCl₃ TETA (hereafter denoted as D2, P2, T2, D3, P3, and T3, respectively).

2.1.2 S-, N-, and, NS-CNO

The following syntheses of CNOs, S-, N-, and, NS-CNO were performed by a Kim group student, Namal Wanninayake.

2.1.2.1 Synthesis of CNOs.

CNOs were prepared by thermally annealing nanodiamond powder ~5 nm (Dynamene NB50, purchased from Nanostructured & Amorphous Materials, Inc.) at 1700

°C for 1 hour under the flow of Helium using a graphitization furnace. Then, the CNOs were further annealed using the same furnace under air at 400 °C for 4 hours to remove any adventitious impurities.

2.1.2.2 Synthesis of Ox-CNO (oxidized carbon nano onions)

First, 500 mg of previously prepared CNOs were mixed with 36 ml of concentrated HNO₃ (Fisher Scientific, Assay-69.5%) and 64 ml of deionized (DI) water (18.2 MΩ) in a 100 ml three-neck flask. Then, the solution was subjected to ultrasonic agitation for 15 minutes to form a homogeneous solution. Next, a magnetic stir bar was added, and the solution was refluxed at 105 °C for 4 hours under 400 rpm. After cooling down, the solution was centrifuged and washed with DI water several times until the solution pH was neutral. Finally, the product was vacuum dried at 60 °C to obtain Ox-CNO.

2.1.2.3 Synthesis of N-CNO.

First, 200 mg of Ox-CNO and 1 g of urea (Sigma Aldrich, ACS reagent, 99.0–100.5%) were added into a 10 ml methanol solution (Sigma Aldrich, anhydrous, 99.8%). Then the solution was ultrasonically agitated for 10 minutes. Then, the methanol was allowed to evaporate slowly, and the resulting solid was crushed into a powder using a mortar and pestle. Subsequently, the solid was placed in a quartz boat and placed inside of a tubular furnace (LINDBERG/BLUE M, Mini-Mite Tube Furnace). The tube was then heated to 700 °C for 3 hours under an argon protected environment (Scott-Gross, 99.999%) with a heating ramp rate of 5 °C min⁻¹. The resulting solid was washed with DI water several times to remove any soluble byproducts. Finally, N-CNO was isolated by removing the water at 60 °C in a vacuum oven.

2.1.2.4 Synthesis of S-CNO.

First, 60 mg of Ox-CNO, 18 ml of dimethyl sulfoxide (Sigma Aldrich, 99.9%), and 2 ml of DI water were added into a Teflon lined container. Then, the Teflon container was closed and ultrasonically agitated for several minutes before placing inside a stainless-steel autoclave. After that, the autoclave reactor was heated to 180 °C for 18 hours in an oven. The resulting solid was washed with ethanol (Sigma Aldrich, Reagent Alcohol 95%) and DI water several times. The solid was then dried by removing the solvents at 60 °C under vacuum and placed in a tubular furnace. Finally, the tube was heated at 700 °C for 1 h under 5% hydrogen in argon to obtain S-CNO.

2.1.2.5 Synthesis of NS-CNO.

NS-CNOs were prepared following the same procedure used to synthesize N-CNO. In this synthesis, instead of urea, thiourea (Sigma Aldrich, $\geq 99.999\%$ (metals basis)) was used as the nitrogen and sulfur donor.

2.1.3 Synthesis of cubic HfO₂ and HfV₂O₇

The following syntheses of VO₂, HfO₂, and HfV₂O₇ were performed by a Banerjee group student, Nathan Fler.

2.1.3.1 Synthesis of VO₂ nanocrystals

VO₂ nanowires with lateral dimensions of 180 ± 70 nm and lengths of 1.6 ± 0.9 μ m have been prepared by the hydrothermal reduction of V₂O₅ with acetone as reported in previous work. Briefly, 1.60 mg V₂O₅, 42.0 mL acetone, and 33.0 mL of deionized water ($\rho = 18.2$ M Ω cm, Barnstead Water Purification System) were placed in a 125 mL polytetrafluoroethylene vessel, which in turn was placed within a sealed hydrothermal reactor and maintained at 210 °C for 72 h. The recovered solid was filtered and washed three times with water and subsequently three times with acetone. The recovered powder was then dried and annealed within a tube furnace under a flow of Ar gas (50 sccm); the furnace was heated to 550 °C at a heating rate of ca. 43 °C min⁻¹ and held at this temperature for 5 h. The annealed solid, VO₂ nanowires crystallized in the M1 phase, was then removed and used as prepared in further reactions. Quasi-spherical VO₂ nanocrystals with a diameter of 44 ± 30 nm have been prepared by an alternative sol-gel condensation and hydrothermal treatment route. Briefly, VO(OH)₂ was precipitated from the reaction between NH₄VO₃ and N₂H₄ in deionized water at a temperature of 80 °C. The solid precipitate was then heated at 210 °C for 24 h within the hydrothermal apparatus described above with the addition of 16 mL of water. The recovered powder was washed with copious amounts of water and acetone across three cycles of resuspension and centrifugation.

2.1.3.2 Deposition of HfO₂ onto VO₂ nanocrystals

Amorphous HfO₂ shells were deposited onto nanowires and quasi-spherical nanocrystals of VO₂ through a hydrolysis approach analogous to the Stöber method for the preparation of SiO₂ shells. In the first step, 30 mg of nanowires or quasi-spherical nanocrystals of VO₂ crystallized in the M1 phase were dispersed in 80 mL dry ethanol

(dried over molecular sieves with 4 Å pore size and Na₂SO₄) via ultrasonication (Branson 5510) for ca. 10 min. The colloidal dispersion was then placed within a three-neck round-bottom flask, which was attached to an Ar Schlenk line and cooled using an ice bath. Hf(O^tBu)₄ was added dropwise to the ethanol dispersion at a molar ratio of VO₂:Hf(O^tBu)₄ of 1:0.5 under an Ar ambient; the reaction mixture was then allowed to stir for 20 min. This dispersion was then removed from the ice bath, placed on a heating mantle, and heated to 80 °C while maintaining an Ar ambient. Next, 20 mL of a 1:20 (v/v) H₂O:EtOH mixture was added dropwise to initiate hydrolysis of the hafnium alkoxide. The low water content precludes homogeneous nucleation of HfO₂ nanocrystals in solution and constrains HfO₂ deposition to the surfaces of the VO₂ nanocrystals. The reaction mixture was maintained at 80 °C for 15 min and subsequently removed from heat and allowed to cool to ca. 50 °C before moving to centrifugation. The solid precipitate was then recovered by centrifugation at 8700 rpm using a Heraeus Megafuge 8. The recovered solid was resuspended in ethanol and recovered by centrifugation at 8700 rpm. Two such cycles were performed. Dry samples were annealed in a quartz tube placed within a tube furnace under 50 sccm of flowing Ar at 650 °C for 25 min. The annealed powder was then allowed to cool to room temperature before further analysis.

2.1.3.3 Stabilization of cubic HfO₂ by dissolution of the V₂O₃ core of V₂O₃@HfO₂ core-shell nanocrystals

After annealing to obtain V₂O₃@HfO₂ core-shell nanocrystals, the vanadium oxide shell was etched in acid solution to stabilize cubic HfO₂. Specifically, V₂O₃@HfO₂ core-shell nanocrystals were placed in a 5.67 M aqueous solution of HCl at a concentration of 1 mg solid per mL of solution. The prepared dispersion had a pH < 1, which results in the

dissolution of V_2O_3 and remnant VO_2 from the core.⁶⁰ The acid-treated sample was sonicated vigorously for ca. 1 h to ensure dissolution of the core. The supernatant turned light blue in color indicating the stabilization of vanadium oxide clusters.⁶¹ The solid was then recovered by centrifugation at 8700 rpm. The recovered solid was subsequently re-dispersed in ethanol and collected by centrifugation at 8700 rpm two times before being allowed to dry at room temperature.

2.1.3.4 Synthesis of HfV_2O_7

$VO_2@HfO_2$ core-shell nanocrystals were prepared as discussed above and the recovered powders were placed in a quartz tube and annealed under a static air ambient within a tube furnace ramping at a rate of $20\text{ }^\circ\text{C min}^{-1}$ to $650\text{ }^\circ\text{C}$. The furnace was maintained at $650\text{ }^\circ\text{C}$ for 25 min. The recovered solid was light orange in appearance and was analyzed upon cooling to room temperature.

2.2 TEM/STEM sample preparation

2.2.1 Sample preparation on a 300 mesh TEM Cu grid

A small amount of the as-synthesized powder sample was dispersed in high purity chloroform/isopropanol (Sigma-Aldrich) and sonicated for 30 minutes. Then, $10\text{ }\mu\text{L}$ of the diluted solution mixture was drop-cast onto a 300 mesh Cu grid with a holey-/lacey-carbon film.

2.2.2 Sample preparation on a Protochips® heating e-chip

A small amount of the as-synthesized powder sample was dispersed in high purity chloroform/isopropanol (Sigma-Aldrich) and sonicated for 30 minutes. Then, 10 μ L of the diluted solution mixture was drop-cast onto a Protochips® heating e-chip in a way that the sample does not short-circuit the e-chip.

2.2.3 Nion UltraSTEM 100 (U100)

The drop-cast grids/e-chips were annealed at 80/160 °C for 8 hours in vacuum ($\sim 10^{-5}$ Torr) prior to the STEM characterization.

2.2.4 Air sensitive $\text{La}_{3-x}\text{Te}_4\text{-Ni}$ sample pellets

2.2.4.1 Inserting the sample into the focused ion beam scanning electron microscope (FIB-SEM)

The $\text{La}_{3-x}\text{Te}_4\text{-Ni}$ ($x=0.26$) pellet (12.7 mm in diameter and about 1 mm thick) was stored in a vacuum desiccator until TEM sample preparation (sample synthesis was performed by the Bux group at NASA JPL). The surface of the pellet was polished with 600-grit sandpaper using 1-Propanol (Alfa Aesar, 99+%) as the lubricant. Then, the sample was inserted into an FEI Helios Nanolab 660 FIB-SEM for TEM sample preparation. The *in situ* carbon source was used for the sample surface protection and welding processes, and the gallium (Ga) ion beam was used for the milling and cleaning processes.

2.2.4.2 FIB lift-out process and attaching to the lift-out TEM grid

A lamella of $12 \times 8 \times 2 \mu\text{m}$ was cut-free from the bulk pellet using a micromanipulator (Figure 2.1c). Then, the lamella was welded onto a FIB lift-out TEM grid (copper (Cu)

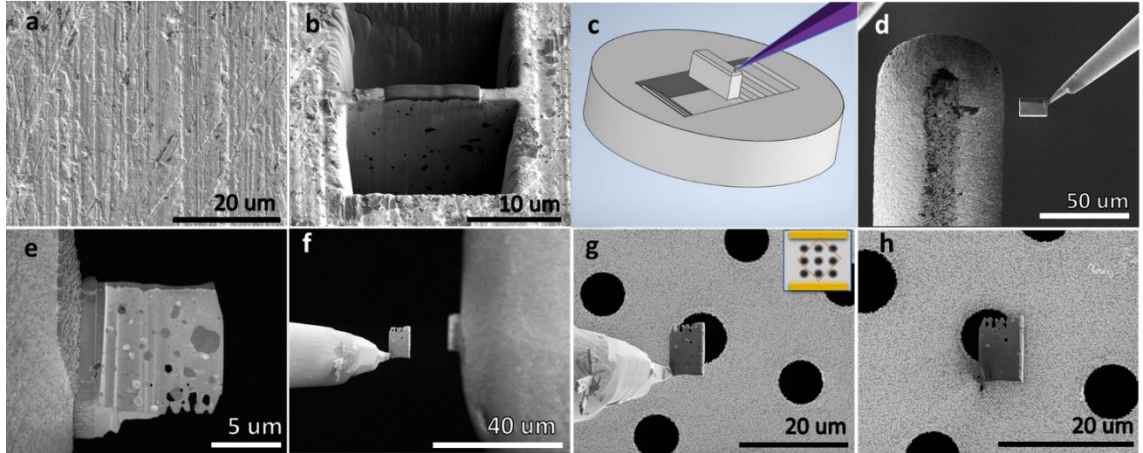


Figure 2.1 FIB sample preparation for TEM/*in situ* TEM. FIB-SEM images showing the top view of the (a) $\text{La}_{3-x}\text{Te}_4\text{-Ni}$ pellet (0.0° tilt) and (b) surface protected region after the cross-section milling (50.5° tilt). (c) Schematic illustration of the welding of the lamella to the micro-manipulator and separation from the bulk sample (pellet). FIB-SEM images taken at different stages of the attaching process; (d) before welding to the TEM copper lift-out grid for thinning, (e) lamella on TEM grid after thinning (0.0° tilt), (f) micro-manipulator attached to the lamella after cutting free from the TEM grid, (g) lamella being transferred to the TEM heating e-chip (0.0° tilt) (inset: a schematic of the nine holey-carbon sample holes of the Protochips[®] heating e-chip), and (h) the lamella after being attached to the TEM heating chip.

grid) for thinning (Figure 1d). Thinning of the sample was continued until the desired thickness (to achieve electron transparency) was obtained (less than 100 nm) (Figure 2.1e). The final milling was done at 2 keV, 24 pA to clean the surface.

2.2.4.3 Attaching the FIB lift-out lamella onto a Protochips[®] heating e-chip

The FIB lift-out procedure (FIB lift-out process and attaching to the lift-out TEM grid) was followed to obtain an electron transparent sample lamella on a FIB lift-out TEM

grid. Then, the other side of the lamella (which is still connected to the lift-out grid by one side) was attached to the micromanipulator needle and cut free from the FIB lift-out TEM grid (Figure 2.1f). Next, the lamella was transferred onto the Protochips® fusion e-chip to position the lamella on top of one of the nine holey-carbon holes of the e-chip (Figure 2.1g-h).

2.2.4.4 High-resolution TEM characterization

An Air Protection (AP) holder (Figure 2.2), which is compatible with both Hitachi NB 5000 FIB-SEM and HF 3300 TEM/STEM was used in this procedure. The FIB lift-out process was performed as described above. The unique design of the AP holder allows isolation of the sample compartment from the outside environment with an O-ring placed at the tip of the holder (just beneath the jewel bearing) (Figure 2.2). The knob located at the back of the AP holder allows the user to switch between “open” and “closed” positions. In contrast to the previous process, welding and thinning down of the lamella were performed on the FIB lift-out TEM grid, which was mounted on the AP holder before inserting into the Hitachi FIB-SEM. The holder is then removed from the FIB-SEM and inserted into the TEM in its “closed” state so that the sample will not be exposed to air. When the holder is inserted into the TEM goniometer, it is then pumped down at the pre-pumping compartment. Once the first cycle of pumping is done, the holder is switched to the “open” state and pumped down once again before fully inserting it into the TEM column. Once the AP holder is fully inserted into the TEM column, the sample holder can be “open” for HRTEM characterization in HF 3300 TEM/STEM at 300 kV (Figure 2.2).

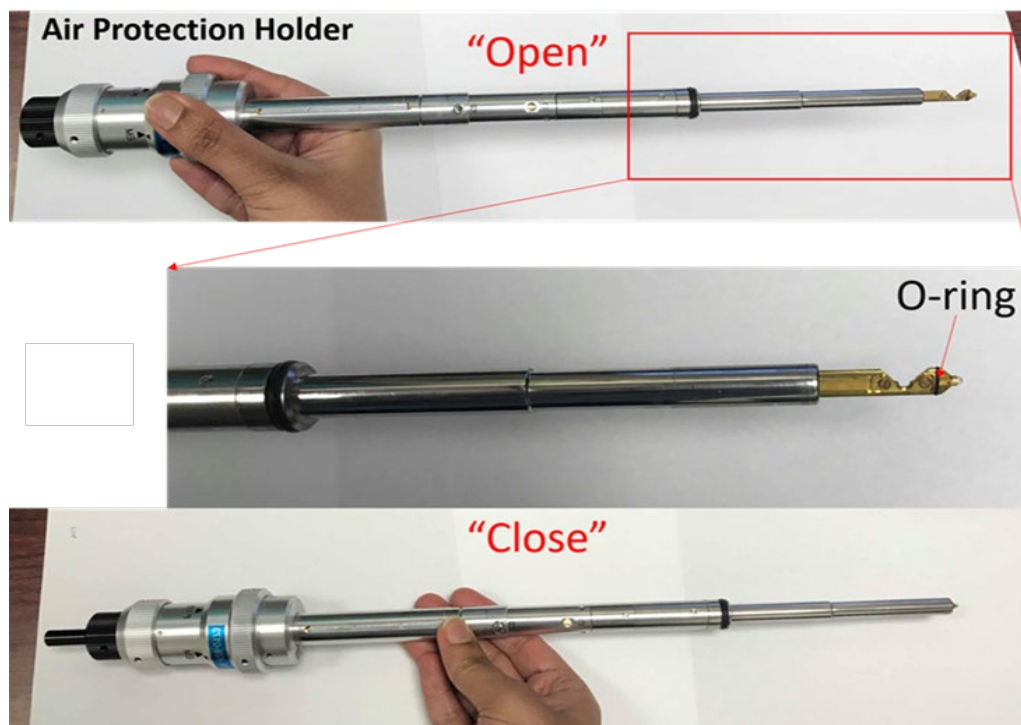


Figure 2.2 Air Protection (AP) holder compatible with both Hitachi FIB-SEM and TEM/STEM systems.

2.2.4.5 *In situ* TEM

In situ TEM experiments were performed in FEI Talos F200X TEM/STEM at 200 kV using the Protochips® Fusion heating system (The AP holder was not used in this process. The sample was transferred between the FIB-SEM and the TEM, manually, within an 80 seconds time window to avoid air-oxidation of the sample).

2.3 Characterization

2.3.1 Powder X-ray diffraction (PXRD)

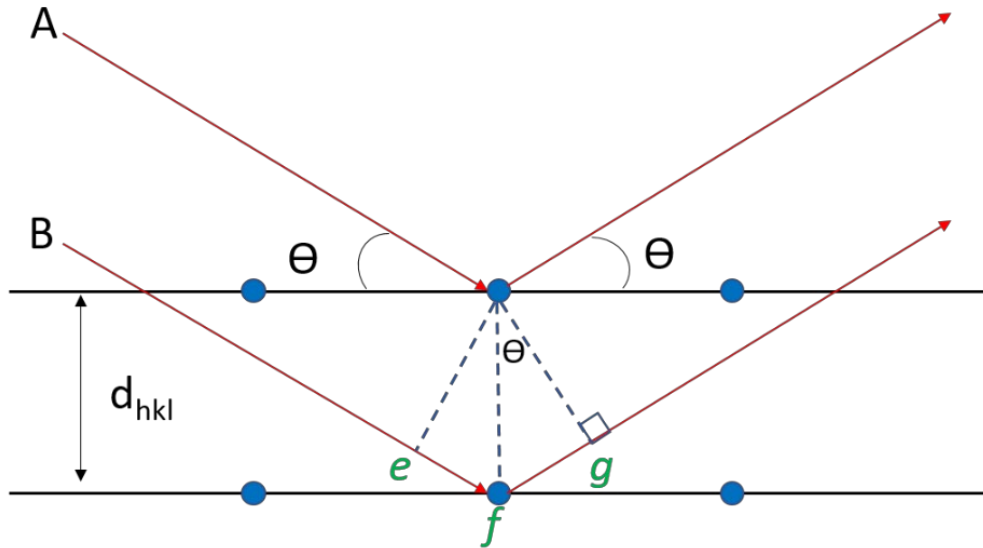


Figure 2.3 Diagram of Bragg's Law (reproduced with permission from West (2014), Wiley).⁶

X rays occur in 10^{-10} m regions of the electromagnetic spectrum. X-rays are generated when high energy electrons, which are accelerated into a high voltage, collide with a target material. When radiation is scattered by a row of atoms in a crystal, diffraction occurs. Powder X-ray diffraction (PXRD) uses this principle to investigate the crystal structure and characterize crystalline materials.⁶

Figure 2.3 illustrates a closely placed parallel planes of atoms with a crystal lattice planer distance of d_{hkl} . When the difference between the paths of X-ray beams A and B, $efg = n\lambda$ (an integer number of wavelengths), constructive interference occurs. The relationship between the wavelength of incident radiation (λ) and d_{hkl} is given by Bragg's

law ($n\lambda = 2 d_{hkl} \sin\theta$). The constructive interference only occurs when Bragg's law is satisfied.⁶

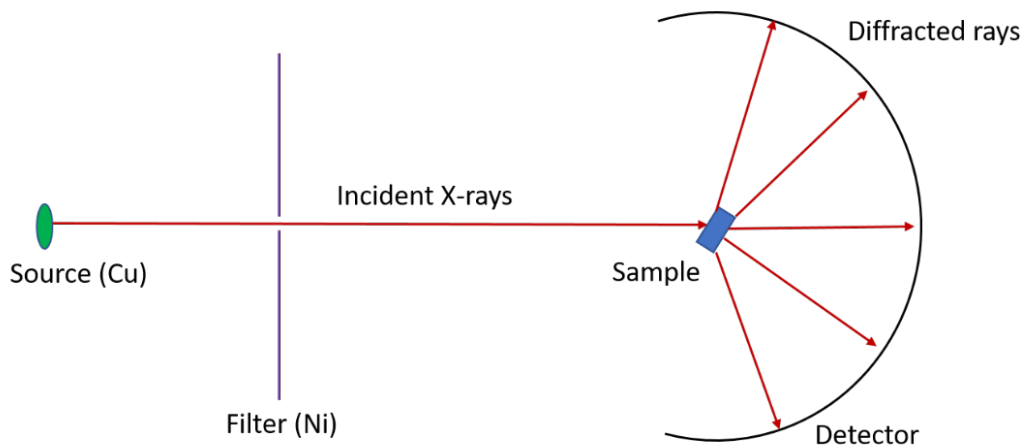


Figure 2.4 The powder X-ray diffraction method (reproduced with permission from West (2014), Wiley).⁶

In PXRD, a monochromatic X-ray beam hits the powder sample with randomly arranged crystals in all possible directions (Figure 2.4). For all sets of crystal planes, there are some crystals oriented at the Bragg's angle (θ), which leads to diffraction. A diffraction pattern plots a diffractogram, a plot of the intensity against the angle of the detector (2θ).^{6,62} The powder diffraction patterns offer information in the form of peak positions, peak intensities, and peak width. Peak positions provide information on crystal lattice planer distance (d_{hkl}), peak intensities reveal scattering factors of elements. Peak width gives information on the crystallinity of the sample and the grain size. Since the powder X-ray diffraction pattern depends on both unit cell parameters and the scattering factors of atoms, even two materials with the same crystal structure will have two different diffraction patterns. Thus, a powder X-ray diffraction pattern can be used for fingerprint identification of crystalline material.⁶

PXRD method is a non-destructive, reliable, highly sensitive user-friendly technique with effective resolution and can be considered as the primary tool for materials characterization.⁶² PXRD was performed in Bruker-AXS D8 Discover diffractometer using CuK α radiation 1.5418 Å. The diffraction patterns were indexed using standard diffraction patterns from the Inorganic Crystal Structure database or using theoretical powder diffraction patterns calculated from CrystalMaker®.

2.3.2 Scanning electron microscopy

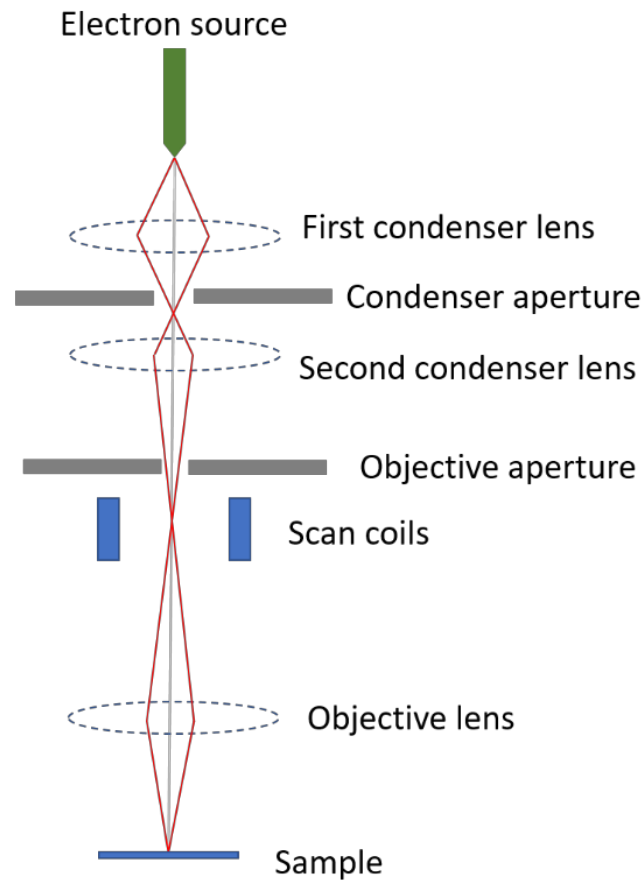


Figure 2.5 The schematic diagram of a scanning electron microscope (modified from Reichelt (2007)).⁶³

Scanning electron microscopy (SEM) uses a focused beam of high energy electrons to perform a raster scan at the sample surface, to obtain various signals to generate an image. At the sample surface, these high energy electrons interact with the solid sample to generate various signals which gives information about the topography and composition of the surface. The electron beam can penetrate about 1 μm into the sample. The penetration depth of the beam depends on the kinetic energy of electrons. In SEM, there are two types of electrons that contribute to the signal generation, secondary electrons (SE) and back

scattered electrons (BSE). While SEs are used to obtain a basic topography image, BSEs are used to get information about the elemental composition of the surface.⁶³

Figure 2.5 shows the ray diagram of SEM. At the top of the column, the electron gun accelerates electrons, which are focused on the sample stage with a set of electromagnetic lenses and apertures. SEM operates at a very low-pressure vacuum condition. The resulting SE and BSE from the interaction between the focused beam and the sample are detected by various detectors equipped in the SEM, to produce an image. Compared with conventional SEM, field emission SEM provides images with better resolution down to 10 nm. SEM was performed using Hitachi S4300 SE with an accelerating voltage between 5-20 kV.

2.3.3 Transmission electron microscopy

2.3.3.1 Transmission electron microscopy (TEM) and scanning transmission electron microscopy (STEM)

Table 2.1 Operating conditions of transmission electron microscopes used.

TEM/STEM	Operating Conditions
Nion UltraSTEM 100	<ul style="list-style-type: none">• Accelerating voltage: 100 kV• Probe current: 0.5 nA (atomic-size probe)• Equipped with 5th-order Nion aberration-corrector
FEI Talos F200X TEM/STEM	<ul style="list-style-type: none">• Accelerating voltage: 200 kV• Resolution: 0.16 nm
Hitachi 3300 TEM/STEM	<ul style="list-style-type: none">• Accelerating voltage: 300 kV
JEOL 2010F TEM/STEM	<ul style="list-style-type: none">• Accelerating voltage: 200 kV

2.3.3.2 *In situ* TEM

In situ TEM analyses were carried out using the Protochips® Fusion heating system, which is capable of heating the sample in the temperature range of 25-1200 °C. Protochips® MEMS e-chips, which have been individually calibrated, were used for sample preparation, as explained in section 2.2.2.

2.3.3.3 Selected area electron diffraction (SAED)

Selected-area electron diffraction (SAED) technique is the method to obtain a diffraction pattern of a specimen in the TEM. The selected-area (SA) aperture is several hundred nanometers in size and is placed at the image plane of the objective lens such that it creates a virtual aperture in the plane of the TEM specimen. The parallel electron beam is illuminated on the TEM specimen, and the diffraction pattern of the specimen area selected by the SA aperture is observed on the screen. The size of the SA can be chosen according to the size of sample.^{64,65}

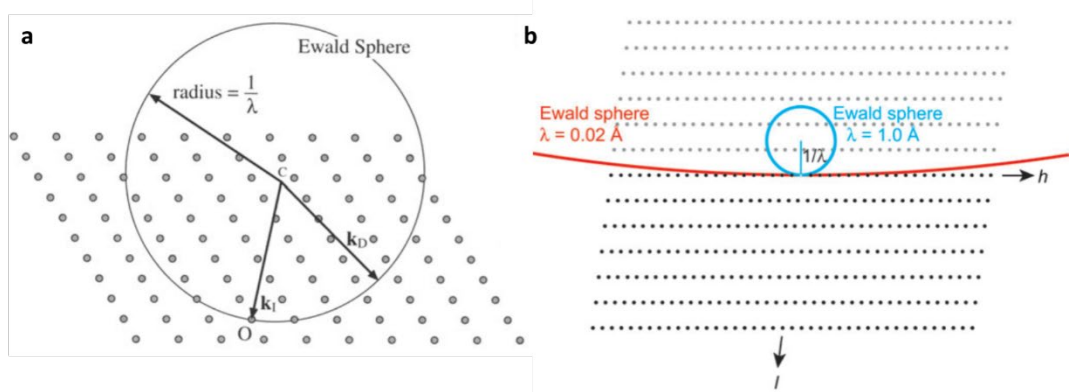


Figure 2.6 Ewald sphere construction. (a) Ewald sphere intersecting with reciprocal lattice points and (b) a comparison of the Ewald sphere construction for different wavelengths. (Copyright permission @ Williams and Carter (1996) and McCusker *et al.* (2009))^{67,68}

The intensities of the diffraction points in electron diffraction are significantly affected by multiple scattering events, and thus, differ from X-rays, where a single scattering is considered for each reflection. The multiple scattering phenomena occurs when a relatively strong diffracted beam acts as an incident beam leading to another scattering event, and this effect is profound in thicker samples.^{66–69} The diffraction spot pattern can be interpreted as the projection of the intersection of the reciprocal lattice points

and the Ewald sphere. The Ewald sphere is constructed with a radius of $\frac{1}{\lambda}$ where λ is the wavelength of the incident radiation and usually drawn over a two-dimensional array of a reciprocal lattice. When the Ewald sphere intersects with a reciprocal lattice point, the Bragg condition is satisfied (Figure 2.6a). The reason for the appearance of many diffraction spots in SAED when compared with PXRD is the difference in wavelengths of incident beams – X-ray ($\sim 1 \text{ \AA}$) and 200 kV electron beam (0.02 \AA) – which lead to Ewald spheres with varied sizes (Figure 2.6b). The Ewald sphere constructed for the electron beam has a larger radius than the Ewald sphere constructed for X-rays, and in contrast to PXRD, in SAED, the sample is thin in the direction of the incident electron beam, thus, the reciprocal lattice spots get elongated in the reciprocal direction, and thus, the Ewald sphere cuts through many reciprocal lattice points which fulfills the Bragg condition.^{66,68,70–72}

In a SAED, the large middle spot with the highest intensity corresponds to the transmitted beam without any diffraction, and the reciprocal lattice spots which get cut right through by the Ewald sphere are displayed as high-intensity spots. The superlattice reflections and appearance of systematic absences (due to multiple scatterings) may appear as weak spots in SAED.^{68,70,71}

2.3.3.4 Energy dispersive X-ray spectroscopy (EDS)

Table 2.2 The EDS systems used in the present work.

TEM/STEM	EDS detector
FEI Talos F200X TEM/STEM	<ul style="list-style-type: none">• Super-X EDS analytical system
Hitachi 3300 TEM/STEM	<ul style="list-style-type: none">• Bruker XFlash® SD detector
JEOL 2010F TEM/STEM	<ul style="list-style-type: none">• Oxford INCA EDX detector

2.3.3.5 Electron energy loss spectroscopy

EELS characterization was carried out using a Gatan Enfina EELS system in Nion UltraSTEM 100 microscope, which can achieve energy resolutions <350 meV at 100 kV. The Hartree–Slater model was used in obtaining the energy differential cross-section in EELS spectra. After the EELS spectrum was obtained, a background correction operation was performed to improve the signal to noise ratio.

2.3.4 Catalytic activity determination

The ORR activity measurements were performed Namal Wanninayake from the Kim group.

2.3.4.1 Electrode preparation.

First, 8 mg of the catalyst, 250 μ L ethanol (Sigma Aldrich, anhydrous, $\geq 99.5\%$), 750 μ L isopropyl alcohol (BDH, VWR analytical, assay 99.5%), and 60 μ L Nafion (Sigma

Aldrich, 117 solution ~5 wt%) were mixed and sonicated for 30 minutes to form a homogeneous catalyst ink solution. Then, a rotating ring disk electrode (RRDE) unit equipped with a glassy carbon disk (4 mm diameter) and Pt ring, was polished with alumina powder. After that, 8.4 μL of the prepared catalyst ink was drop casted on to the glassy carbon disk and dried at 60 $^{\circ}\text{C}$ overnight. As a comparison, commercial Pt–C catalyst (20% (w/w) Pt, Vulcan XC-72, Premetek Co) on glassy carbon was also prepared using the same method.

2.3.4.2 ORR activity measurements

The ORR activity of each catalyst was determined via RRDE measurements in a 0.1 M KOH electrolyte solution (Fluka analytical). First, the electrolyte solution was saturated with oxygen (Scott-Gross, 99.99%) by purging the gas for 30 minutes. A platinum (Pt) coil was used for the counter electrode (CE). The catalyst or Pt/C mounted disk electrode was used for the first working electrode (WE). The Pt ring electrode was connected to the second working electrode where a fixed potential was applied. An Ag/AgCl electrode (CH Instruments) filled with 1 M KCl was used as the reference electrode (RE). Linear sweep voltammograms (LSV) were recorded under the rotation rate of 1600 rpm while the disk potential was swept from 0.25 to -0.85 V vs. Ag/AgCl at the scan rate of 5 mV s^{-1} and the Pt-ring potential is fixed at 0.30 V vs. Ag/AgCl to oxidize back hydrogen peroxide. The electron transfer number (n) was then determined by the following equation.

$$n = \frac{4 I_d}{I_d + \left(\frac{I_r}{N}\right)}$$

Where I_d is the disk current,⁷³ I_r is the ring current, N is the collection efficiency of the Pt-ring. N was determined to be 0.42 from the RRDE experiment with $K_4Fe(CN)_6$.

2.3.5 X-ray Photoelectron Spectroscopy

X-ray Photoelectron Spectroscopy (XPS) is a surface analytical technique that analyses the chemical composition of a sample surface quantitatively. The sample is irradiated with a monochromated X-ray beam and the resulting photoelectrons emitted from the first 10 nm (in-depth) from the sample surface, which are characteristic of the elements that are present in the sample, are analyzed. In this study, XPS characterization was performed using Thermo Scientific K-Alpha™.

CHAPTER 3. MORPHOLOGY CONTROLLED HYDROTHERMAL SYNTHESIS OF IRON(II) SULFIDE NANOPATELETS

Parts of this chapter are taken from “M. P. Thomas, A. Ullah, R. H. Pham, H. Djieutedjeu, and B. S. Guiton; *Morphology controlled hydrothermal synthesis of FeS nanoplatelets*” Reproduced with permission from ACS Crystal Growth & Design, submitted for publication. Unpublished work copyright [2020] American Chemical Society.

3.1 Introduction

Layered tetrahedral transition metal chalcogenides (TTMC) have recently gained interest due to their unique and novel properties resulting from the partially filled transition metal *d*-orbitals. Although TTMC's are similar to transition metal dichalcogenides (TMD's) in some ways, their synthesis and structure-property relationships have been less thoroughly explored. Unlike TMD's, TTMC's favor electron-rich late transition metals which leads to metallic or superconducting properties. These TTMC's share a common metal square lattice as the structural unit where the layers of the transition metal are tetrahedrally coordinated by chalcogen atoms. These layers are held together by weak van der Waals forces which makes tuning of properties such as ferromagnetism, metallic conductivity, and, in iron containing compounds, superconductivity, comparatively easy.⁷⁴⁻⁷⁷ The stoichiometry between the metal and the chalcogen plays a key role in defining the properties of a TTMC. Even though Fe_{1.01}Se and Fe_{1.03}Se are both tetragonal at room temperature, for example, only the superconducting Fe_{1.01}Se phase undergoes a structural change to a lower symmetry orthorhombic phase at low temperatures.⁷⁸

FeS has gained significant interest among members of the iron chalcogenide family due to its large range of variable electronic, magnetic, and optical properties with interesting applications such as for solar cells and lithium ion batteries. The recent discovery of superconductivity in tetragonal FeS (mackinawite) and the structural, compositional and electronic property similarities of mackinawite to other iron chalcogenide superconductors have created much excitement.^{76,77} In previously published work, it is evident that there has been a considerable amount of disagreement on the conductivity of FeS with reported semiconducting and metallic properties.^{79,80} Many authors have recently, however, reported metallic behavior of mackinawite at room temperature.^{81–85} There are only a few reports of superconductivity, particularly when hydrothermal synthesis was employed,^{77,81,83,84,86} due both to synthetic challenges in synthesizing phase-pure stoichiometric material, and to its very low superconducting transition temperature ($T_c=3.5-5$ K) which decreases with increasing pressure, in contrast to the FeSe system.⁷⁴ Efforts have been taken to increase the T_c of FeS from 5 K to 8 K by metal hydroxide intercalation.⁸⁷ Finding a physical approach to increase T_c , however, is still a challenge. When a solid material approaches nanoscale, its physical properties may be controlled by quantum size and surface effects. The size dependence superconductivity is expected to follow in an analogous manner.⁸⁸ An investigation of shape and size dependence on T_c of mackinawite would therefore be a topic of great interest.

Iron(II) sulfide (FeS) has three stoichiometric polymorphs, tetragonal mackinawite, a cubic phase, and the hexagonal troilite.⁸⁹ The metastable mackinawite has the anti-PbO structure with each Fe atom tetrahedrally coordinated by four S atoms. These FeS₄ tetrahedra share edges to form layers which are stacked along the c-axis and held together

by van der Waals forces. The typical unit cell of tetragonal FeS has two formula units of FeS with the $P4/nmm$ space group and +2 and -2 oxidation states of Fe and S atoms, respectively.^{76,81,82,90-93} Iron sulfide is found in several less iron-rich crystallographic phases as it moves away from 1:1 stoichiometry: pyrrhotite ($Fe_{1-x}S$), smythite (Fe_9S_{11}), greigite (Fe_3S_4), marcasite (FeS_2), and pyrite (FeS_2).⁹⁴ Several studies have been reported of the phase transformation of the mackinawite phase to other stoichiometric and non-stoichiometric FeS phases at high temperature or when exposed to air over time.⁹⁴⁻⁹⁶ Shoesmith *et al.* reported a synthesis for which mackinawite is the first (kinetic) product during the synthesis before undergoing phase transformation to cubic FeS, then troilite, pyrrhotite, and finally pyrite.^{97,98} It has also been found that mackinawite transforms to a mixture of mackinawite and greigite after two months, and completely to greigite after ten months, in aqueous aging experiments.⁹⁵ Boursiquot *et al.* showed XRD evidence of mackinawite transforming to greigite, elemental sulfur, and iron (oxy-hydr)oxides upon air exposure.⁹⁶

A good understanding of design and synthesis is required to produce iron chalcogenides with varied properties suitable for each desired application. Designing and choosing a synthesis process to overcome challenges in controlling the morphology and size of these materials, therefore, is extremely important.¹⁷ Wet chemical methods such as hydrothermal and solvothermal methods have received more attention over other techniques due in part to their simplicity, controllable products, low production cost, and large-scale production potential.¹⁸ In solution-based syntheses, the use of surfactants is extremely important to obtain discrete nanostructures, by preventing particle aggregation by forming an outer layer on the particle surface. Surfactants can influence both the

nucleation and growth processes in a hydrothermal synthesis, controlling the particle shape and size by manipulating the surface adsorption of surface-active molecules on different crystal planes of the nucleating centers. The surfactant controls the growth direction and thus the particle shape.^{19,20} Crystallographic anisotropy is obtained by controlling the growth rate of different crystal faces selectively with different surfactants.⁹⁹⁻¹⁰¹

In this work we present a surfactant-assisted hydrothermal synthesis of FeS nanoplatelets for which the morphology is controlled by choice of starting material and/or the surfactant. Six reactant/starting material combinations were investigated, and samples were characterized using powder X-ray diffraction (PXRD), scanning electron microscopy (SEM), transmission electron microscopy (TEM), Energy Dispersive X-ray Spectroscopy (EDS), and Energy Photoelectron Spectroscopy (XPS).

3.2 FeS Nanoplatelets

The morphology of the as-prepared FeS samples with the six surfactant and starting material combinations was characterized using SEM (Figure 3.1), showing that the synthesis resulted in rectangular, polygonal, and shard-like nanoplatelets with platelet diagonals in the range of 1.37-34.16 μm and thicknesses between 90 and 740 nm.

The data reported in Table 3.1 were obtained by constructing distribution histograms of 50 measurements in each case, calculated by ImageJ® software (Figure 3.2). Examination of this data reveals that the Fe source had a significant impact on the resulting platelet diagonal and thickness. When $\text{FeCl}_2 \cdot x\text{H}_2\text{O}$ was employed the nanoplatelet thickness decreased by 4-8 times and platelet diagonal decreased by 14-22 times compared to that from $\text{FeCl}_3 \cdot 6\text{H}_2\text{O}$. This may be due to the higher solubility of ferrous (Fe^{2+}) ions with respect to that of ferric (Fe^{3+}) ions in the basic reaction medium employed.¹⁰² Higher solubility of ferrous ions leads to an increase in supersaturation. According to traditional

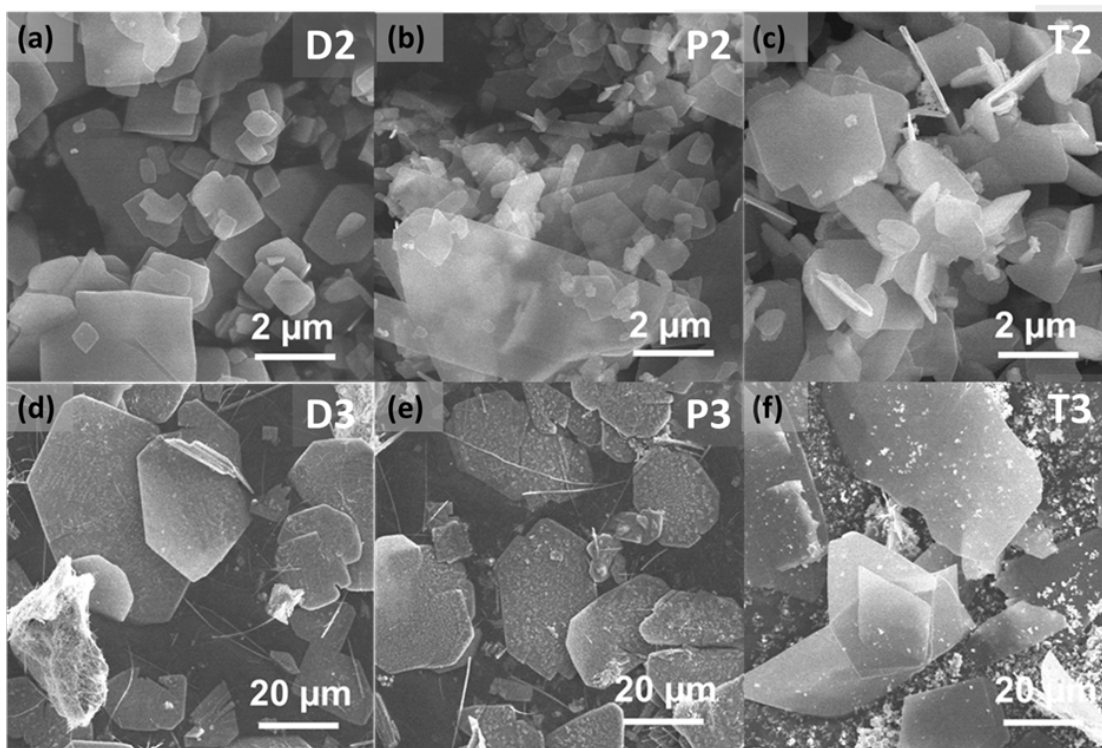
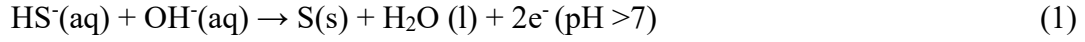


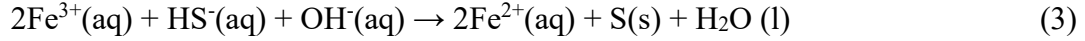
Figure 3.1 SEM images of FeS nanoplatelets with the following synthetic conditions (starting material, surfactant) a) FeCl_2 , DETA b) FeCl_2 , TEPA c) FeCl_2 , TETA d) FeCl_3 , DETA e) FeCl_3 , TEPA f) FeCl_3 , TETA.

nucleation theory, the particle size tends to decrease with increase supersaturation¹⁰³, explaining the observed decrease in platelet diagonal and thickness when $\text{FeCl}_2 \cdot x\text{H}_2\text{O}$ was

utilized. The proposed Fe^{3+} to Fe^{2+} reduction reaction equations are listed in equations 1-3.



Balanced equation:



The time needed to create one nucleus with critical size decreases with high supersaturation levels, thus achieving fast rates of nucleation and growth. When a single chemical species is crystallizing in a solution, the driving force for crystallization is expressed as a change in chemical potential ($\Delta\mu$) rather than in terms of the change in total free energy during

Table 3.1 Summary of starting material and surfactant effect on platelet diagonal, thickness, and shape of FeS nanoplatelets.

		DETA	TEPA	TETA
FeCl₂	Platelet diagonal (μm)	1.373 (0.692)	1.587 (0.748)	2.190 (1.058)
	Thickness (μm)	0.091 (0.049)	0.142 (0.050)	0.106 (0.032)
	Shape	Rectangular	Rectangular	Rectangular
FeCl₃	Platelet diagonal (μm)	28.678 (7.499)	34.160 (7.063)	29.533 (8.968)
	Thickness (μm)	0.739 (0.296)	0.600 (0.290)	0.536 (0.167)
	Shape	Hexagonal/polygonal	Hexagonal/polygonal	Shards

crystallization¹⁰³, and is given by equation (4), where μ_s and μ_c are the chemical potential of the crystallizing species in the solution and bulk crystal. Crystal growth studies typically model nucleation with respect to supersaturation (σ) which is related to $\Delta\mu$ via equation 5.

$$\Delta\mu = \mu_s - \mu_c \quad (4)$$

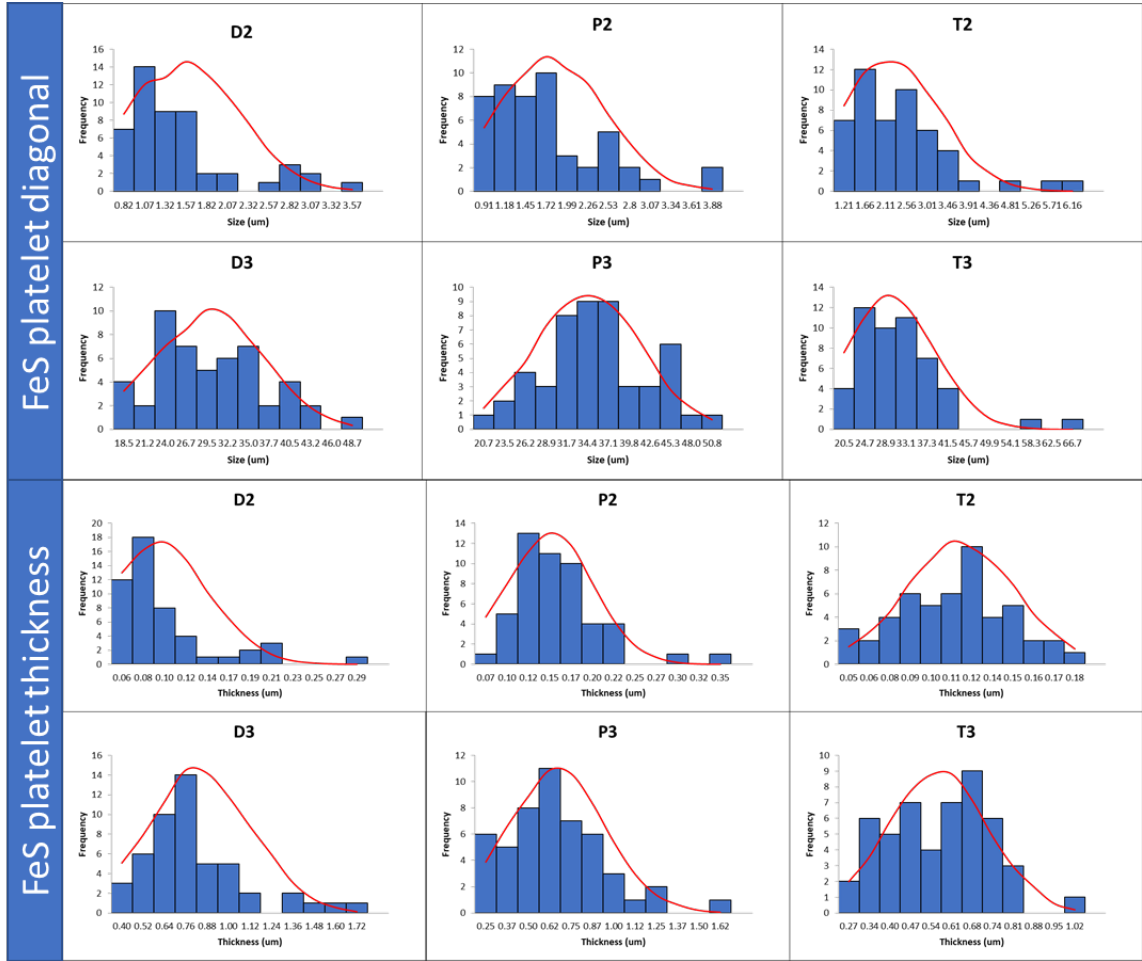


Figure 3.2 The platelet diagonal and thickness distribution histograms of the FeS platelets calculated by ImageJ® software.

$$\Delta\mu = k_B T \ln \sigma \quad (5),$$

Here, k_B is the Boltzmann constant, T is the absolute temperature, and σ is the supersaturation. Low supersaturation levels lead to slow rates of nucleation, hence increased critical cluster size. Smaller crystals with higher solubilities may dissolve and the larger crystals may grow at the expense of smaller clusters. This competitive growth is essentially the Ostwald ripening process of crystal growth.^{103–105}

With regards the effect of surfactant, it should be noted that commercially purchased DETA is a single-component linear chain primary amine, while commercial TETA and TEPA consist of four components: linear, branched and cyclic amines. The conformations formed by different surfactants around a particle nucleus can vary widely. Unbranched linear surfactants form an array of close-packed molecules on the sample surface with a fixed angle to one another, bonded by the functional group. Branched surfactants encapsulate the nucleus with empty spaces between the branches.¹⁰⁶ Steric effects, therefore, may be responsible for the observed differences in morphology when various branched amines are utilized. The combination of DETA+FeCl₃ and TEPA+FeCl₃

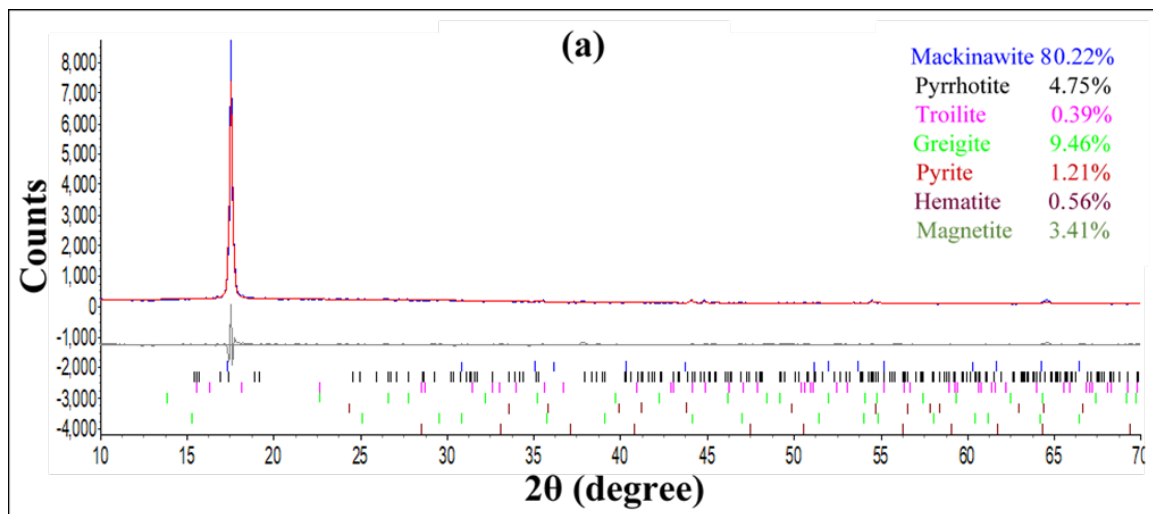


Figure 3.3 Rietveld refined PXRD pattern of the as-synthesized FeS sample from FeCl₂ and DETA. The observed, calculated and difference profiles are shown by the blue, red and gray line, respectively. The vertical bars (|) indicate the position of Bragg reflections of the calculated patterns of different iron sulfide and oxide phases.

produces hexagonal/polygonal platelet shapes, whereas a combination of FeCl₂ with DETA, TEPA, and TETA produces a rectangular platelet shape. The FeCl₃+TETA combination produces shard-like platelets. The control of morphology and platelet diagonal in these FeS platelets have been obtained by manipulating the surface adsorption

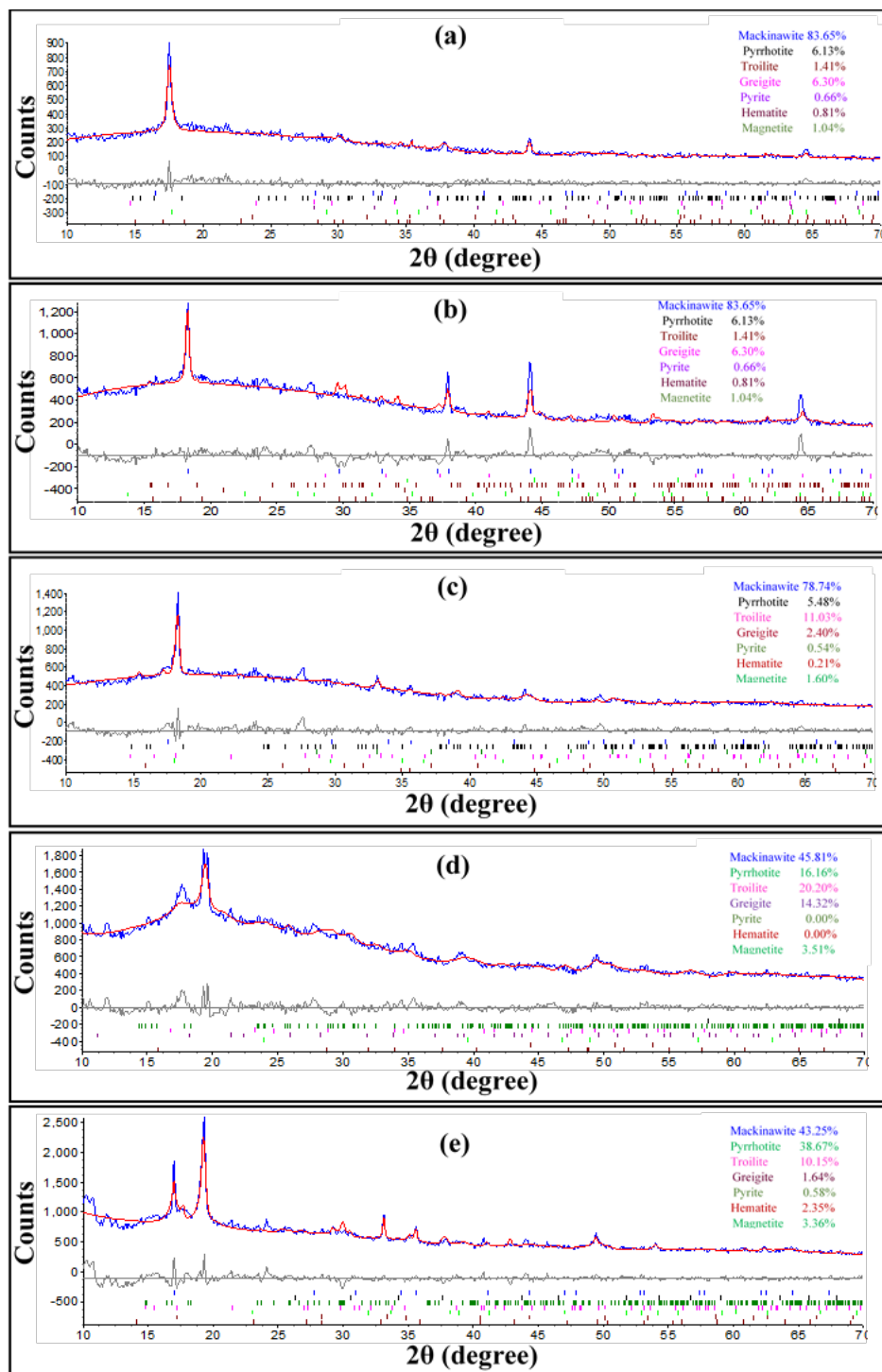


Figure 3.4 FeCl₃ DETA, (b) FeCl₂ TEPA, (c) FeCl₃ TEPA, (d) FeCl₂ TETA and (e) FeCl₃ TETA. The solid blue, red and gray lines represent the observed, calculated and difference profiles, respectively. The vertical bars (|) indicate the position of Bragg reflections of the calculated patterns of different iron sulfide and oxide phases.

of surface-active molecules (i.e. surfactants), on different crystal planes of nucleating

centers. When different surfactants were employed in the synthesis, they control the growth directions of the different crystal planes selectively at different rates, hence resulting a morphology-controlled synthesis.

Table 3.2 Rietveld analysis of powder x-ray diffraction pattern of iron sulfide samples synthesized using different ligand and iron sources.

Ligand	Iron (Fe) source	Mackinawite, (FeS) (%)	Pyrrhotite, Fe ₇ S ₈ (%)	Troilite, FeS (%)	Greigite, Fe ₃ S ₄ (%)	Pyrite, FeS ₂ (%)	Hematite, Fe ₂ O ₃ (%)	Magnetite, Fe ₃ O ₄ (%)	R _{wp} (%)
DETA	FeCl ₂	80.22	4.75	0.39	9.46	1.21	0.56	3.41	10.98
	FeCl ₃	83.65	6.13	1.41	6.30	0.66	0.81	1.04	9.22
TEPA	FeCl ₂	72.15	18.96	5.85	0.00	3.04	0.00	0.00	9.57
	FeCl ₃	78.74	5.48	11.03	2.40	0.54	0.21	1.60	7.56
TETA	FeCl ₂	45.81	16.16	20.20	14.32	0.00	0.00	3.51	5.86
	FeCl ₃	43.25	38.67	10.15	1.64	0.58	2.35	3.36	8.10

The shiny black powder products obtained from the hydrothermal synthesis were characterized using PXRD to determine the crystallinity of as-synthesized samples (Figures 3.3-3.4). According to PXRD analysis, the occurrence of FeS mackinawite phase increases as follows: T3<T2<D3<P3<D2<P2 (Figure 3.4, Table 3.2). Rietveld refinement analysis of PXRD data indicates that in all six FeS samples, most of the peaks can be indexed to a tetragonal phase of FeS (81087-ICSD) (refined unit cell parameters available in Table S2). The very intense 001 peak (~ 17°) seen in PXRD suggests these nanoplatelets have preferred growth direction with plate normal along the [001] direction. In the DETA and TEPA samples (D2, D3, P2, and P3), a few minor phases can be identified (Table 3.2,

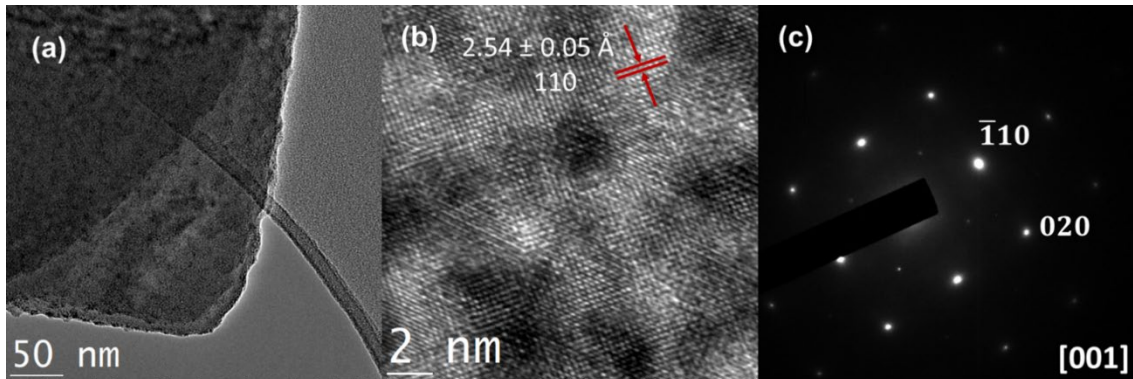


Figure 3.5 TEM characterization of FeS nanoplatelets; (a) low resolution TEM image of a representative nanoplatelet, (b) HRTEM from the same platelet showing lattice fringes identified as the (110) planes of tetragonal FeS, and (c) representative SAED pattern.

Figure 3.4), mainly the greigite, troilite, and pyrrhotite phases, with some oxidation additionally due to the hematite (Fe_2O_3) and magnetite (Fe_3O_4) phases. The TETA (T2 and T3) samples show much higher fraction of these non-mackinawite phases than the DETA

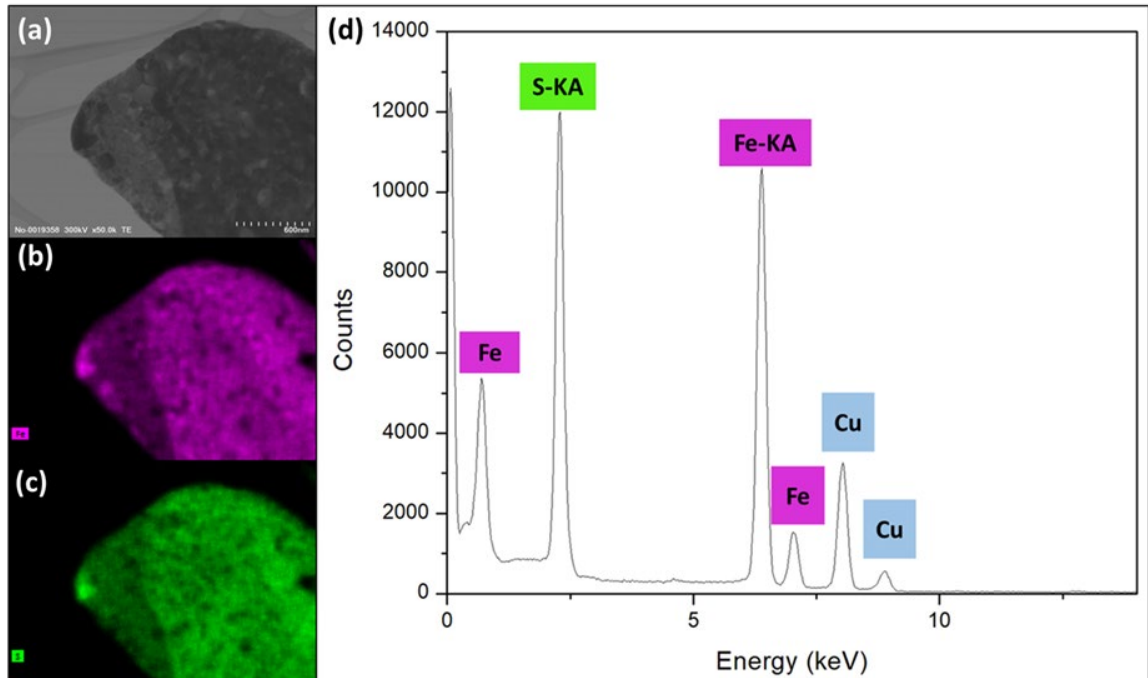


Figure 3.6 EDS analysis of an FeS nanoplatelet (sample D2); (a) STEM image; EDS elemental maps of (b) Fe, (c) S, and (d) EDS spectrum confirming the presence of elements, Fe and S in the sample.

and TEPA samples. The two-peak condition (15-20°) seen in the TETA samples and peaks appearing around 38-40° can be recognized as an indication of multiple phases, pyrrhotite, troilite, and greigite.¹⁰⁷

TEM and HRTEM images (Figure 3.5) reveal the atomic- and micro-structure of the platelets in the as-prepared D2 sample. The low resolution TEM image of the sample shows the rectangular morphology of a nanoplatelet and the high resolution TEM (HRTEM) shows the highly crystalline nature of the nanoplatelet. The lattice fringes appearing in the HRTEM image (Figure 3.5b) were measured to be $2.54 \pm 0.05 \text{ \AA}$ which matches with (110) planes of tetragonal FeS mackinawite. SAED patterns obtained from platelets in the same

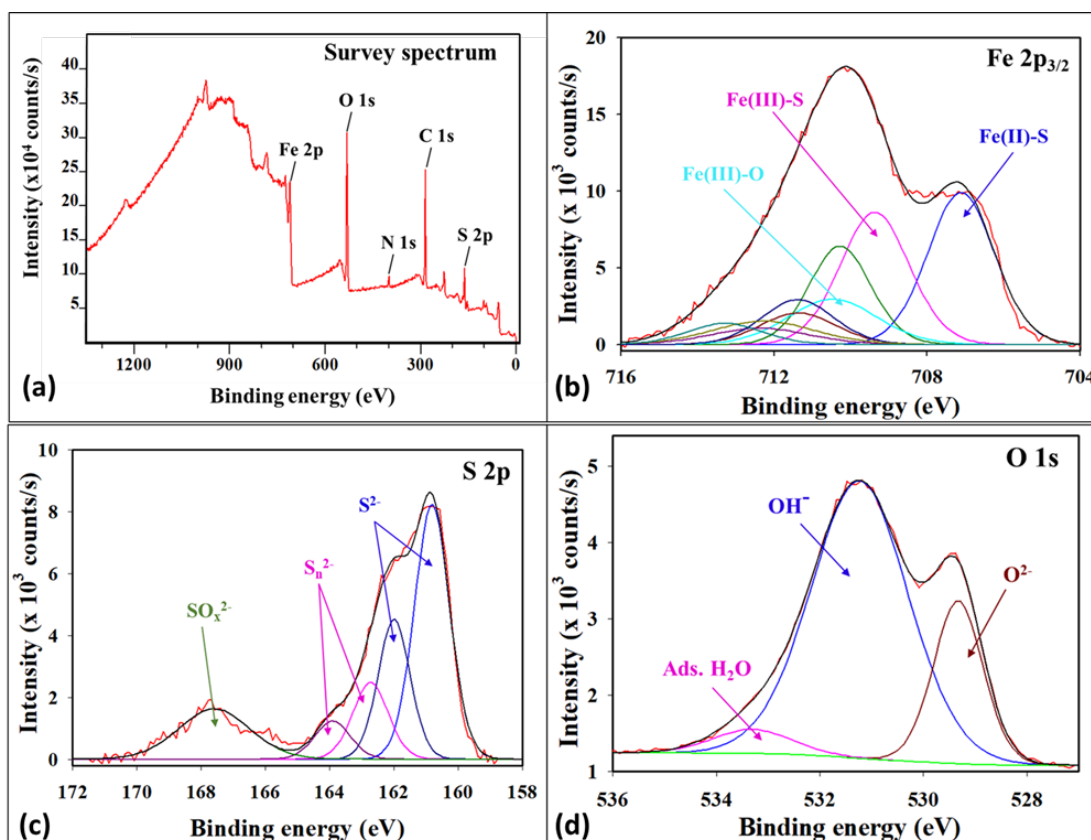


Figure 3.7 XPS spectra of FeS synthesized from FeCl₂ using DETA surfactant (D2): (a) survey spectrum; (b) Fe (2p_{3/2}) region; (c) S 2p region and (d) O 1s region.

sample (example in Figure 3.5c) further confirms that these nanoplatelets are single-

crystalline and have a unique growth direction such that the platelet normal is parallel to the FeS [001].

EDS experiments were performed to analyze the elemental composition and distribution within the FeS nanoplatelets. The spectrum for the D2 sample (Fig. 3.6(d)) shows peaks corresponding to Fe, S, and Cu including sharp S-K α (~2.3 keV) and Fe-K α (~6.4 keV) peaks, thereby confirming the presence of Fe and S. The peaks corresponding to Cu come from the Cu TEM grids used in preparation of the TEM samples. EDS elemental maps (Fig. 3.6(b) and (c)) clearly shows homogenous distribution of Fe (purple) and S (green) throughout the nanoplatelet.

XPS analysis of the D2 sample is shown in Figure 3.7. The survey spectrum shows Fe 2p, S 2p, O 1s, C 1s and N 1s peaks (Figure 3.7a). Unreacted surfactant in the sample could be the source of the nitrogen peak, and oxygen and carbon peaks could be the result of surface oxidation, universal contamination, or carbon tape. Figure 3.7b displays the XPS spectrum of the Fe (2p_{3/2}). By examination of the literature, the Fe(2p_{3/2}) spectrum was best fitted by three main components: Fe(II)-S, Fe(III)-S and Fe(III)-O at binding energies 707.1, 709.4, and 710.5 eV, respectively.¹⁰⁸⁻¹¹¹ Fe(II)-S is a low spin compound and contains three paired electrons at t₂ level, therefore a single peak was used to fit the low energy region of Fe(2p_{3/2}) spectrum. In the case of low spin Fe(III)-S, a main peak at 709.4 eV with additional three multiplets (each of them separated by 1eV) were used for fitting, because both contain a unpaired electron at the t₂ level which induces a multiplet. Similarly, a major peak of Fe(III)-O species at 710.5 eV with three multiplets, each separated by 1 eV, were used to obtain the best fit for high energy region of Fe(2p_{3/2}) spectrum.

The XPS spectrum of S(2p) is shown in Figure 3.7c. In the literature, S(2p) spectra were fitted with the doublets of different iron sulfides. Doublets in the S(2p) spectrum arise due to the spin-orbit splitting. Each doublet consists of two peaks S(2p_{3/2}) and S(2p_{1/2}) which are separated by 1.18 eV and the intensity ratio of S(2p_{3/2}):S(2p_{1/2}) is 2:1. To get a good fit in this study, the S(2p) spectrum was fitted with two doublets of mono-sulfide(S²⁻) and polysulfide(S_n²⁻), respectively. S(2p_{3/2}) peaks at 160.8 eV and 162.7 eV are typically attributed to mono-sulfide(S²⁻) and polysulfide(S_n²⁻), respectively.¹¹¹ A SO_x²⁻ peak was also observed at 167.6 eV in the spectrum which reveals that some oxidation of the surface may have occurred while handling or annealing.¹¹²

The O (1s) spectrum with broad peaks can be best fitted with three components at 529.3, 531.2 and 533.3 eV. These broad peaks correspond to oxide, hydroxide and adsorbed H₂O, respectively.¹¹³⁻¹¹⁵ All the peak fittings of Fe(2p), S(2p) and O(1s) spectra show a very good agreement with the literature.

3.3 Conclusion

In conclusion, morphology control of FeS platelets was achieved with a simple one step hydrothermal synthesis. The platelet diagonal, thickness, and shape of nanoplatelets are strongly dependent on the Fe-source and the surfactant employed in the synthesis process. The occurrence of the mackinawite phase in as-synthesized FeS products increases as follows: TETA < TEPA, DETA. This work makes a key step towards tuning the physical characteristics of FeS by size control.

CHAPTER 4. DIRECT IMAGING OF HETEROATOM DOPANTS IN CATALYTIC CARBON NANO-ONIONS

Parts of this chapter are taken from “M. P. Thomas, N. Wanninayake, M. De Alwis Goonatilleke, D. Y. Kim and B. S. Gupton, *Nanoscale*, 2020, **12**, 6144
DOI: 10.1039/D0NR00335B” Reproduced by permission of The Royal Society of Chemistry.⁴²

4.1 Introduction

Carbon-based nanomaterials where heteroatoms or metal–ligand complexes are embedded have been investigated as an effective alternative to replace precious Pt-based catalysts, mainly due to their cost effectiveness, long-term stability and comparable catalytic activity.^{116–122} Carbon nano-onions (CNOs) are multi-shelled carbon nanostructures with a hollow core and concentric polyhedral shells, which can be synthesized by thermal annealing of nano-diamonds, chemical vapor deposition, arc-discharge, etc.^{123–126} CNOs exhibit high electrical conductivity and chemical activity due to high surface curvature and strain energy. Due to a high specific-surface-area and catalytic surface, CNOs are useful for chemical and electrochemical conversions.¹²⁷ With the presence of many active sites due to the large surface area and significant number of defects, CNOs have shown high efficiencies to catalyze reactions such as C–H bond activation, oxygen reduction reaction (ORR), ring opening polymerization, alcohol oxidation, and styrene epoxidation.^{117,123,128–130}

Doping CNOs with non-metallic heteroatoms is known to be an effective method to change their physical and chemical properties.¹¹⁷ Compared to undoped CNOs, N- and B-doped CNOs have shown enhanced catalytic activity in styrene epoxidation reactions and

the ORR.^{117,123} Lin *et al.* reported that N heteroatom dopants produce a large number of structural defects in the graphitic shells of the CNO, which can explain its enhanced catalytic activity in styrene epoxidation reactions.¹²³ Moreover, it has been shown that CNOs with a higher number of defect sites are more susceptible to reactions occurring at the surface.¹³¹ The configurations and locations of the dopant atoms and defects, therefore, are likely key factors determining the catalytic activity of heteroatom doped CNOs.¹³² Recent studies of doped catalytic CNOs have shown the structure of concentric graphitic layers of the CNO via TEM/STEM.^{117,123,124,126,133} Previous computation studies have identified specific chemical configurations involving single dopant or multiple dopants in close proximity to one another as candidates for efficient catalysis.¹²⁹ Nonetheless, experimental evidence that confirms such sites have been rarely reported. A detailed structural analysis is imperative, therefore, to locate heteroatom dopants and associated defects. As an example, to further understand the effect of co-heteroatom-doped carbon host structures towards catalytic mechanisms such as the ORR or electrochemical carbon dioxide reduction,¹³⁴ atomic-scale visualization of the catalyst is crucial. The structural details provided by such analysis can be used directly for building computational models for which density functional theory (DFT) calculations are utilized to deduce viable reaction pathways for these mechanisms.¹³⁵

Motivated by the aforementioned necessities, here we report the direct imaging of heteroatoms in doped CNOs for the first time, via aberration-corrected STEM equipped with EELS, and provide an analysis of dopant configuration and location with respect to discontinuity/defect sites in the CNO graphitic shells, for three CNO samples: sulfur-doped CNOs (S-CNO), nitrogen-doped CNOs (N-CNO), and nitrogen and sulfur co-doped CNOs

(NS-CNO). Finally, the ORR catalytic activities of these samples were compared to gain insight into the role of heteroatom dopants on CNOs and the enhanced catalytic activity of NS-CNO with respect to N- and S-CNO.

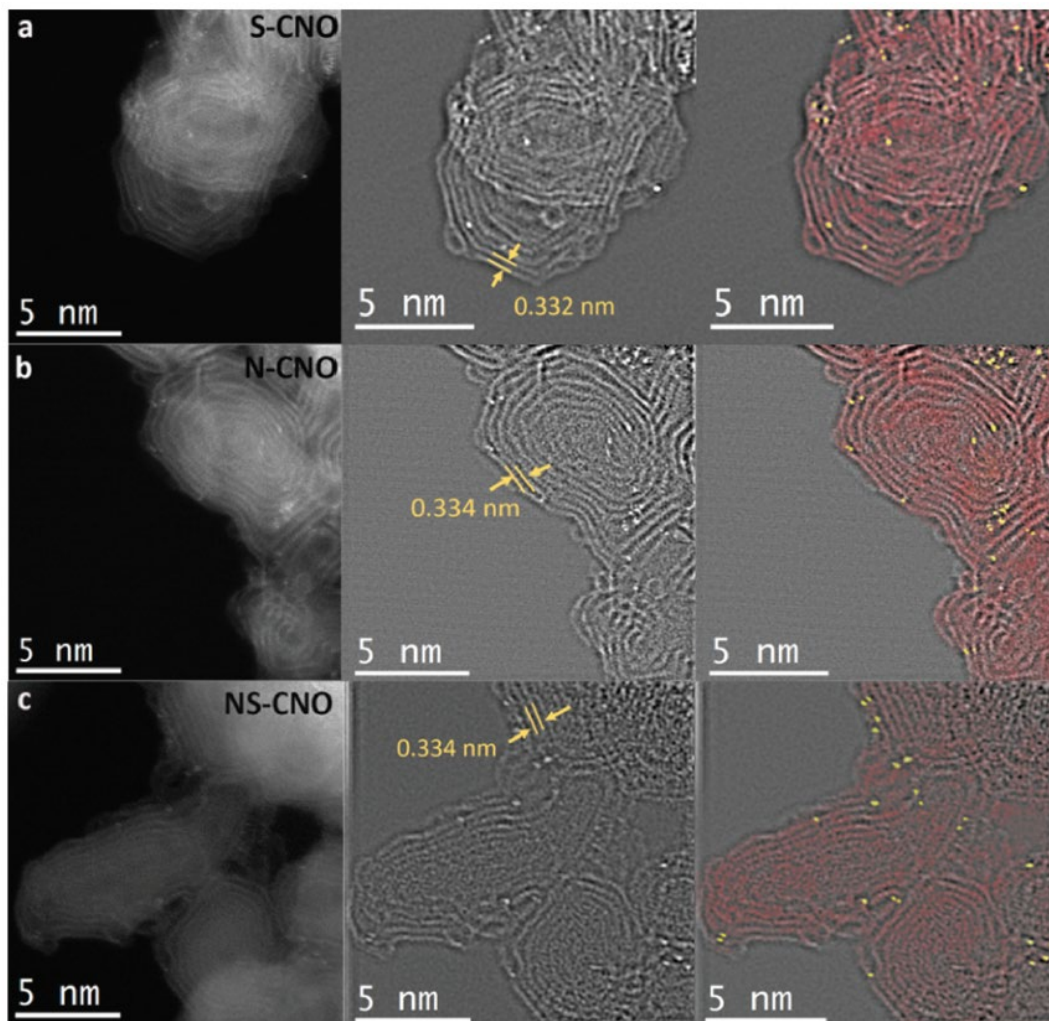


Figure 4.1 HRSTEM images of CNO with heteroatom dopants, (a) sulfur-doped, (b) nitrogen-doped, and (c) sulfur and nitrogen co-doped, and their respective IFFT filtered (middle) and false-colored (right column) images. Red = carbon; yellow = dopant atom.

4.2 S-, N-, and, NS-CNO

Figure 4.1 shows high resolution STEM (HRSTEM) micrographs (first column) and their respective filtered images (second column) of N-, S-, and, NS-CNO samples. In the third column, the heteroatom dopants (green) and graphitic shells of CNO (red) are false colored to enable recognition of dopant atoms. Images reveal that the onion like concentric shell structure of the CNO has been retained during the doping step. The interlayer spacing of the graphitic shells of N-, S-, and NS-CNO are ~ 0.33 nm, consistent with the 0.33–0.35 nm range in previous reports.^{136,137} The heteroatom dopants (N and S) and their configuration (whether they are arranged in groups or as single atoms (Figure 4.2) can be seen clearly in the HRSTEM images. High-angle annular dark field (HAADF), also known as Z-contrast imaging mode, is a STEM imaging mode using an annular detector to collect electrons scattered through high angles (usually >80 mrad).¹³⁸ The scattering intensity of electrons on this detector is roughly proportional to $Z^{1.6-1.9}$,⁷ and this mode therefore produces an image in which higher mass atoms and materials correspond to regions of higher intensity, and images which are easily interpretable. The contrast observed in Figure 4.1 (first column) therefore represents concentric spherical shells, with individual and grouped dopant atoms of higher atomic number than the shell. Individual atoms identified through their high intensity in the HAADF image have been false colored (column 3) for clarity.

EEL spectroscopy (Figure 4.3) performed on all three samples confirms the presence of carbon, nitrogen, and sulfur as expected. An oxygen signal was also recorded, and can be attributed to oxygenated functional groups formed during chemical oxidation of CNOs prior to the doping process. The oxygen signal was found in all three samples.

The EELS edges of N and S can be identified clearly, and are shown in the magnified regions of the spectra inset in Figure 4.3 Defects such as discontinuities and holes in the graphitic shells of the CNO (Figure 4.4) are identified with red arrows in filtered micrographs of the three doped samples (Figure 4.5).

The defects form edges in concentric graphene shells and play an important role in catalysis. STEM imaging indicates that the proximity of the dopant to the defect is important and we might gain insight from a quantitative analysis of the configuration of the heteroatom dopants (whether they are present as isolated atoms, or as groups), and their proximity to defects within the graphitic shells. Data taken from the three samples is summarized in Table 4.1 (detailed information is available in Tables 4.2-4.4). This

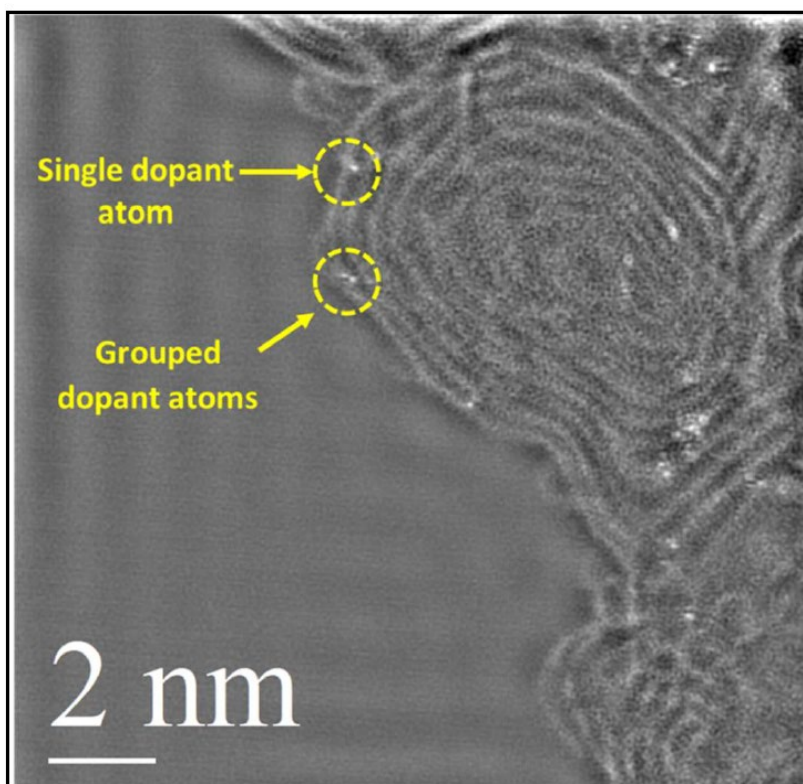


Figure 4.2 Fourier filtered HAADF image indicating single and grouped dopant atoms (yellow circles) in a N-CNO represents measurement of 98 CNOs, 358 dopant atoms/groups, and 358 defects in total. It

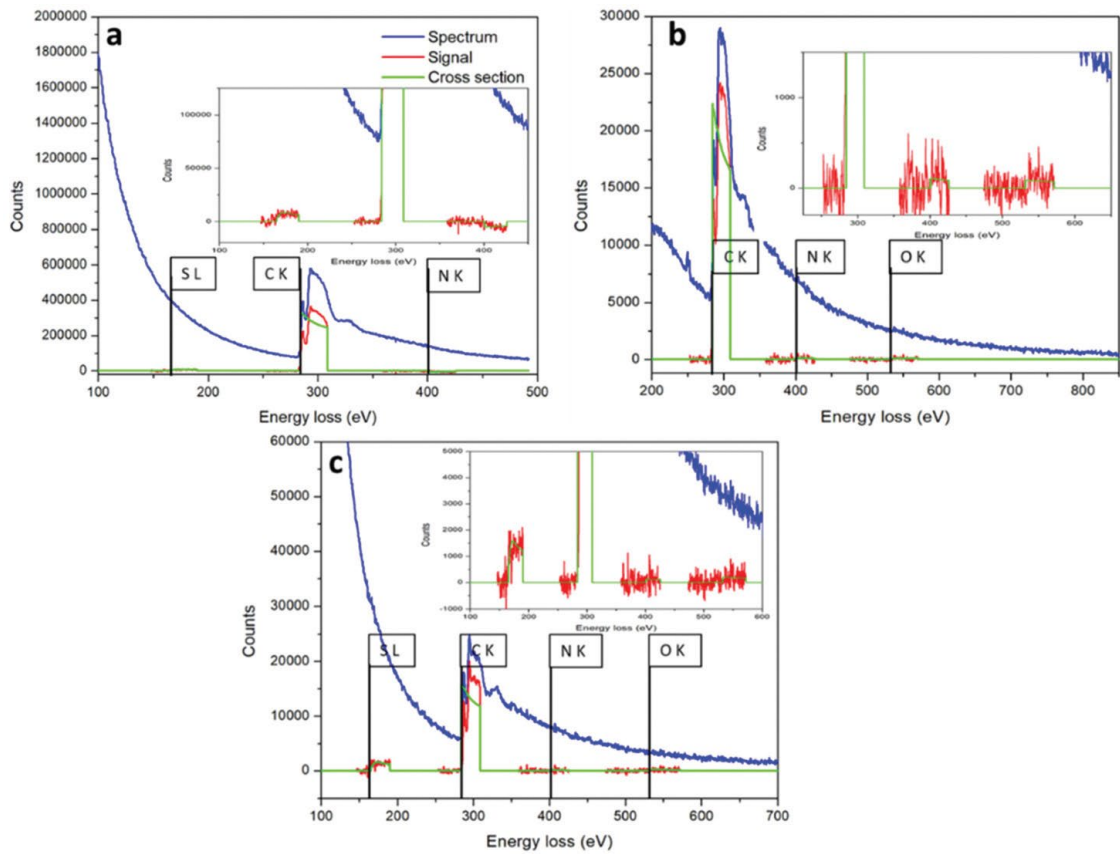


Figure 4.4 EEL spectroscopy. (a) Sulfur-doped, (b) nitrogen-doped, and (c) sulfur and nitrogen co-doped, CNO samples, confirming successful doping of the respective heteroatoms into the CNO structure.

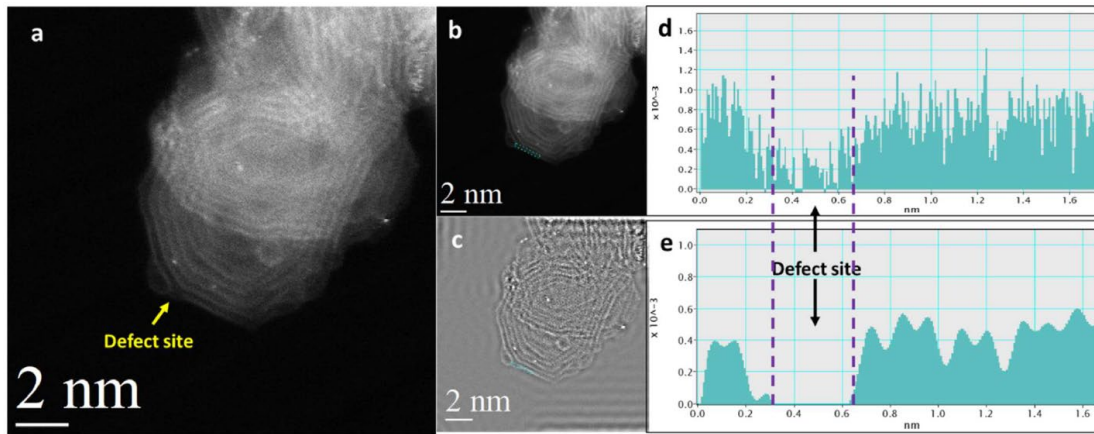


Figure 4.3 Defect sites in CNO. (a) HAADF micrograph showing the defect site in the outermost graphitic shell of a S-CNO, (b) indicates the position of the line profile (blue dashed box), (c) Fourier filtered image of (b) for improved clarity. (d) and (e) are line profiles across the defect sites in (b) and (c), respectively.

should be noted that the STEM micrograph is a two-dimensional (2D) projection of a three-

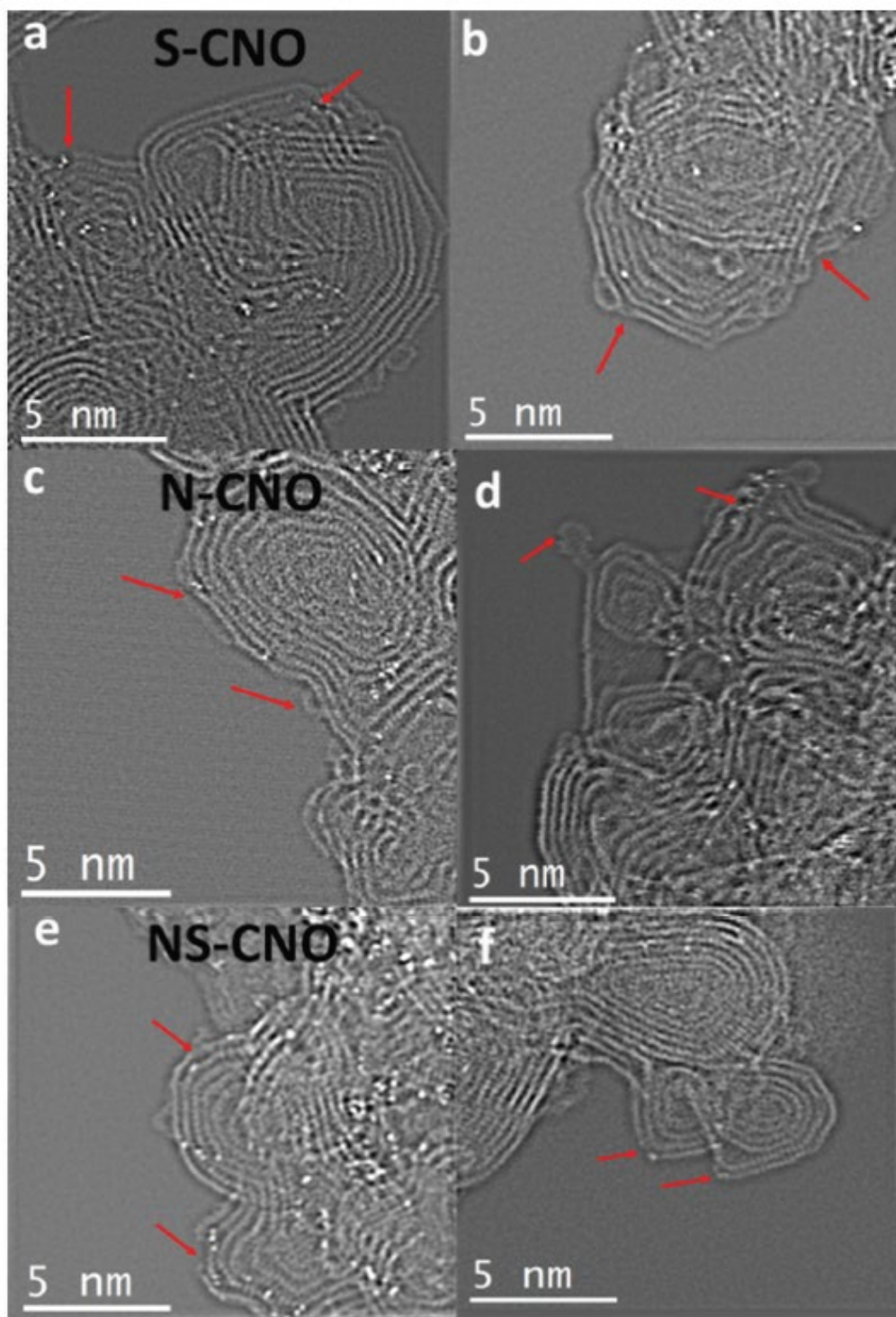


Figure 4.5 Filtered IFFT images showing defects in CNO shells. (a,b) sulfur-doped CNOs, (c,d) nitrogen-doped CNOs, and (e,f) sulfur and nitrogen codoped CNOs. (Defects marked with red arrows).

dimensional (3D) sample, and as such only the defects which are visible in 2D micrographs

were considered, therefore. It is worth noting, however, that since we are using a post-doping strategy, most of the dopant atoms are expected to remain in the outer few layers of the CNOs.

Table 4.1 Dopant configuration and location on CNOs.

Type	Number of CNO	Number of dopants	grouped dopant atoms				single atom dopants		Proximity to defect sites							
			2	3	>3	%			At the defect site		0-0.4 nm		0.41-0.7 nm		>0.7 nm	
NS-CNO	39	>209	23	10	3	42	121	58%	147	70%	34	16%	11	5%	17	8%
S-CNO	29	>82	7	3	1	32	55	67%	43	52%	4	5%	13	16%	22	27%
N-CNO	30	>67	8	4	-	42	39	58%	16	24%	3	4%	5	7%	43	64%

Table 4.2 Quantitative analysis of NS-CNO.

CNO	Dopant atom				Proximity to defect site									
	Single		Grouped		At defect site				0 - 0.4 nm		0.41 - 0.7 nm		>0.71nm	
	1	2	3	4	1	2	3	4	Number of dopants	Proximity (nm)	Number of dopants	Proximity (nm)	Number of dopants	Proximity (nm)
1	3				2								1	1.00
2	2												1	0.80
													1	>2.0
3	3		1						3	0.35	1	0.45		
									1	0.25				
									1	0.35				
4	3	1	1		1		1		1	0.24			1	> 2.0
													2	1.50
5	9	3	2		7	2	1		1	0.30				
									1	0.35				
									3	0.21			2	>2.0
6	5	1	1	1	1	1	1	1	1	0.35	1	0.55		
											1	0.57		
											1	0.56		
7	8	2			6	2			1	0.33	1	0.45		
8	7	1			4	1			1	0.40				
									1	0.35				
									1	0.25				

Table 4.2 (continued)

9	8	3			7	2			1	0.20				
									2	0.30				
10	6	4			3	3			1	0.35	1	0.45		
									1	0.30				
									2	0.30				
11-12	11	2	1	1	9	2	1	1	1	0.25			1	>2.0
13-14	7		1		4		1				1	0.45	1	>2.0
													1	0.80
15	3	1			1	1			1	0.25				
									1	0.35				
16	2				2									
17	2				1				1	0.30				
18-21	10	2			7	2			1	0.30	1	0.60		
									1	0.30				
22-23	3				2								1	1.10
24-29	9		1	1	7		1	1			1	0.70	1	1.00
30-32	6	1			6						2	0.60		
33-36	7	1	1		5	1			1	0.35			1	2.00
													3	>2.0
37-39	7	1	1		5		1		1	0.35				
									2	0.30				
									1	0.25				

Table 4.3 Quantitative analysis of S-CNO.

CN O	Dopant atom				Proximity to defect site									
	Single	Grouped			At defect site				0 - 0.4 nm		0.41- 0.7 nm		>0.71nm	
					1	2	3	4	Number of dopants	Proximity (nm)	Number of dopants	Proximity (nm)	Number of dopants	Proximity (nm)
1-4	12				8						1	0.45	1	0.9
											1	0.6	1	0.8
5-7	5	4	1		1	3	1		1	0.3	1	0.7		
											2	0.55		
											1	0.6		
											1	0.45		
8-10	2	1	1	1		1	1				4	0.5	1	>2.0
													1	>2.0
11-16	5	2			2	2							1	>2.0
													1	1.2
													1	0.8
17-24	10		1		2		1		1	0.3	1	0.7	1	1
									1	0.3			1	1
													1	0.8
													1	>2.0
													1	1.8
25-27	12				7								1	1.2
													1	>2.0
													1	>2.0
													1	>2.0
													1	>2.0
28-29	9								1	0.35	1	0.7	1	>2.0
													1	>2.0
													1	>2.0
													1	>2.0
													1	>2.0

Table 4.4 Quantitative analysis of N-CNO.

CN O	Dopant atom				Proximity to defect site									
	Single	Grouped			At defect site				0 - 0.4 nm		0.41- 0.7 nm		>0.71nm	
					1	2	3	4	Number of dopants	Proximity (nm)	Number of dopants	Proximity (nm)	Number of dopants	Proximity (nm)
1-4	4										1	0.50	1	1.60
													1	1.10
													1	0.80

Table 4.4 (continued)

5-9	6	2			1	1				1	0.55	1	1.40		
														1	1.00
														1	1.10
														2	>2.0
														1	>2.0
10-12	7	2			2					2	0.20	1	0.60	1	>2.0
										1	0.40			1	>2.0
														2	1.10
														1	>2.0
13-22	10	2	3		4	1	1							1	1.20
														1	1.20
														3	>2.0
														1	>2.0
														2	1.20
														1	>2.0
														1	>2.0
														3	1.00
														1	>2.0
23-24	4				1					1	0.60	1	>2.0		
														1	>2.0
25-27	5	1	1		1					1	0.50	1	>2.0		
														1	>2.0
														3	>2.0
														2	>2.0
														1	>2.0
28-30	3	1												1	>2.0
														1	>2.0
														1	>2.0
														2	>2.0

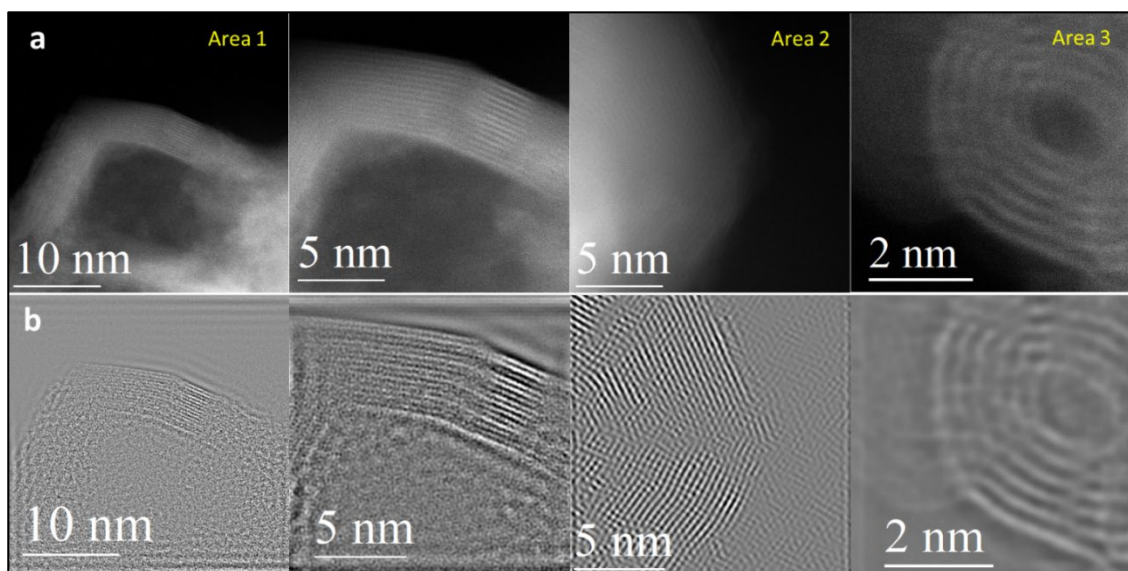


Figure 4.6 STEM micrographs of pristine CNOs. (a) HAADF micrographs and (b) the respective Fourier filtered images of pristine CNOs imaged at three different areas of the same sample.

It was also not possible to distinguish quantitatively whether any particular dopant atom was sulfur or nitrogen (or possibly oxygen) in the co-doped sample, due to unknown sample thickness and variation. In all cases dopants were identified qualitatively as atoms

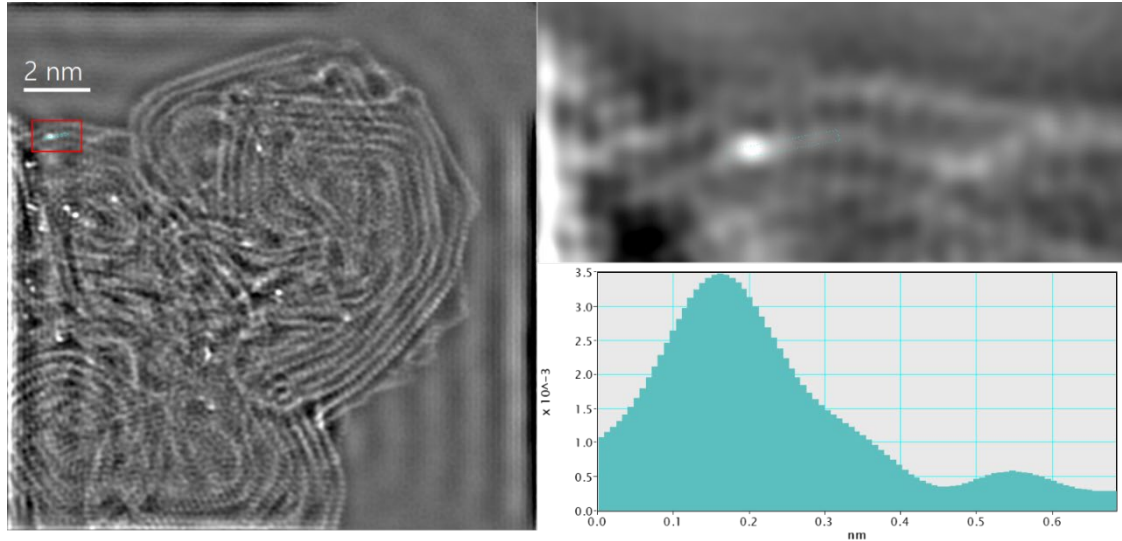


Figure 4.7 Line scan across C and S atoms in S-CNO sample (HAADF image).

with greater intensity (and therefore mass) than carbon. A control experiment was performed to confirm that the undoped pristine CNO starting material does not contain visible heteroatom dopants. The HAADF micrographs and corresponding filtered images (Figure 4.6) show samples free of contaminants and demonstrate that the heteroatoms observed in Figure 4.5 likely originate from S and/or N doping. Consistent with HAADF

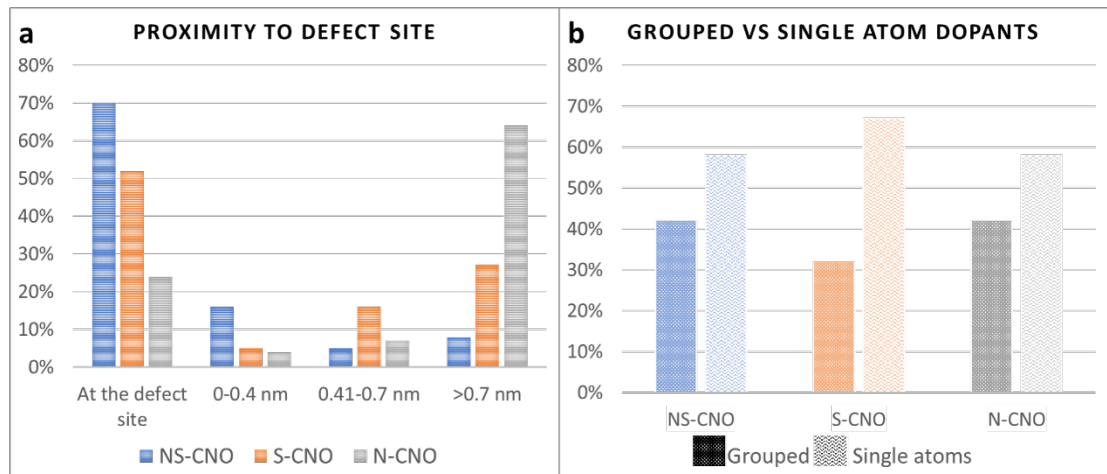


Figure 4.8 Histograms of dopant proximity and configuration in the three CNO samples. (a) Proximity of defect sites, and (b) single atom vs grouped.

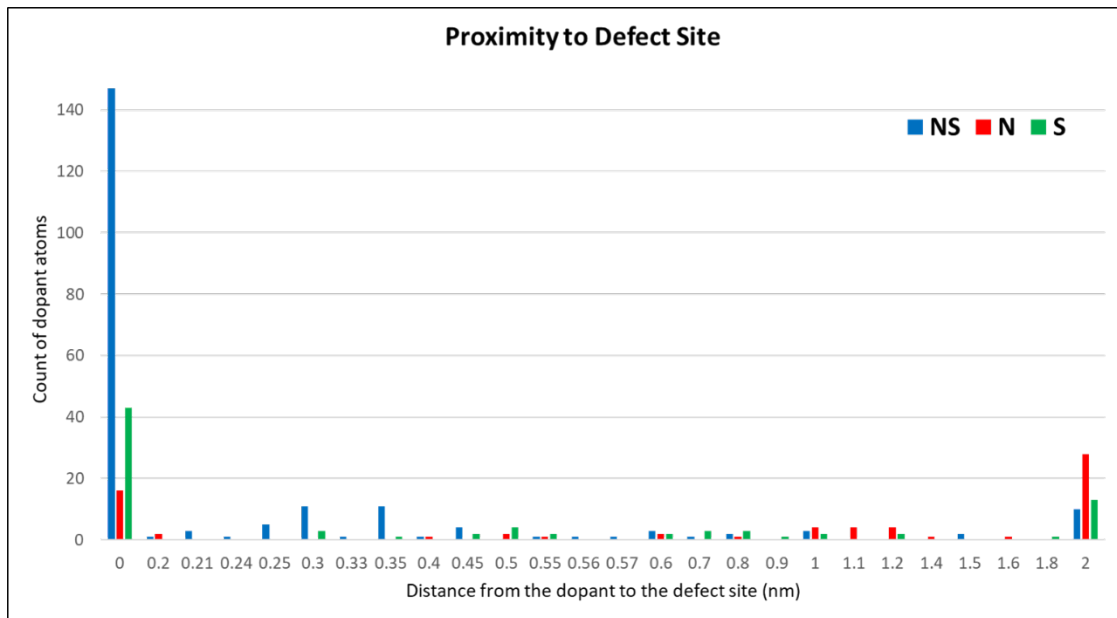
imaging, dopants in the S-CNO and NS-CNO samples were more easily identified due to their greater intensity (Figure 4.7).

The scattering intensity of electrons on this detector $\propto Z^{1.6-1.9}$

$$\text{Intensity ratio (from HAADF micrograph (Figure 4.6))} = \frac{3.5 \times 10^{-3}}{0.5 \times 10^{-3}} = 7$$

$$\text{Ratio between } Z^{1.9} \text{ of S and C} = \frac{16^{1.9}}{6^{1.9}} = 6.45$$

The results show that for NS-CNO, 86% of dopant atoms are located within <0.4 nm of the defect site, whereas for S-CNO and N-CNO, only 57% and 28% of dopant atoms reside within <0.4 nm of the defect site respectively (Figure 4.8a and Figure 4.9 (detailed histogram of Figure 4.8a with equal bin sizes)). While most of the dopants in NS-CNOs and S-CNOs are found at the defect sites or within close proximity to defects, N dopants in N-CNOs are significantly internalized and at longer distances from defects, where the dopants are presumed to be introduced. This is attributable to the smaller size of N with respect to S. The configuration of dopant atoms (whether single or grouped) is consistent



throughout the three samples (Table 4.1; and Figure 4.8b). In N-, S-, and NS-CNO samples, the ratios of single to grouped dopant atom configurations are 1:1.4, 1:1.8, and 1:1.4 respectively. Li *et al.* have reported that the defects are inferred to be located near high curvature locations on CNO and can be seen as blurry areas in TEM/STEM images, which is also consistent with our work.¹²⁴ STEM imaging and EELS reveals, therefore, the occurrence of dopant atoms and groups at close proximity to high curvature regions of the shell, in which defects are more prevalent.

Since all samples studied show distinct atomic configurations and distributions, the electronic properties of these samples might also be expected to be significantly different from one another. Accordingly, the ORR electrocatalytic activities of these samples were measured as a metric to differentiate the electronic properties. The ORR is one of the crucial reactions to occur in fuel cells and metal air batteries.¹³⁹ Typically, the oxygen

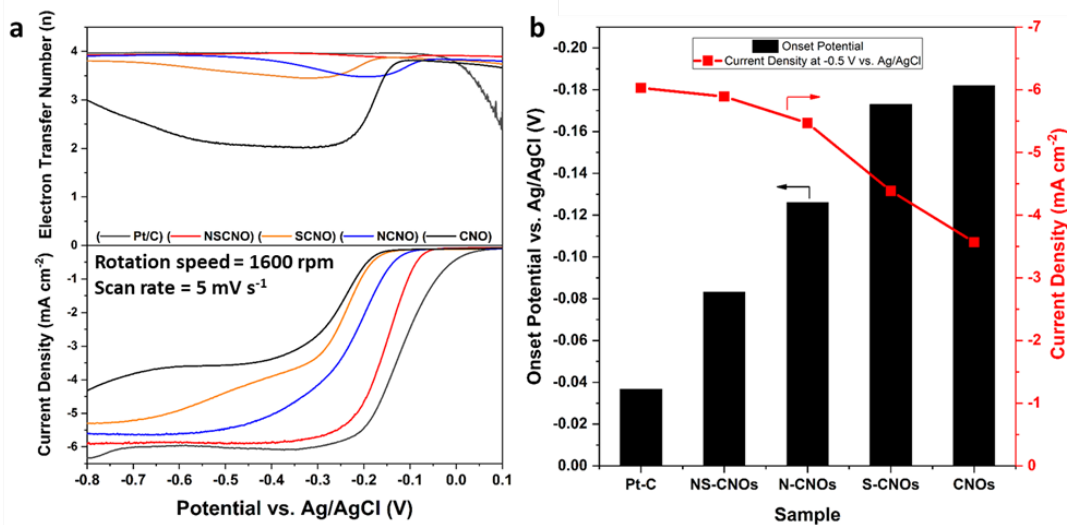


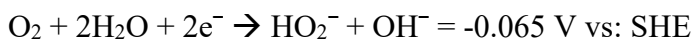
Figure 4.10 Determination of ORR activity by RRDE experiments. (a) LSV curves and electron transfer number (obtained by rotating RRDE at 1600 rpm while maintaining a scan rate of 5 mV s⁻¹) and (b) Current density and ORR onset potential for each sample. (The ORR activity measurements were performed Namal Wanninayake from the Kim group).

reduction occurring in the cathode side of a fuel cell is kinetically sluggish and more problematic compared to hydrogen oxidation occurring at the anode. It is imperative, therefore, to boost the kinetics of the ORR by developing advanced materials which are highly stable and durable. In an alkaline medium, the ORR proceeds either by a direct four-electron pathway or a two-electron peroxide pathway.¹⁴⁰

Direct four-electron pathway



Two-electron peroxide pathway



Out of these two pathways, the direct four-electron pathway is desirable due to its high efficiency. It has been proposed that heteroatom dopant atoms such as sulfur and nitrogen incorporated into a graphitic network are effective in inducing asymmetric charge distribution on the surface due to dissimilar electronegativity and size mismatch.^{118,129,141} The greater electronegativity difference between nitrogen and carbon induce an asymmetric charge density; the size mismatch between carbon and sulfur also yield an asymmetric charge density. Co-doped nitrogen and sulfur introduce unpaired electrons altering the charge and spin densities of the active domains. Sites with high spin and charge densities are known to be active for the adsorption of oxygen molecules during the ORR.^{124,130} Figure 4.10a shows LSV recorded for each catalyst sample.

The ORR performance of each tested catalyst was compared with the state-of-the-art 20% Pt-C catalyst, where the best ORR catalyst shows low-overpotential and a high current density. Figure 4.10b compares the onset potential and the current densities at -0.50

V vs. Ag/AgCl of each catalyst. It is noted that, out of all the metal-free catalysts investigated, NS-CNO show the lowest on-set potential and the highest current density (with current density similar to that of Pt-C). The N-CNO sample showed higher performance than the S-CNO sample. Undoped CNOs showed the worst performance. Intriguingly, all heteroatom-doped samples yielded electron transfer numbers close to four indicating the heteroatom dopant contribution towards the ORR. Since undoped CNOs do not contain heteroatoms, this material primarily generates peroxide via a two-electron pathway. The narrow four-electron window of undoped CNOs (-0.1 V-0.0 V) is a mathematical artifact due to a near-zero ring current (I_r). These observations are well consistent with the other literature findings.¹⁴²

Overall, all heteroatom-doped CNOs exhibit enhanced activities for the ORR compared to undoped CNOs, in terms of higher current densities and lower onset potentials. Among doped CNOs, NS-CNOs show the best performance, closest to that of Pt/C. Remarkable improvements in the activities of doped CNOs clearly reflect that various active sites are formed by incorporating S and N dopants in CNOs. From STEM analysis, N-CNO, S-CNO, and NS-CNO contain dopants in the form of groups at or closer to defect sites. These groups could form unique active sites that can reduce the adsorption barrier of the O₂ molecule and catalyze the ORR. Previous computational studies identified bi- and tri-pyridinic N sites as potential catalytic sites.^{143,144} These sites can have dopant arrangements as groups that we captured by STEM analysis in this study. In NS-CNO where N and S atoms are in proximity, in particular, the electron and spin densities on the catalyst surface are significantly promoted relative to N-CNO or S-CNO, leading to the best ORR activity. Combined with the structural analysis presented, NS-CNO suggests a

concerted mechanism of catalysis for the ORR, requiring both heteroatom dopant and high-curvature defective regions of the CNO.

4.3 Conclusions

In this work, for the first time, single and grouped dopant atoms in S-, N- and NS-CNO samples were resolved using STEM imaging. Micrographs show that the onion like concentric shell structure of the CNO was retained during the fabrication and doping steps, and EELS characterization confirms the successful doping of all three CNO samples. Defects within CNO shells are seen clearly in HRSTEM images and analysis shows that 86% of dopant atoms in the NS-CNO sample are located within <0.4 nm of the defect, while the dopant atoms in S- and N-CNO are located at greater distances from the defects, revealing a possible key structural feature for catalysis. Greater catalytic efficiency for the ORR for co-doped samples with respect to singly-doped counterparts suggests the synergistic effect of dopants and the dopant proximity to the defect may play a key role in the catalytic mechanism.

CHAPTER 5. UNCOVERING THE STRUCTURE AND STABILITY OF
THERMOELECTRIC LANTHANUM(IV) TELLURIDE-NICKEL COMPOSITES
USING HIGH-RESOLUTION AND *IN SITU* TEM

5.1 Introduction

For the past 50 years, NASA has relied exclusively on thermoelectric materials in RTGs to power their missions in deep-space such as the Viking and Curiosity rover on Mars, and the 1977 Voyager missions. An alloy based on $\text{Si}_{0.8}\text{Ge}_{0.2}$ was one of the earliest bulk thermoelectric composites that NASA used in RTGs at the initial stages.^{145–151} The RTGs use the heat generated from radioactive decay of ^{238}Pu to heat one side of the thermocouple with the other side kept cold due to the reduced temperature of space.¹⁵² The phenomenon of direct conversion of a temperature difference to electric potential (Seebeck effect) or the electric potential to a temperature difference (Peltier effect) is known as the thermoelectric effect and the thermoelectric efficiency of a material is given by its dimensionless figure of merit (zT) value which can be expressed using the following equation:

$$zT = \frac{S^2 \sigma T}{K} \quad (1)$$

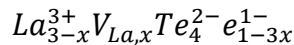
Where S is the Seebeck coefficient, σ is the electrical conductivity, T is the absolute temperature, and K is the thermal conductivity. The total thermal conductivity (K) is the combination of the electronic (K_{el}) and the lattice (K_l) thermal conductivities.^{145,146,150,153}

Preliminary work has been performed in this field to achieve the "phonon-glass electron-crystal" phenomenon by exploring ways to maintain low thermal conductivity. In another approach, the scaling of sample size combined with low dimensionality may give

independent control over the σ , S , and K parameters, which can simultaneously enhance zT .^{146,154,155} Nanoscale solid-state thermoelectric materials have proven to be reliable and clean energy recovering sources for generating electricity from residual heat. In contrast to bulk materials, the thermal and electrical conductivities in nano thermoelectrics can be independently controlled by scaling down the size of the material.^{145,146,156} The traditional thermoelectric materials have only shown capabilities in moderate performance with conversion percentages as low as 6-6.5%. The new thermoelectric materials such as n-and p-type filled skutterudites and rare earth metal composites, however, have increased thermoelectric efficiencies by twofold, when compared with traditional thermoelectrics.¹⁵⁷ Various approaches have been scouted to enhance the thermoelectric efficiency by incorporating nanoparticles into the microstructure and improving grain refinements.¹⁵⁸⁻¹⁶⁰ The concept of bulk nanocomposite thermoelectrics evolved as a result of combining the ideas of improved bulk and low dimensional thermoelectric materials, and, therefore, retain the superior characteristics of both of these counterparts that result in enhanced efficiency.¹⁶¹ The structure of a thermoelectric nanocomposite comprises a thermoelectric semiconductor host material and nanoparticle (NP) inclusions and these structural modifications lead to reduced thermal conductivity by increasing phonon-scattering and consequently enhance the zT of the resulting thermoelectric composite. Previous studies illustrate that these alterations in the structure also aid in controlling electrical conductivity and/or the Seebeck coefficient *via* electron/energy filtering.^{158,162-166} Here, the metal NP islands act as barriers and obstruct the movement of electrons through thermoelectric host material. Only the electrons with adequate energy levels are, therefore, will be able to pass over the barrier, which can facilitate the increase in Seebeck coefficient by lowering

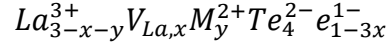
electrical conductivity.¹⁶⁷ Toprak *et al.* demonstrate that the nanocomposite of bismuth telluride results in a high density of grain boundaries which lowers its thermal conductivity and enhances thermoelectric efficiency.¹⁶² In another study carried out with similar material, nanocomposite $\text{Bi}_{2-x}\text{Sb}_x\text{Te}_3$ shows a 40% increase in zT when compared with its bulk counterpart, due to increased phonon scattering at interfaces.¹⁵⁹ Furthermore, analogous research has been conducted with similar materials such as $\text{In}_{0.53}\text{Ga}_{0.47}\text{As}$ nanocomposite with ErAs nanoparticles to increase the thermoelectric performance, and theories have also been developed to elucidate the relationship between the improvement in the Seebeck coefficient values with the high energy dependence of electron scattering at the interface between the metallic nanoparticle and the semiconductor host.^{163,164}

Lanthanum telluride, $\text{La}_{3-x}\text{Te}_4$ is a state-of-the-art n-type thermoelectric material, with an optimized zT of 1.1 at 1273 K ($x=0.23$) and is self-doped through La vacancies. Computational studies of $\text{La}_{3-x}\text{Te}_4$ indicate that La plays a vital role in defining the density of states (DOS) in the conduction band, and that the material possesses glass-like K_I values revealing excellent electric transport properties at 1273 K.^{157,168–171} The carrier density in $\text{La}_{3-x}\text{Te}_4$ is controlled by the valence of La, where La^{3+} provides three electrons to the crystal structure and Te uses 2 of the 3 electrons to complete its valence. The stoichiometry of the $\text{La}_{3-x}\text{Te}_4$ crystal is shown below (La vacancies are denoted by V_{La})¹⁷²:



At $x=0$, there is one free electron per formula unit leading to metallic properties (formula: La_3Te_4) and the introduction of La vacancies results in an insulating behavior with no free electrons (formula: $\text{La}_{2.67}\text{Te}_4$).^{147,168} When La^{3+} is substituted with a divalent metal cation

(M^{2+}), the chemical environment changes as follows (y denotes the number of substituted M^{2+} cations):¹⁴⁷



The substitution of La^{3+} with divalent metal ions such as Ca^{2+} and Yb^{2+} has been explored in previous work where a better control over the carrier density with improved zT values (1.2-1.3 at 1273 K) was achieved.^{147,157,172} A DFT study combined with Boltzmann transport theory explains that the band structure of $La_{3-x}Te_4$ has a strong influence on improved thermoelectric efficiency at temperatures above 1000 °C compared to legacy n-type thermoelectric materials. The Seebeck coefficient is enhanced due to the increased energy dependence of the DOS, which is explained by the sharp increase of the DOS ascribable to the presence of heavy bands in the energy-dependent analysis of the DOS ($N(E)$). The effect of charge localization induced by La vacancies is, therefore, negated by forming conduction channels in the band structure.^{168,173} Very recently, Ma *et al.* have introduced a high-temperature thermoelectric composite material comprising a $La_{3-x}Te_4$ semiconductor host and rare earth metal NP inclusions (Ni and Co) which explains a methodology to enhance the mechanical properties while maintaining a high efficiency by decoupling thermal and electronic transport properties.¹⁷⁴ We hypothesize that the coherent $La_{3-x}Te_4/Ni$ interfaces permit low electrical resistivity, but are distributed efficiently to maintain a low thermal conductivity. A thorough understanding of the salient features of the $La_{3-x}Te_4/Ni$ interfaces is of critical importance in understanding its improved thermoelectric efficiency. The characteristics and stability of these interfaces remain relatively unexplored, however, at ambient or elevated temperatures. Moreover, the significance of investigating the stability of $La_{3-x}Te_4/Ni$ over its operating conditions has

been already established in preceding studies.^{146,163,175} The use of an *in situ* TEM technique enables the opportunity to mimic the working environment of the RTG in deep-space which is high temperature and low pressure, opening up the ability to study the tiniest salient structural details of these cutting-edge thermoelectric composite materials in their locality.

Here, we report a detailed structural characterization of the $\text{La}_{3-x}\text{Te}_4/\text{Ni}$ interface using high-resolution and *in situ* TEM and EDS techniques, at ambient and elevated temperatures in high-vacuum conditions. High-resolution TEM (HRTEM) analysis reveals the epitaxial correlation of the two interfacing phases, cubic $\text{La}_{3-x}\text{Te}_4$ and Ni, at ambient temperature. The *in situ* TEM and EDS studies performed using pristine, oxidized, and partially oxidized $\text{La}_{3-x}\text{Te}_4\text{-Ni}$ samples indicate that in the presence of oxygen, Ni diffusion and interface degradation occurs at temperatures as low as 400 °C. The pristine oxygen-free $\text{La}_{3-x}\text{Te}_4/\text{Ni}$ interface is, however, stable up until temperatures of ~800 °C, above which Ni diffusion becomes prominent.

5.2 Structure and stability of thermoelectric $\text{La}_{3-x}\text{Te}_4\text{-Ni}$ composites

The TEM micrographs of the FIB lift-out lamella attached to the FIB lift-out grid and transferred to the TEM via AP holder are shown in Figure 5.1(b-d). The spherical regions apparent in TEM (Figure 5.1(b-c)) and STEM high-angle annular dark-field (HAADF) images are identified as nickel (Ni) nanoparticles (NPs) in the EDS map (Figure 5.1e). EDS maps of lanthanum (La) and tellurium (Te) indicates the homogenous distribution of these elements in the $\text{La}_{3-x}\text{Te}_4$ matrix (Figure 5.1(f-g)). The EDS spectrum

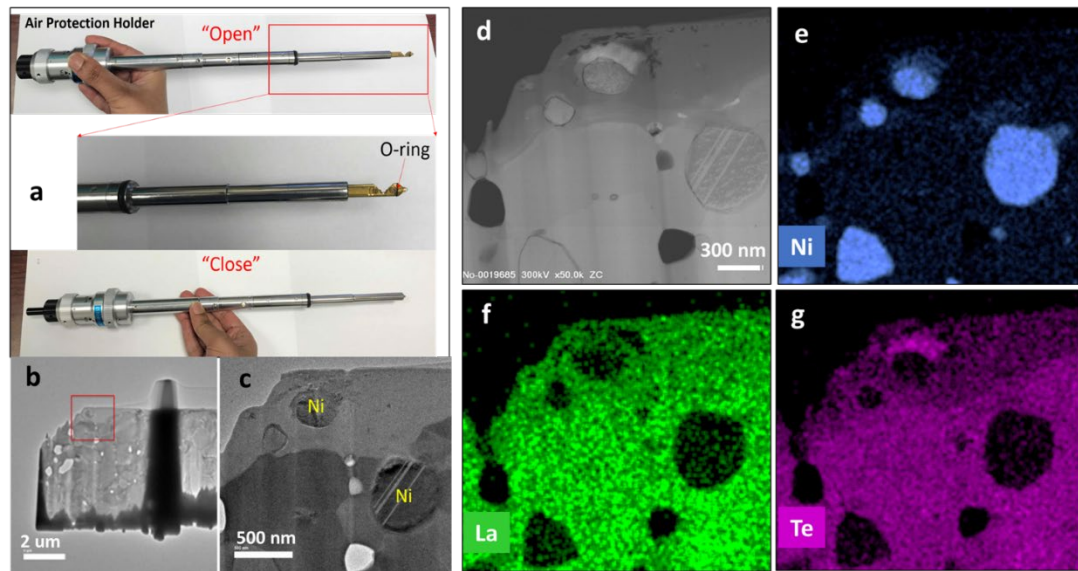


Figure 5.1 Sample preparation. (a) Air Protection (AP) holder compatible with both Hitachi FIB-SEM and TEM/STEM systems. (b-c) TEM, (d) STEM micrographs, and EDS elemental maps of (e) Ni, (f) La, and (g) Te of a FIB lift out lamella of $\text{La}_{3-x}\text{Te}_4\text{-Ni}$ sample.

Confirms the presence of La, Te, and Ni in the sample. The absence of an O peak indicates successful sample preparation and transfer processes (Figure 5.2).

A previous study on this material by Ma *et al.* reports that the Ni and Co composited $\text{La}_{3-x}\text{Te}_4$ show a great enhancement in zT when compared with the pristine $\text{La}_{3-x}\text{Te}_4$ material.¹⁷⁴ It was postulated that the presence of an interface layer (such as NiO: an insulator with high thermoelectric power), between the Ni metal nanoparticle and the $\text{La}_{3-x}\text{Te}_4$, could positively contribute to this improvement in zT . Other studies of thermoelectric composites have shown the importance of the interface between the thermoelectric semiconductor and metal inclusions suggesting the interface plays a role in scattering electrons preferentially and that the epitaxial relationship between two interfacing phases

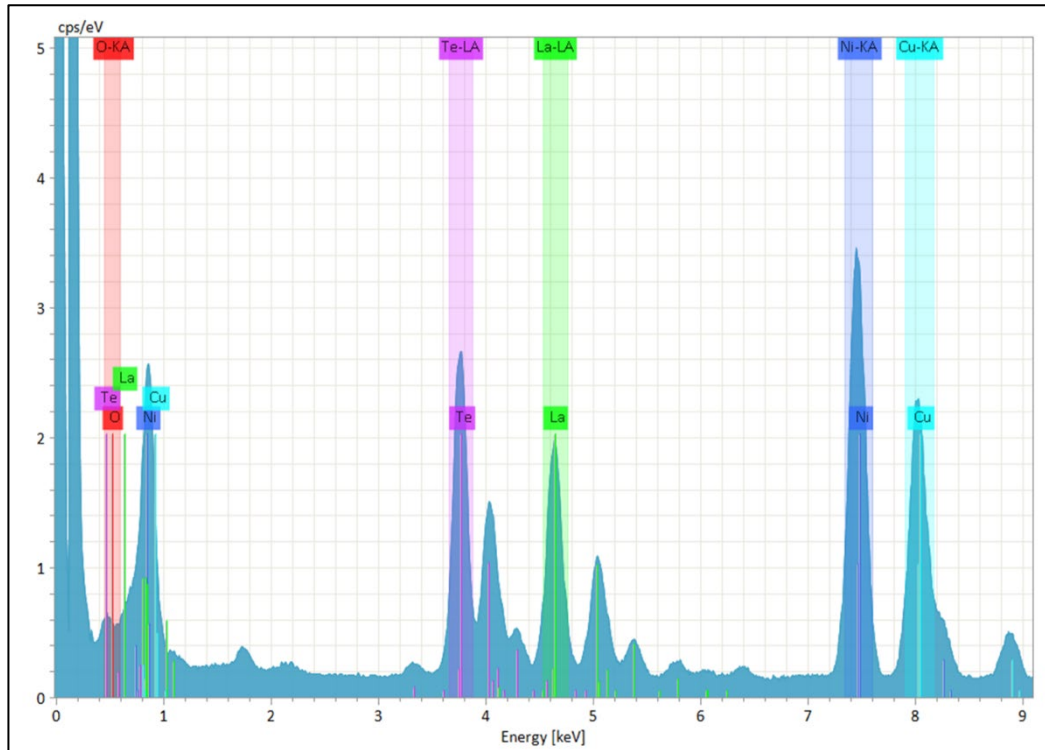


Figure 5.2 EDS spectrum of Figure 1 (d-g) showing the presence of La, Te, and Ni in the $\text{La}_{3-x}\text{Te}_4$ -Ni sample. The absence of an O peak indicates successful sample preparation and transfer processes.

can facilitate low thermal conductivity.^{163,175} The structural characterization of the $\text{La}_{3-x}\text{Te}_4$ is of key importance, therefore, in the present study.

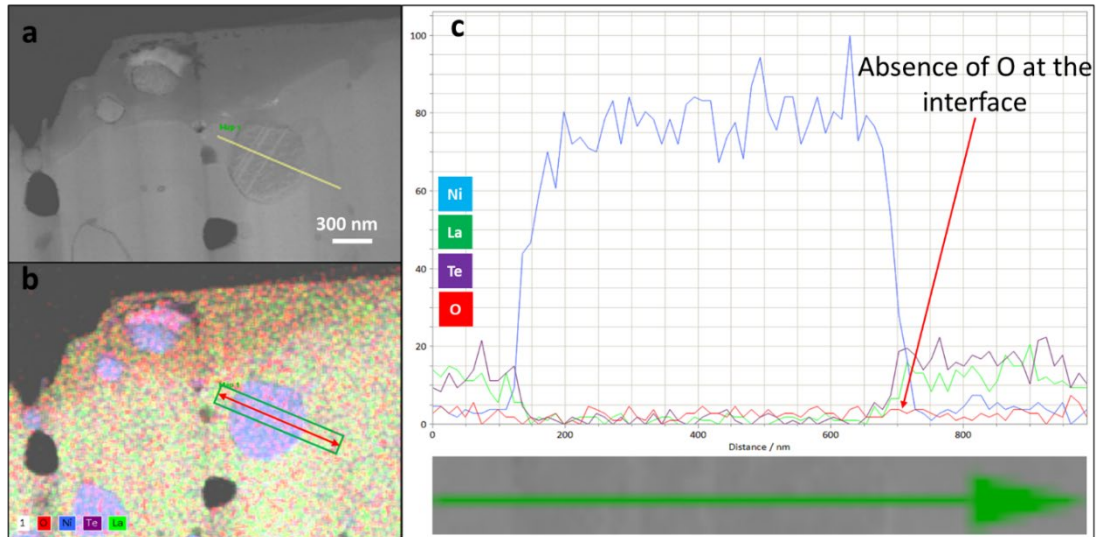


Figure 5.3 EDS line scan across the interface of $\text{La}_{3-x}\text{Te}_4$ matrix and Ni particle. (a) STEM image and (b) composite EDS image indicating the region where the line scan has been performed. (c) The red line corresponding to oxygen signal lies flat through the scan indicating the absence of O at the interface and throughout the sample.

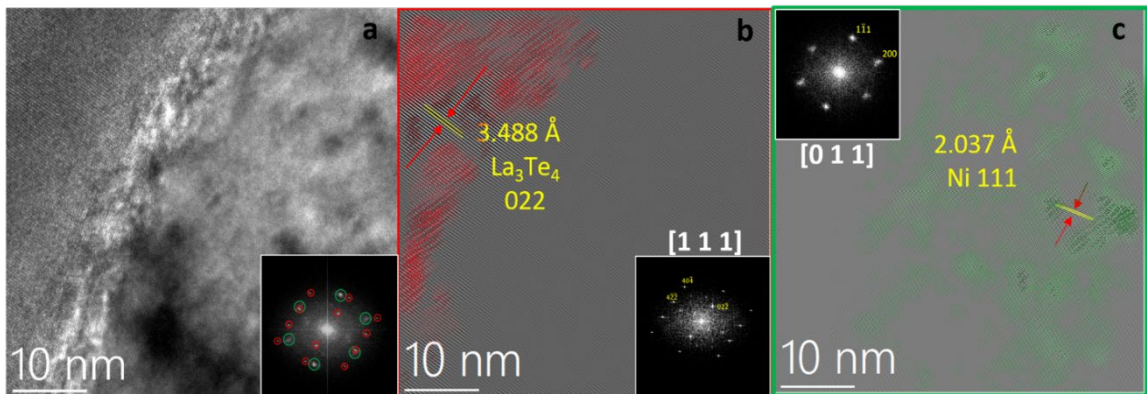


Figure 5.4 High-resolution TEM characterization of the $\text{La}_{3-x}\text{Te}_4$ -Ni interface. (a) HRTEM image of $\text{La}_{3-x}\text{Te}_4$ -Ni interface. Inset shows the FFT image; the set of red spots correspond to $\text{La}_{3-x}\text{Te}_4$ matrix and green spots correspond to Ni nanoparticle inclusions, which have been separately masked, and Fourier filtered to generate (b) and (c) respectively. The insets of (b) and (c) shows these highly crystalline areas can be indexed to zone axes of La_3Te_4 [111] and Ni [011] respectively.

The EDS line scan performed across two $\text{La}_{3-x}\text{Te}_4/\text{Ni}$ interfaces (Figure 5.3(a-b)) confirms the absence of an oxide or any other interfacial layer at the interface (the oxygen signal lies flat throughout the line scan region) (Figure 5.3c). A thorough examination of individual elemental line scans of La, Te, and Ni suggests that the Ni nanoparticle is tightly bonded to the matrix without any gap in the structure.

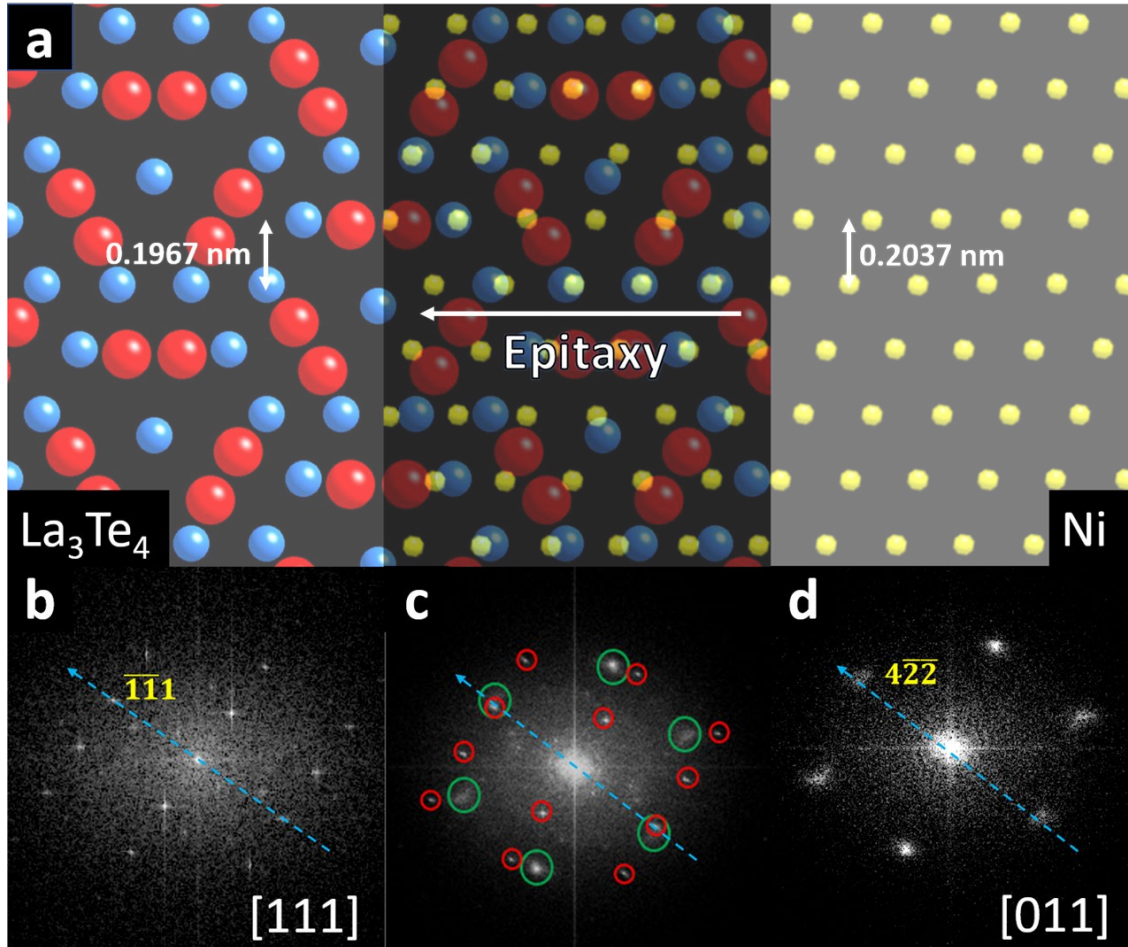


Figure 5.5 Epitaxial relationship between $\text{La}_{3-x}\text{Te}_4$ and Ni at the $\text{La}_{3-x}\text{Te}_4/\text{Ni}$ interface. (a) Shows the epitaxial direction (white arrow) in the interfacing phases of $\text{La}_{3-x}\text{Te}_4[111]$ and Ni $[011]$ (simulated image from CrystalMaker® software (red spheres=La, blue spheres=Te, and yellow spheres=Ni)). The FFTs (b-d) obtained from the $\text{La}_{3-x}\text{Te}_4$, $\text{La}_{3-x}\text{Te}_4/\text{Ni}$ interface, and Ni can be indexed to cubic phases of $\text{La}_{3-x}\text{Te}_4 [111]$ (red circles in (c)) and Ni $[011]$ (green circles in (c)). The direction of epitaxy in the interfacing phases is further indicated (b-c) using the parallel blue-dashed arrows along $(\bar{1}\bar{1}1)$ and $(4\bar{2}\bar{2})$ diffraction spots of cubic $\text{La}_{3-x}\text{Te}_4$ and Ni, respectively.

Figure 5.4 shows the high-resolution TEM characterization of the $\text{La}_{3-x}\text{Te}_4/\text{Ni}$ interface. The HRTEM micrograph (Figure 5.4a) shows that the two interfacing phases, $\text{La}_{3-x}\text{Te}_4$ and Ni are highly crystalline. The FFT obtained at this region (inset of Figure 5.4a) shows two sets of spots, which have been identified separately ($\text{La}_{3-x}\text{Te}_4$ (red circles) and Ni (green circles)) by generating the FFTs from the individual interfacing phases (insets of Figure 5.4(b-c)). Once identified, the two sets of spots were individually masked to generate their respective inverse FFTs and false-colored for better representation ($\text{La}_{3-x}\text{Te}_4$ (red) and Ni (green)) (Figure 5.4(b-c)). Figure 5.4(b-c) delineates the crystalline facets spaced at 3.488 Å and 2.037 Å corresponding to La_3Te_4 (022) and Ni (111), and their corresponding FFTs can be indexed to the [111] and [011] zones of cubic La_3Te_4 and Ni, respectively.

As mentioned above, the epitaxial relationship between the thermoelectric semiconductor host and the metal nanoparticle inclusions at the interface is of utmost importance. Using the CrystalMaker® software package, the simulation in Figure 5.5a demonstrates the epitaxial matching of $\bar{1}\bar{1}1$ ($\text{La}_{3-x}\text{Te}_4$) and $4\bar{2}\bar{2}$ (Ni) facets at the interface. The epitaxial direction is shown in a solid white arrow in Figure 5.5a and is further indicated by parallel blue-dashed arrows drawn across $\bar{1}\bar{1}1$ and $4\bar{2}\bar{2}$ diffraction spots in the FFTs of $\text{La}_{3-x}\text{Te}_4$ and Ni, respectively (Figure 5.5(b-d)).

$\text{La}_{3-x}\text{Te}_4\text{-Ni}$ is a state-of-the-art thermoelectric nanocomposite material that is designed for deep-space RTG applications and is intended to be operated at a high-temperature and low-pressure environment. The *in situ* TEM technique is, therefore, an indispensable tool to execute a detailed study of this type of material since it can closely simulate the RTG environment in deep-space within the microscope.

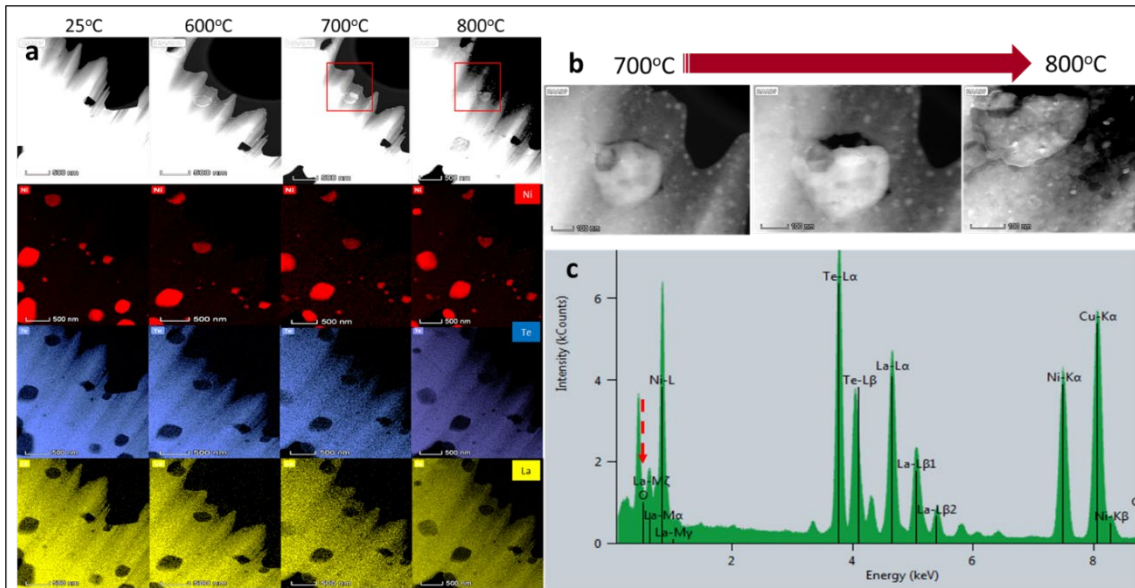


Figure 5.6 *In situ* TEM study of a pristine (non-oxidized) $\text{La}_{3-x}\text{Te}_4\text{-Ni}$ sample. (a) STEM micrographs (top row in (a)) and EDS elemental maps collected at 25, 600, 700 and 800 °C during an *in situ* heating experiment show Ni (red) diffusion in to $\text{La}_{3-x}\text{Te}_4$ matrix and interface degradation ~ 700 °C (area inside the red square in STEM micrographs). The $\text{La}_{3-x}\text{Te}_4/\text{Ni}$ interface degradation can be clearly observed in the magnified STEM micrographs recorded in 700-800 °C temperature range (b). (c) EDS spectrum shows the absence of an oxygen signal (dashed red arrow) in the sample.

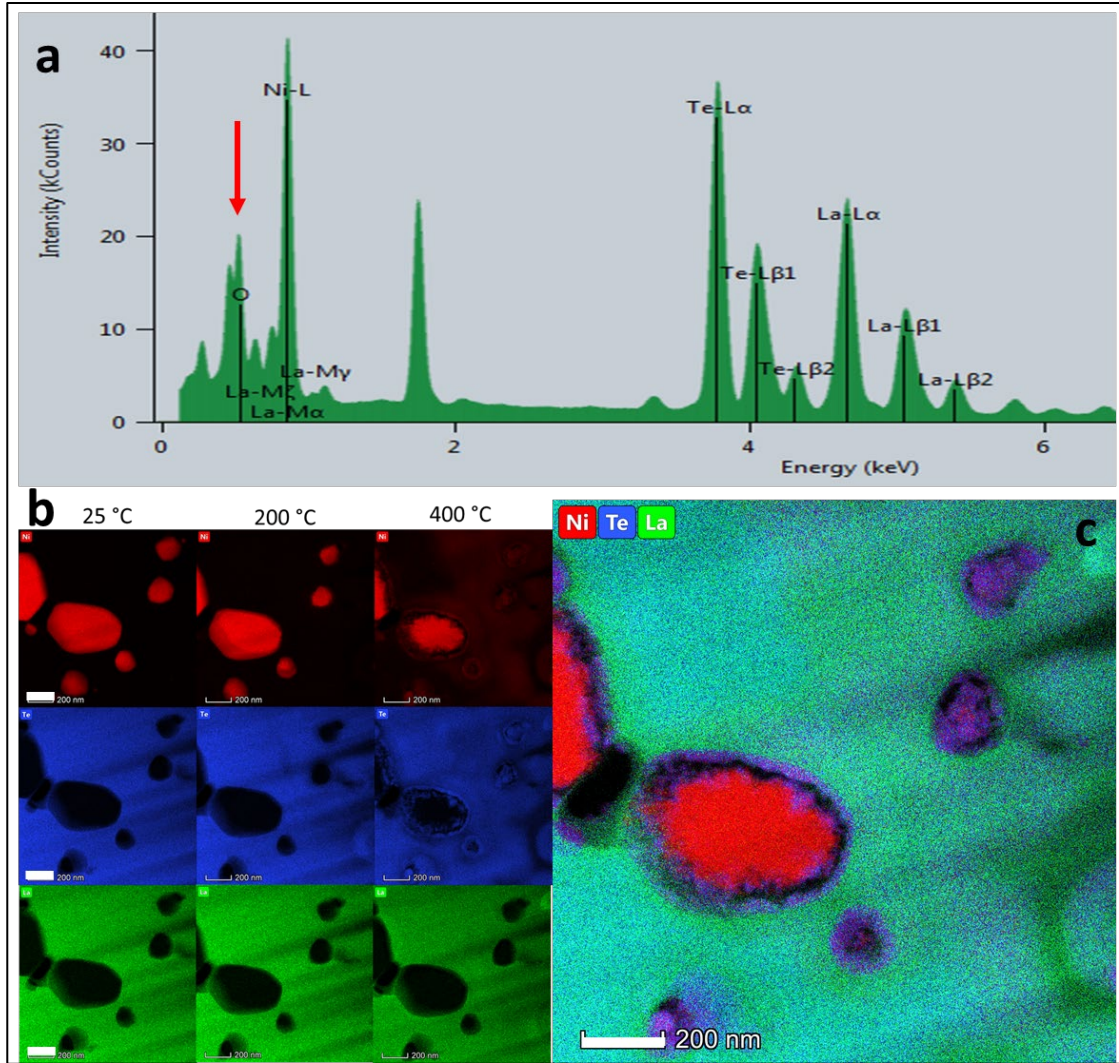


Figure 5.7 *In situ* TEM study of an oxidized $\text{La}_{3-x}\text{Te}_4\text{-Ni}$ sample. (a) EDS spectrum taken at the region of interest (ROI) shows a distinctive oxygen signal (red arrow). (b) EDS elemental maps collected at 25, 200, and 400 °C during an *in situ* heating experiment show Ni (red) and Te (blue) interdiffusion forming a nickel telluride layer at the interface at 400 °C (purple later in the composite image (c)). La (green) does not change throughout the heating treatment. Scale bar is 200 nm (b-c).

An *in situ* TEM study of the pristine (non-oxidized) $\text{La}_{3-x}\text{Te}_4\text{-Ni}$ sample (heating rate: 10 °C min^{-1}) is shown in Figure 5.6. The dashed red arrow at 0.525 keV in Figure 5.6c, where the oxygen $\text{K}\alpha$ peak would appear in the EDS spectrum, is evidence of the absence of oxygen in the sample. The HAADF micrographs and EDS elementals maps of La, Te, and Ni acquired at 25, 600, 700 and 800 °C indicate that the oxygen-free $\text{La}_{3-x}\text{Te}_4/\text{Ni}$

these deep-space missions. The effect of oxygen on the kinetics of $\text{La}_{3-x}\text{Te}_4/\text{Ni}$ interfaces, therefore, cannot be neglected.¹⁷⁷ Figure 5.7 illustrates the *in situ* TEM analysis of a fully oxidized $\text{La}_{3-x}\text{Te}_4\text{-Ni}$ sample. The solid red arrow in the EDS spectrum acquired at the region of interest (ROI) (at 25°C – before heating) (Figure 5.7a) indicates a distinctive oxygen peak. The sample was heated from 25 to 450 °C using the Protochips® fusion heating system, at a heating rate of 10 °C min⁻¹ and TEM and EDS elemental maps were collected at 25, 100, 200, 300, and 400 °C (Figure 5.7b). The temperature-dependent EDS and TEM analyses indicate that at around 400 °C, Ni and Te interdiffusion takes place and the composite EDS map (400 °C) suggests a newly formed NiTe layer at the interface (purple layer in Figure 5.7c). Subsequently, after reaching 400 °C, the Ni nanoparticle and the interface start to collapse. This observation is consistent with previous studies reported in the literature on Ni diffusion into bismuth telluride at low temperatures such as 200 °C,¹⁷⁵ and the formation of a NiTe layer at the $\text{Bi}_2(\text{Te, Se})_3/\text{Ni}$ interface at ~100 °C, in the presence of oxygen.¹⁷⁸ This may be due to the potential formation of TeO_3 when oxygen is present in the sample. At temperatures above 400 °C, TeO_3 undergoes thermal decomposition resulting in the basic tellurate, TeO_2 .^{179,180} Marczenko *et al.* reports that reducing agents can reduce tellurium (IV) to elemental Te.¹⁸¹ The possibility exists that the reducing environment created in the TEM column due to the very low oxygen partial pressure (high vacuum: $\sim 10^{-7}$ Torr), facilitates the reduction of TeO_2 to Te, which has a reported melting point of 449 °C and appears to be in the temperature region the interface degradation occurs in the current study (400-450 °C). Such high-vacuum conditions are also typical of a deep-space environment.

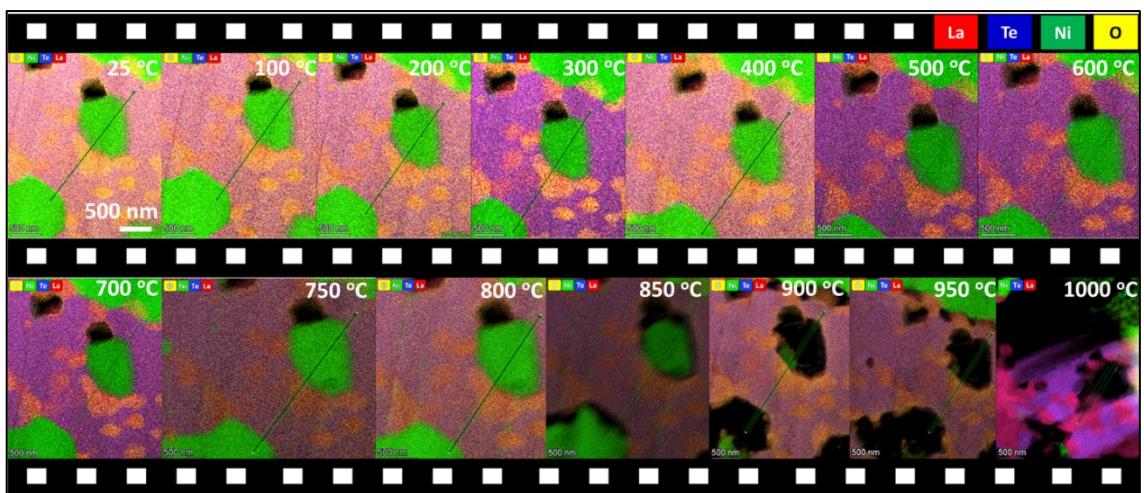


Figure 5.9 *In situ* TEM study of the partially oxidized $\text{La}_{3-x}\text{Te}_4\text{-Ni}$ sample (same area as Figure 5.8 or small area in the blue box shown in the figure 5.8a). The EDS elemental maps collected at the temperature range of 25-1000 °C, further confirm that the $\text{La}_{3-x}\text{Te}_4/\text{Ni}$ interface remains intact without any Ni diffusion up to 700 °C in the absence of oxygen (these results are complementary to the observations made in Figure 5.6 for the pristine interface).

Figures 5.8 and 5.9 show an *in situ* heating TEM experiment conducted using a partially oxidized $\text{La}_{3-x}\text{Te}_4\text{-Ni}$ sample. Two examples of oxidized and non-oxidized $\text{La}_{3-x}\text{Te}_4/\text{Ni}$ interfaces present in the sample are shown in Figure 5.10 (note the presence and absence of the oxygen $\text{K}\alpha$ signal in their respective EDS spectra (denoted by red solid and dashed arrows)). When the ROI (Figure 5.8: red square) at 25 °C (Figure 5.8a) is compared with the same region at 750 °C (Figure 5.8b), it is apparent that the $\text{La}_{3-x}\text{Te}_4/\text{Ni}$ interfaces at the oxidized areas (Figure 5.8a: black-dashed square regions at 25 °C) have fully degraded before reaching 750 °C. The EDS line scan (Figure 5.8c) performed at the area indicated by the white rectangle (Figure 5.8a) of the EDS elemental map reveals the

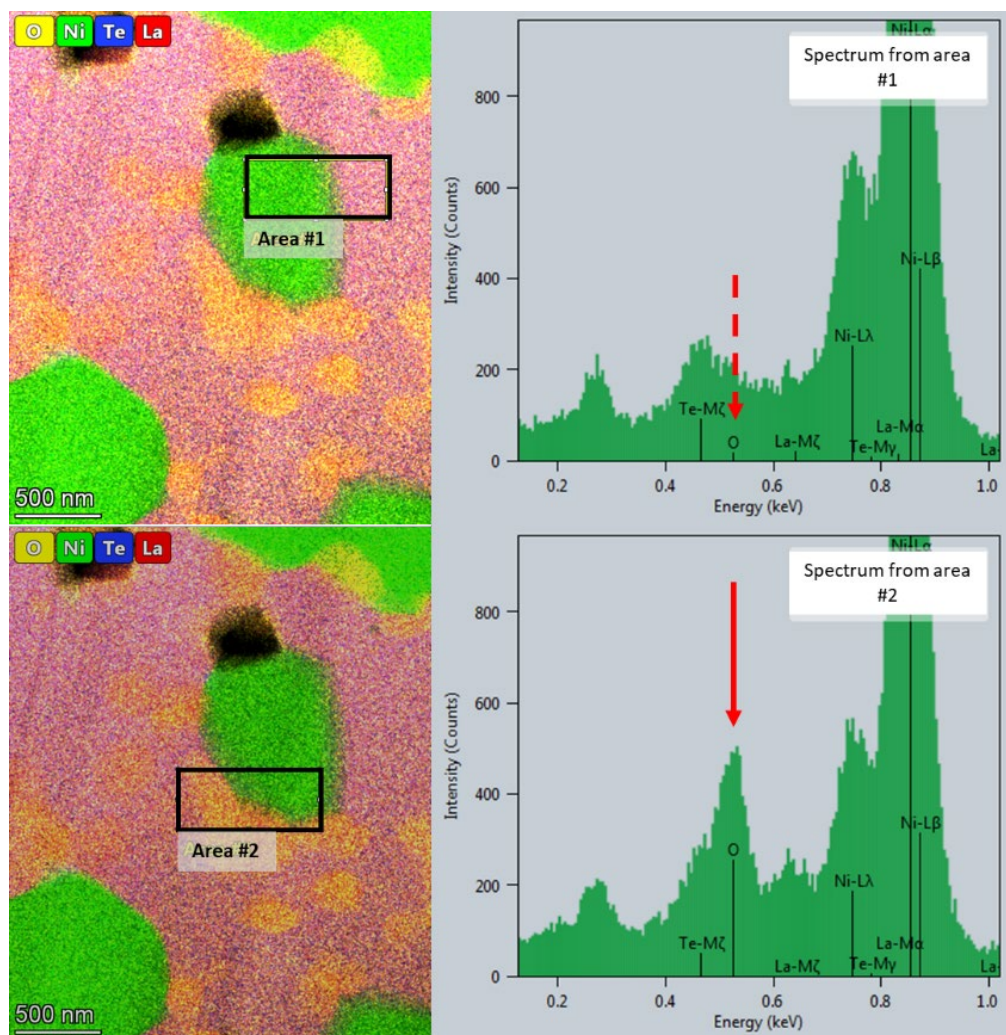


Figure 5.10 Two EDS spectra representing two areas from the ROI of the partially oxidized $\text{La}_{3-x}\text{Te}_4\text{-Ni}$ sample in Figure 6(a). Area 1 and 2 represents non-oxidized and oxidized interfaces, respectively (red dashed and solid arrows indicate absence and presence of the O signal in EDS spectra, respectively).

presence of two non-oxidized interfaces at 25 °C (black arrows in Figure 5.8c), which remain intact, however, even at 750 °C. This experimental observation is consistent with the results obtained in the previous two *in situ* heating experiments (Figures 5.6-5.7), and thus signifies the reproducible nature of our experimental findings. The temperature-dependent EDS elemental maps collected (25-1000 °C) at a non-oxidized interface is shown in Figure 5.9, which reveals that Ni diffusion and interface degradation initiates at

800-850 °C and is fully decomposed by 950 °C, which is consistent with the results obtained in Figure 5.6.

5.3 Conclusions

In this study, a detailed analysis of the structure and stability of $\text{La}_{3-x}\text{Te}_4\text{-Ni}$ composites and their interfaces were carried out in ambient and elevated temperatures at high vacuum. The devised TEM sample preparation process is proven to be highly successful and resulted in no oxygen contamination of the sample. THE HRTEM analysis indicates the two interfacing phases are epitaxial with each other along the $\bar{1}\bar{1}1$ and $4\bar{2}\bar{2}$ crystal facets in $\text{La}_{3-x}\text{Te}_4$ and Ni, respectively, which implies the possible low thermal conductivity pathways.¹⁶³ The *in situ* TEM studies performed over the working temperature of these thermoelectric materials (25-1000 °C) using three pristine, oxidized, and partially oxidized $\text{La}_{3-x}\text{Te}_4\text{-Ni}$ samples reveal that the Ni diffusion and interface degradation of a pristine $\text{La}_{3-x}\text{Te}_4$ /Ni interface occurs at temperatures higher than 750 °C, whereas the presence of oxygen at these interfaces accelerates interface degradation processes to occur at a lower temperature of about 400 °C. The current study provides a detailed perspective on the structure and stability of a high-performance thermoelectric composite material over its working conditions (high-temperature and low-pressure), of direct relevance when designing next-generation thermoelectric materials with a longer lifespan for potential applications in RTGs.¹⁴⁶

CHAPTER 6. STABILIZATION OF METASTABLE CUBIC HAFNIA AND HAFNIUM PYROVANADATE FROM CORE-SHELL ARRANGEMENT OF PRECURSORS

Parts of this chapter are taken from “N. A. Fler, M. P. Thomas, J. L. Andrews, G. R. Waetzig, O. Gonzalez, G. Liu, B. S. Guiton and S. Banerjee, *Nanoscale*, 2019, 11, 21354 DOI: 10.1039/C9NR07316G” Reproduced by permission of The Royal Society of Chemistry.¹⁸²

6.1 Introduction

Metastable crystal structures with atomic arrangement somewhat altered from the thermodynamic phase correspond to relatively shallower local minima on free energy diagrams but can in many instances be trapped under ambient conditions.^{183–186} The large amounts of energy inputted in conventional high-temperature ceramic and metallurgical processing methods result in reaction mixtures being able to approach equilibrium efficiently. In contrast, synthetic approaches that can situate the material in a local minimum under specific constraints (temperature, pressure, chemical doping) can often be rapidly “quenched”, enabling kinetic trapping of the metastable phase.^{183,185,187–192}

At nanoscale dimensions, the increased stabilization of the tetragonal polymorph of HfO₂ derived from surface and strain energy differentials with the monoclinic polymorph overcomes the bulk free energy preference for the latter polymorph.^{3,187} The transformation of metastable tetragonal ZrO₂ to the thermodynamically stable monoclinic polymorph provides an effective means of energy dissipation and is used industrially for transformation toughening.

Reducing the size of the complementary metal oxide semiconductor field effect transistor, led to the requirement of a very thin gate dielectric SiO₂ layer, which resulted in large leakage currents. HfO₂, has been proposed as the preferred oxide with high dielectric constant (κ) and high bandgap to replace SiO₂.^{193,194} HfO₂ and ZrO₂ are commonly referred to as the “twin oxides” owing to the similarities in the properties of these two materials that arise from the closely matched atomic radii of their cations, which indeed is a direct result of lanthanide contraction.^{195,196} HfO₂ has the low symmetry (seven-coordinated hafnium atoms) monoclinic structure (P21/a) at room temperature and undergoes a sequence of structural phase transitions at elevated temperatures. Around 1720 °C, HfO₂ adopts the higher-symmetry (eight-coordinated hafnium atoms) tetragonal phase (P42/nmc) and transforms to a much higher symmetry (eight-coordinated hafnium atoms) cubic HfO₂ (Fm3m) at temperatures above 2600 °C and is retained until 2758 °C where it is congruently melted.^{197,198} Much higher dielectric constants have been reported for high temperature HfO₂ phases, cubic (κ ~29) and tetragonal (κ ~70) when compared to monoclinic phase HfO₂ (κ ~16-18). Therefore, significant attention has been given for stabilizing these high temperature phases of HfO₂.¹⁹⁶ Some attempts have been reported to stabilize cubic HfO₂ by creating oxygen vacancies using dopants.¹⁹⁹ Kita *et al.* have observed, structural phase transition at low temperature by doping HfO₂ with Yttrium to stabilize of high κ phase HfO₂.²⁰⁰ Previous work illustrates that the stabilization of tetragonal HfO₂ under ambient conditions is much more challenging and requires scaling to dimensions <4 nm as compared to the ca. 30 nm critical size for ZrO₂.^{3,187,201}

While dimensional confinement and twin domain control have emerged as viable means of accessing the tetragonal phase of HfO₂, an altogether new strategy is required to

stabilize the cubic polymorph of HfO₂ and is demonstrated here based on a core-shell precursor strategy. The intimate mixing and small diffusion lengths within core-shell VO₂@HfO₂ nanocrystals enable the facile stabilization of phase-pure cubic HfO₂ at low temperatures. In contrast, facilitating interdiffusion under oxidative conditions yields HfV₂O₇, a negative thermal expansion (NTE) material in the MX₂O₇ material family that exhibits isotropic negative thermal expansion.^{202–205} The development of a facile synthetic route to this material further mitigates a significant impediment to its industrial use within zero thermal expansion composites.

Atomic-scale observation of the structure is of vital importance to understand the structural transformation mechanism at a fine-scale, hence opens up the opportunity to manipulate the transformation.⁴ The stabilization of cubic hafnia with larger κ would be crucial in potential technological applications when weighed against the room temperature monoclinic phase. Real-time observations of structural transformations of cubic HfO₂ and HfV₂O₇ are, therefore, of crucial significance as it could provide experimental confirmation for all the theoretical work done in this field.

Herein, we provide the structural proof that a combination of epitaxial growth of HfO₂ onto VO₂ nanocrystals and interdiffusion, followed by etching of the vanadium oxide core, enables the stabilization of metastable cubic HfO₂ under ambient conditions, using high-resolution and *in situ* transmission electron microscopic (TEM) techniques.

6.2 Stabilizing metastable cubic HfO₂ from a core-shell nanorod precursor

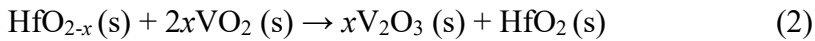
VO₂ nanowires with lateral dimensions of 180 ± 70 nm and lengths of 1.6 ± 0.9 μ m and quasi-spherical VO₂ nanocrystals with diameters of 44 ± 30 nm have been prepared

(Banerjee group, University of Texas A&M) as discussed in detail in Chapter 2. The synthetic approach to core-shell positioning of the precursors and the process used to prepare metastable cubic HfO₂ and the negative thermal expansion material, HfV₂O₇, is illustrated in Figure 6.1. An amorphous HfO₂ shell is first deposited onto VO₂ nanocrystals or VO₂ nanowires by hydrolysis and condensation of a hafnium alkoxide precursor as per:



This reaction is performed at low temperature (4 °C) to prevent homogeneous nucleation of HfO₂ nanocrystals. The abundant hydroxyl groups on the surfaces of the VO₂ nanocrystals allow for the formation of V–O–Hf oxo linkages as observed previously in the deposition of SiO₂ shells.^{206,207}

Annealing in Ar to 650 °C results in the emergence of rhombohedral V₂O₃ and crystalline cubic HfO₂ phases, as shown in the powder XRD studies, illustrating oxygen diffusion from the core to the shell concomitant with crystallization consistent with the more electropositive nature of hafnium:



Based on first principles calculations, the average oxygen vacancy formation energy in amorphous HfO₂ is 6.97 eV, but is notably increased to 7.29 eV in crystalline HfO₂.^{208,209} In other words, crystallization is accompanied by a significant destabilization of oxygen vacancies, which are healed by diffusing oxygen from the VO₂ core to the HfO₂

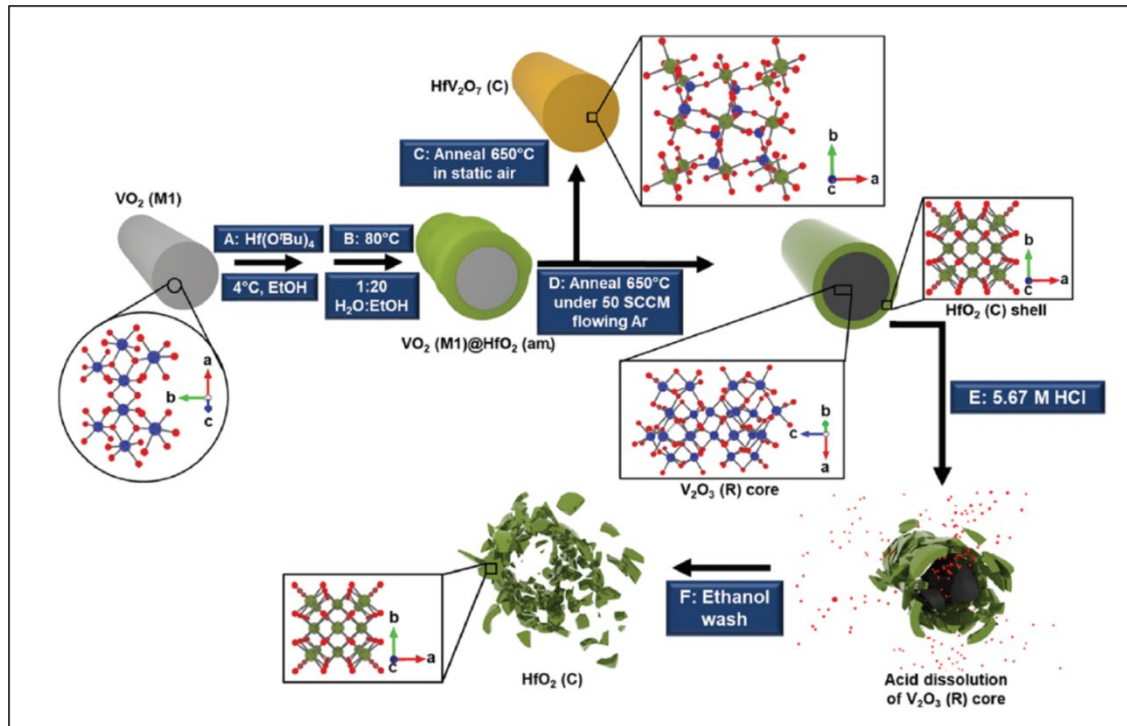


Figure 6.1 Schematic depiction of the synthesis of cubic HfO₂ and HfV₂O₇ from VO₂ and HfO₂ precursors arranged in a core–shell arrangement. (A) Hf (O^tBu)₄ is deposited onto the surface of VO₂ nanowires and nanocrystals crystallized in the M1 phase and hydrolyzed in (B) to deposit an amorphous HfO₂ shell. The VO₂@amorphous-HfO₂ core–shell structures can either be (C) annealed under static air at 650 °C to yield cubic HfV₂O₇, or (D) annealed under flowing Ar to produce rhombohedral V₂O₃ with a cubic HfO₂ shell. (E) Acid treatment of V₂O₃@HfO₂ with a 5.67 M aqueous solution of HCl results in the dissolution of the V₂O₃ core and after (F) washing with ethanol yields phase-pure cubic HfO₂, which is recovered upon centrifugation.

shell. As such, crystallization of the HfO₂ shell is accompanied by a reduction in the concentration of oxygen vacancies and concomitant reduction of the vanadium (IV) oxide to vanadium (III) oxide. Acid etching of the core-shell structure leaves behind cubic HfO₂ as the only crystalline phase. No HfV₂O₇ contamination is observed for materials obtained

by this method.²¹⁰ The core-shell disposition of the oxide precursors, the establishment of

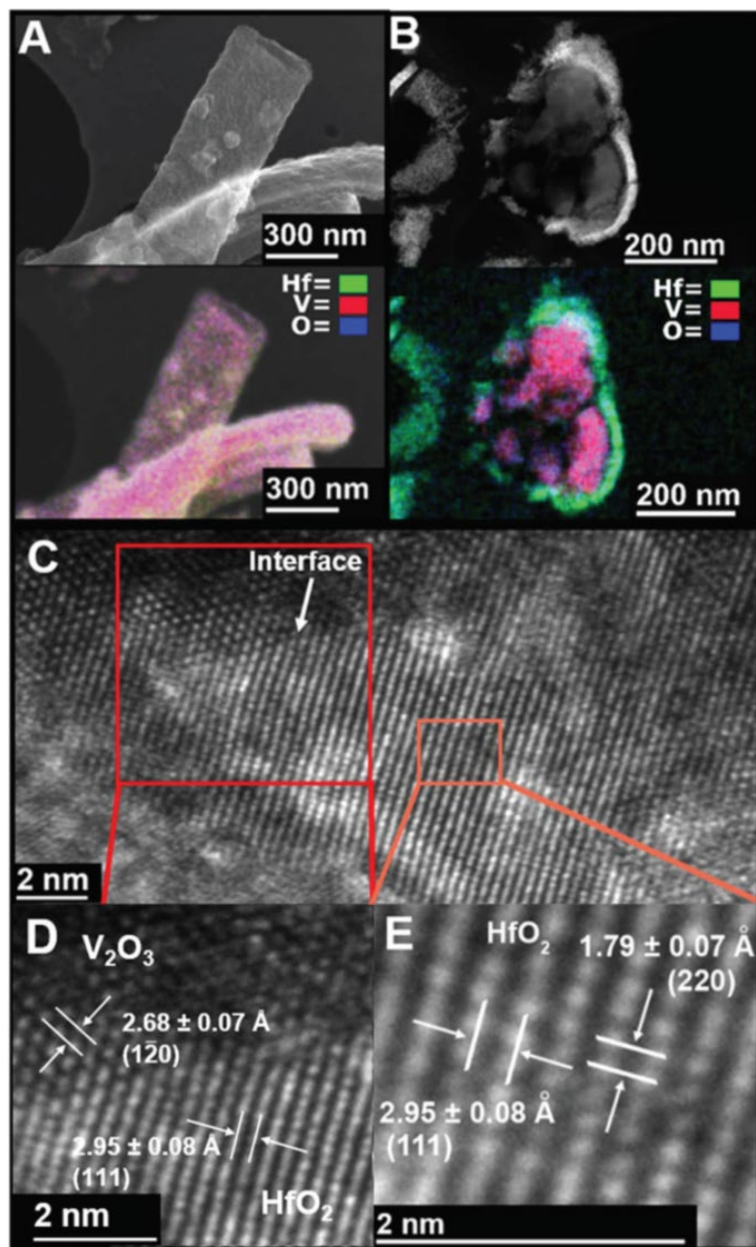


Figure 6.2 Imaging and compositional mapping of $V_2O_3@HfO_2$ core-shell structures. (A) STEM image of annealed $V_2O_3@HfO_2$ and corresponding EDS map illustrating the vanadium oxide core surrounded by a hafnium oxide shell. (B) Cross-sectional STEM image and EDS map of an ultramicrotomed core-shell nanowire. It is apparent that V (red) is highly concentrated within the core, whereas the Hf signal (green) is concentrated along the shell. (C and D) High-resolution TEM images depicting the epitaxial interface between rhombohedral V_2O_3 and cubic HfO_2 . Lattice spacings corresponding to rhombohedral V_2O_3 (PDF 85-1411) and cubic HfO_2 are delineated. (E) A magnified image of cubic HfO_2 domains within the shell.

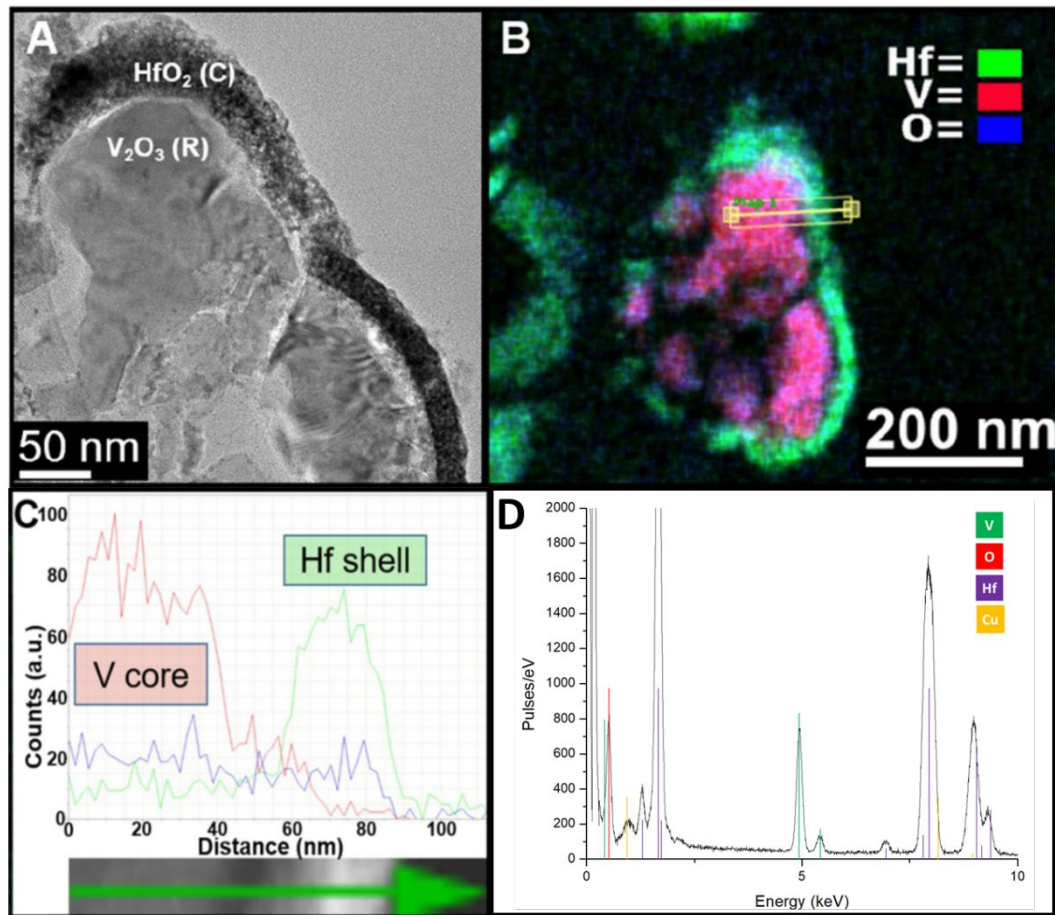


Figure 6.3 Cross-sectional TEM image and EDS line scan of an ultramicrotomed $V_2O_3@HfO_2$ core-shell nanowire. A) Cross-sectional TEM image of a $V_2O_3@HfO_2$ core-shell nanowire; B) corresponding EDS map of the $V_2O_3@HfO_2$ nanowire; and C) EDS line scan along the arrow in panel B. The vanadium signal (red) is highly concentrated within the core, whereas the Hf (green) signal derives predominantly from shell with oxygen (blue) distributed throughout the nanowire.

a crystallographically related interface between rhombohedral V_2O_3 and cubic HfO_2 , and etching of the vanadium oxide core to yield freestanding cubic HfO_2 have been examined using transmission electron microscopy and energy dispersive X-ray spectroscopy (EDS). Preliminary TEM and scanning electron microscopy (SEM) studies revealed VO_2 nanowires encased by an amorphous HfO_2 shell, in which the M1 VO_2 reduces to rhombohedral V_2O_3 and yields $V_2O_3@HfO_2$ core-shell particles with a cubic HfO_2 shell upon annealing under Ar at 650 °C for 25 min.¹⁸² The SEM analysis further indicated that

the shell is polycrystalline with faceted plate-like crystallites protruding from the surface of the nanowires and the cubic HfO_2 nanocrystals after acid etching of the rhombohedral V_2O_3 core.¹⁸² The core-shell configuration is further confirmed by examining of microtomed nanowires. Figure 6.2A and B show low-magnification STEM images of core-shell $\text{V}_2\text{O}_3@ \text{HfO}_2$ nanowires obtained upon annealing alongside an EDS map illustrating the core-shell arrangement of the vanadium and hafnium oxide domains. Figure 6.2A shows a panoramic view, whereas Figure 6.2B exhibits a cross-sectional image and EDS map acquired for an ultramicrotomed nanowire. This image shows that vanadium (red) is

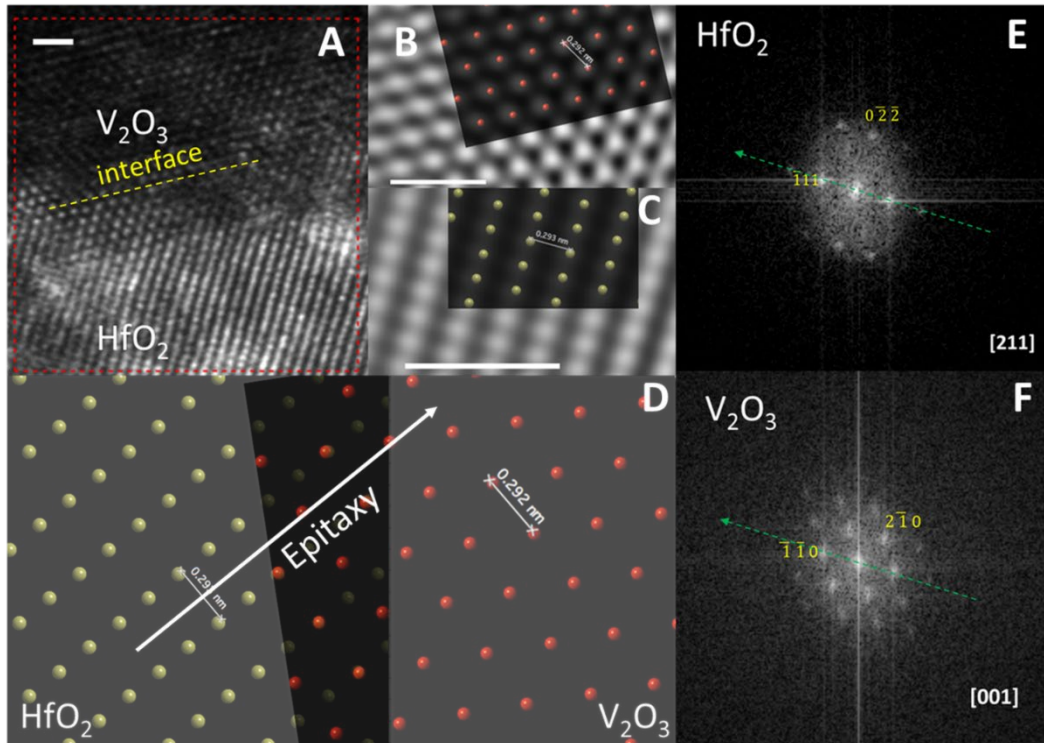


Figure 6.4 The scale bars of (a-c) indicate 1 nm. (a) TEM image of the interface of HfO_2 and V_2O_3 . (b) and (c) are Fourier filtered TEM images of two interfacial phases, V_2O_3 and HfO_2 , respectively. The superimposed red and olive color spheres represents V and Hf atoms, respectively. (d) shows the epitaxial direction (white arrow) in the interfacial phases (simulated image from CrystalMaker® software). The FFTs (e and f) obtained from (a) for the two interfacial phases can be indexed to $[211]$ and $[001]$ zone axes of cubic HfO_2 and rhombohedral V_2O_3 , respectively.

concentrated within the core of the structure, whereas hafnium (green) is concentrated within the shell. Further evidence of the core-shell structure is shown in Figure 6.3, which shows a cross-sectional view of an ultramicrotomed nanowire as well as an EDS line scan that further confirms the core-shell structure with Hf concentrated within the shell and vanadium within the core. Some V content is detected within the shell likely derived from the outwards diffusion of vanadium cations facilitated by the miscibility of the two cations.²¹⁰ The lattice-resolved HRTEM images in Figure 6.2C and D demonstrate the epitaxial matching between the rhombohedral V_2O_3 core and the cubic HfO_2 shell. The direction of the epitaxy in the interfacing phase is further indicated in Figure 6.4A-D. Figure 6.4E and F show the parallel green-dashed arrows along $(\bar{1}11)$ diffraction spots of cubic HfO_2 and $(\bar{1}\bar{1}0)$ diffraction spots of rhombohedral V_2O_3 , which confirms the epitaxy between two phases. Figure 6.2D and E delineate lattice spacings of $2.95 \pm 0.08 \text{ \AA}$

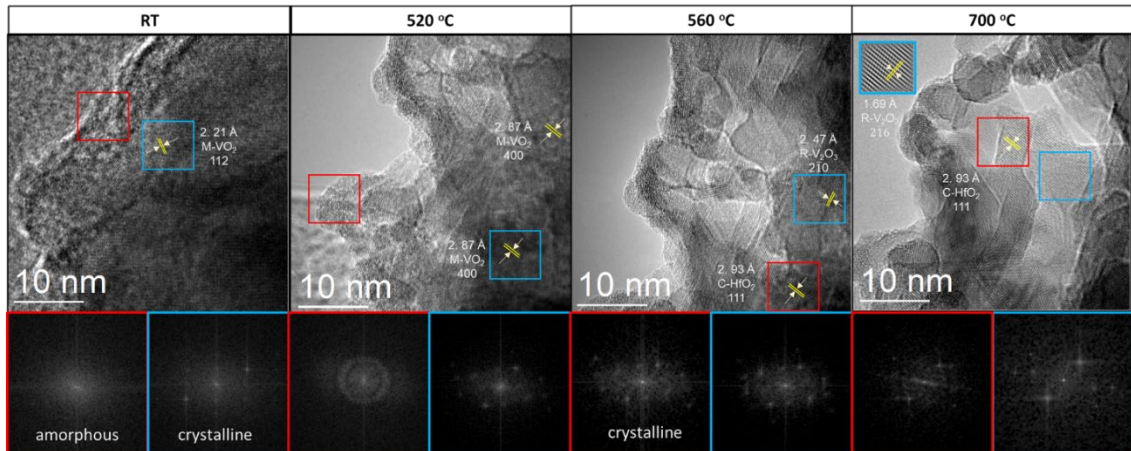


Figure 6.5 TEM images and accompanying FFTs corresponding to *in situ* heating of $HfO_2@VO_2$ core-shell particles. The heating rate is $5 \text{ }^\circ\text{C min}^{-1}$. The red squares delineate HfO_2 domains. The blue squares denote VO_2 or V_2O_3 domains. corresponding to the separation between (111) planes of cubic- HfO_2 and $2.68 \pm 0.07 \text{ \AA}$

corresponding to the separation between $(1\bar{2}0)$ planes of rhombohedral V_2O_3 . Indeed, this epitaxial matching is critical to the nucleation of cubic HfO_2 .

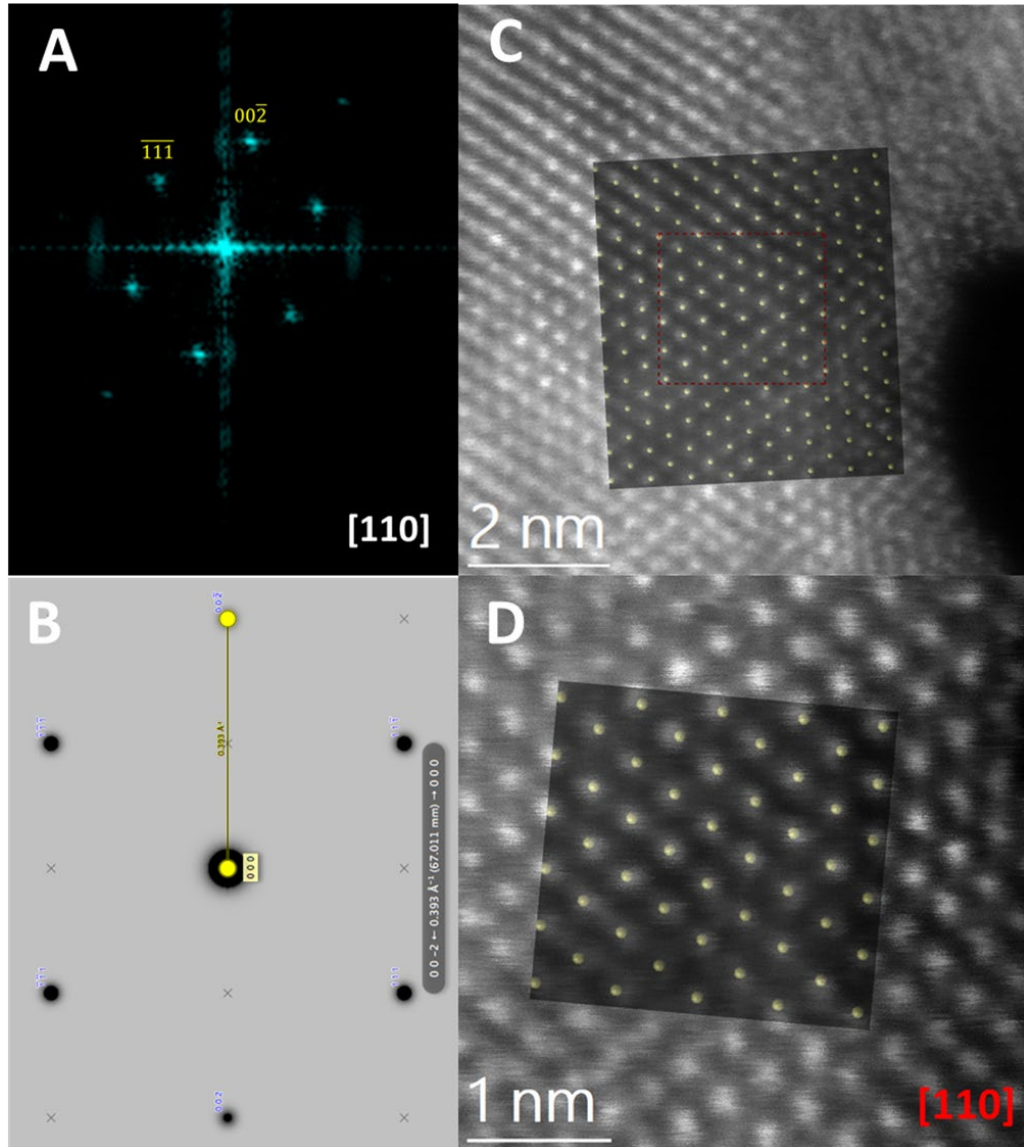


Figure 6.6 Stabilized cubic hafnia. (A-B) HAADF image of cubic HfO_2 along the $[110]$ zone axis. The superimposed olive spheres are Hf atomic column positions in the $[110]$ zone as predicted using CrystalMaker® software. (C-D) An FFT obtained at region (A), indexed to $[110]$ zone of cubic HfO_2 and simulated diffraction pattern (down the same zone) simulated from CrystalMaker® (SingleCrystal) software, respectively.

The dynamical evolution of VO₂ nanoparticles coated with amorphous HfO₂ shells upon thermal annealing has been examined by *in situ* TEM. Figure 6.5 shows high-resolution *in situ* TEM images along with corresponding Fast Fourier Transform (FFT) acquired upon *in situ* annealing of core-shell configurations of VO₂ nanocrystals with an amorphous HfO₂ shell. The initially amorphous HfO₂ domains are transformed into cubic HfO₂ at ca. 560 °C, and such domains persist upon heating up to 700 °C. Cubic HfO₂ and rhombohedral V₂O₃ domains are discernible upon annealing to 560 °C. Figure 6.5 shows that the crystallite size of cubic-HfO₂ is 8.4 ± 1.4 nm.

The crystallization and reduction of VO₂ to V₂O₃ occurs in concert and involves oxygen diffusion along a gradient of electropositivity. As noted above, oxygen vacancies are strongly destabilized as a result of crystallization. Thus, oxygen atoms diffuse from the vanadium oxide core to incipient crystalline HfO₂ domains resulting in a decrease in the formal valence of vanadium within the core.^{208,209} Previous studies with an identical reaction performed without the presence of VO₂ illustrates that initially nucleated cubic/tetragonal domains are lost, and the thermodynamically stable monoclinic phase of HfO₂ is stabilized as a result of grain growth.^{3,4,211–213} The epitaxial relationship between V₂O₃ and cubic HfO₂ in the crystalline core-shell structures is, therefore, critical to preventing reversion to the thermodynamically stable monoclinic polymorph at elevated temperatures.

HfO₂ exhibits high stability in aqueous media across a wide pH range; in contrast, V₂O₃ is readily dissolved in acidic media.⁶⁰ This difference in reactivity provides a means of isolating freestanding cubic HfO₂ powders. The V₂O₃ cores of V₂O₃@HfO₂ core-shell structures have been etched in acid solution at room temperature, thereby preserving the

metastable cubic structure of the shell. Figure 6.6 shows a lattice-resolved STEM image of freestanding cubic HfO₂ particles (prepared by acid etching of core-shell V₂O₃@HfO₂) acquired along the [110] zone axis. Based on analysis of the lattice-resolved TEM images, the recovered materials are phase pure. The vanadium incorporation alone cannot account for stabilization of the metastable cubic polymorph; previous studies have indicated the need for at least 11 at% V dopant incorporation to stabilize cubic HfO₂, which is observed to further be contaminated by HfV₂O₇.^{210,214} The stabilization of cubic HfO₂ stems from both kinetic origins as well as from the conditions of constrained equilibrium imposed by the small crystallite size.^{183,185,186}

Recent work has illustrated that a metastable polymorph can be preferentially stabilized if the barrier to nucleation of a metastable polymorph is lower than that of the thermodynamic phase.^{60,214} The rhombohedral V₂O₃ core essentially selects for the preferential formation of cubic HfO₂ as compared to other HfO₂ polymorphs owing to the available epitaxial relationship (as well as the influence of vanadium incorporation). In other words, the coherent low-energy interface accessible between cubic-HfO₂ and rhombohedral V₂O₃ (but not with monoclinic HfO₂) facilitates selective crystallization of the former polymorph by depressing the nucleation barrier. Interestingly, while the epitaxial relationship likely underpins nucleation of cubic HfO₂, the lattice mismatch is sufficiently large such as to bring about strain-induced delamination of the V₂O₃ core from the HfO₂ shell and this mismatch is further evidenced in the small crystallite size of the stabilized domains (Figures 6.2B and 6.3). Indeed, the crystallite size of cubic-HfO₂ is 8.4±1.4 nm, which suggests that extended coherent interfaces are not stabilized within this system.

The stabilization of freestanding cubic hafnia thereby provides access to a metastable kinetically trapped polymorph that is otherwise only accessible at temperatures above 2600 °C. The cubic HfO₂ remains stable for over 12 months without transforming to metastable tetragonal or thermodynamically stable monoclinic polymorphs.

6.3 Conclusions

In summary, we have demonstrated a detailed structural analysis of a facile low-temperature synthesis for stabilizing the metastable cubic phase of HfO₂ and unveiled the epitaxial relationship between rhombohedral V₂O₃ (generated *in situ* from the reduction of VO₂ as a result of oxygen diffusion) and cubic HfO₂.^{215,216} Oxygen diffusion proceeds from the VO₂ core to the amorphous HfO₂ shell owing to the more electropositive nature of the latter and the higher oxygen vacancy formation energy in crystalline HfO₂ as compared to amorphous HfO₂; the available epitaxial relationship along with the incorporation of vanadium atoms reduces the barrier to nucleation of the cubic polymorph notwithstanding its metastable nature and allows for its preservation at elevated temperatures wherein sintering and grain growth strongly favors stabilization of the monoclinic phase.^{217,218} The arrangement of VO₂ and HfO₂ in a core-shell structure further provides a direct solid-state synthetic route to cubic HfV₂O₇, a technologically significant negative thermal expansion material.^{202,203,219}

REFERENCES

- (1) Petkov, N. In Situ Real-Time TEM Reveals Growth, Transformation and Function in One-Dimensional Nanoscale Materials: From a Nanotechnology Perspective <https://www.hindawi.com/journals/isrn/2013/893060/> (accessed May 23, 2019). <https://doi.org/10.1155/2013/893060>.
- (2) Hunyadi Murph, S. E. An Introduction to Nanotechnology. In *Anisotropic and Shape-Selective Nanomaterials: Structure-Property Relationships*; Hunyadi Murph, S. E., Larsen, G. K., Coopersmith, K. J., Eds.; Nanostructure Science and Technology; Springer International Publishing: Cham, **2017**; pp 3–5. https://doi.org/10.1007/978-3-319-59662-4_1.
- (3) R. Waetzig, G.; W. Depner, S.; Asayesh-Ardakani, H.; D. Cultrara, N.; Shahbazian-Yassar, R.; Banerjee, S. Stabilizing Metastable Tetragonal HfO₂ Using a Non-Hydrolytic Solution-Phase Route: Ligand Exchange as a Means of Controlling Particle Size. *Chemical Science* **2016**, *7* (8), 4930–4939. <https://doi.org/10.1039/C6SC01601D>.
- (4) Hudak, B.; Depner, S.; Waetzig, G.; Talapatra, A.; Arróyave, R.; Banerjee, S.; Guiton, B. Real-Time Atomistic Observation of Structural Phase Transformations in Individual Hafnia Nanorods. *Nature Communications* **2017**, *8*. <https://doi.org/10.1038/ncomms15316>.
- (5) Chen, L.; Liu, J.; Jiang, C.; Zhao, K.; Chen, H.; Shi, X.; Chen, L.; Sun, C.; Zhang, S.; Wang, Y.; Zhang, Z. Nanoscale Behavior and Manipulation of the Phase Transition in Single-Crystal Cu₂Se. *Advanced Materials* **2019**, *31* (4), 1804919. <https://doi.org/10.1002/adma.201804919>.
- (6) West, A. R. *Solid State Chemistry and Its Applications*; Wiley, 2014.
- (7) Wang, Z. W.; Li, Z. Y.; Park, S. J.; Abdela, A.; Tang, D.; Palmer, R. E. Quantitative Z-Contrast Imaging in the Scanning Transmission Electron Microscope with Size-Selected Clusters. *Phys. Rev. B* **2011**, *84* (7), 073408. <https://doi.org/10.1103/PhysRevB.84.073408>.
- (8) Pennycook, S. J.; Rafferty, B.; Nellist, P. D. Z-Contrast Imaging in an Aberration-Corrected Scanning Transmission Electron Microscope. *Microscopy and Microanalysis* **2000**, 343–352.
- (9) Yu, L.; Hudak, B. M.; Ullah, A.; Thomas, M. P.; Porter, C. C.; Thisera, A.; Pham, R. H.; De Alwis Goonatilleke, M.; Guiton, B. S. Unveiling the Microscopic Origins of Phase Transformations: An *in Situ* TEM Perspective. *Chemistry of Materials* **2020**, *32* (2), 639–650. <https://doi.org/10.1021/acs.chemmater.9b03360>.
- (10) Sinclair, R. In Situ High-Resolution Transmission Electron Microscopy of Material Reactions. *MRS Bulletin* **2013**, *38* (12), 1065–1071. <http://dx.doi.org.ezproxy.uky.edu/10.1557/mrs.2013.285>.
- (11) Pienack, N.; Bensch, W. In-Situ Monitoring of the Formation of Crystalline Solids. *Angewandte Chemie International Edition* **2011**, *50* (9), 2014–2034. <https://doi.org/10.1002/anie.201001180>.
- (12) Ross, F. M. Growth Processes and Phase Transformations Studied in Situ Transmission Electron Microscopy. *IBM Journal of Research and Development* **2000**, *44* (4), 489–501. <https://doi.org/10.1147/rd.444.0489>.

- (13) Gao, M.-R.; Xu, Y.-F.; Jiang, J.; Yu, S.-H. Nanostructured Metal Chalcogenides: Synthesis, Modification, and Applications in Energy Conversion and Storage Devices. *Chem. Soc. Rev.* **2013**, *42* (7), 2986–3017. <https://doi.org/10.1039/C2CS35310E>.
- (14) Antunez, P. D.; Buckley, J. J.; Brutchey, R. L. Tin and Germanium Monochalcogenide IV-VI Semiconductor Nanocrystals for Use in Solar Cells. *Nanoscale* **2011**, *3* (6), 2399–2411. <https://doi.org/10.1039/c1nr10084j>.
- (15) Li, G.; Zhang, B.; Rao, J.; Herranz Gonzalez, D.; Blake, G. R.; de Groot, R. A.; Palstra, T. T. M. Effect of Vacancies on Magnetism, Electrical Transport, and Thermoelectric Performance of Marcasite FeSe_{2-δ} (δ = 0.05). *Chem. Mater.* **2015**, *27* (24), 8220–8229. <https://doi.org/10.1021/acs.chemmater.5b03562>.
- (16) Burda, C.; Chen, X.; Narayanan, R.; El-Sayed, M. A. Chemistry and Properties of Nanocrystals of Different Shapes. *Chem. Rev.* **2005**, *105* (4), 1025–1102. <https://doi.org/10.1021/cr030063a>.
- (17) Bastola, E.; Bhandari, K. P.; Matthews, A. J.; Shrestha, N.; Ellingson, R. J. Elemental Anion Thermal Injection Synthesis of Nanocrystalline Marcasite Iron Dichalcogenide FeSe₂ and FeTe₂. *RSC Adv.* **2016**, *6* (74), 69708–69714. <https://doi.org/10.1039/C6RA06351A>.
- (18) Byrappa, K.; Adschiri, T. Hydrothermal Technology for Nanotechnology. *Progress in Crystal Growth and Characterization of Materials* **2007**, *53* (2), 117–166. <https://doi.org/10.1016/j.pcrysgrow.2007.04.001>.
- (19) Phan, C. M.; Nguyen, H. M. Role of Capping Agent in Wet Synthesis of Nanoparticles. *J. Phys. Chem. A* **2017**, *121* (17), 3213–3219. <https://doi.org/10.1021/acs.jpca.7b02186>.
- (20) Bakshi, M. S. Nanoshape Control Tendency of Phospholipids and Proteins: Protein–Nanoparticle Composites, Seeding, Self-Aggregation, and Their Applications in Bionanotechnology and Nanotoxicology. *J. Phys. Chem. C* **2011**, *115* (29), 13947–13960. <https://doi.org/10.1021/jp202454k>.
- (21) Byrappa, K.; Yoshimura, M. 1 - Hydrothermal Technology—Principles and Applications. In *Handbook of Hydrothermal Technology*; William Andrew Publishing: Norwich, NY, 2001; pp 1–52. <https://doi.org/10.1016/B978-081551445-9.50002-7>.
- (22) Li, J.; Wu, Q.; Wu, J. Synthesis of Nanoparticles via Solvothermal and Hydrothermal Methods. In *Handbook of Nanoparticles*; 2016; pp 295–328. https://doi.org/10.1007/978-3-319-15338-4_17.
- (23) Darr, J. A.; Zhang, J.; Makwana, N. M.; Weng, X. Continuous Hydrothermal Synthesis of Inorganic Nanoparticles: Applications and Future Directions. *Chem. Rev.* **2017**, *117* (17), 11125–11238. <https://doi.org/10.1021/acs.chemrev.6b00417>.
- (24) Zhang, X.; Che, G.; Fan, W.; Shi, W. Controlled Hydrothermal Synthesis of Three-Dimensional FeSe₂ Rod Clusters. *IET Micro Nano Letters* **2012**, *7* (10), 1076–1079. <https://doi.org/10.1049/mnl.2012.0669>.
- (25) Williams, D. B.; Carter, C. B. The Transmission Electron Microscope. In *Transmission Electron Microscopy*; Springer, Boston, MA, 1996; pp 3–17. https://doi.org/10.1007/978-1-4757-2519-3_1.
- (26) Williams, D. B.; Carter, C. B. Amplitude Contrast. In *Transmission Electron Microscopy: A Textbook for Materials Science*; Williams, D. B., Carter, C. B., Eds.;

- Springer US: Boston, MA, 2009; pp 371–388. https://doi.org/10.1007/978-0-387-76501-3_22.
- (27) High-Resolution STEM Imaging. In *Transmission Electron Microscopy and Diffractometry of Materials*; Fultz, B., Howe, J. M., Eds.; Springer: Berlin, Heidelberg, 2008; pp 583–609. https://doi.org/10.1007/978-3-540-73886-2_11.
- (28) Pennycook, S. J. *Structure Determination Through Z-Contrast Microscopy Abstract*.
- (29) Pennycook, S. J.; Jesson, D. E. High-Resolution Z-Contrast Imaging of Crystals. *Ultramicroscopy* **1991**, *37* (1), 14–38. [https://doi.org/10.1016/0304-3991\(91\)90004-P](https://doi.org/10.1016/0304-3991(91)90004-P).
- (30) Pennycook, S. J.; Jesson, D. E. Atomic Resolution Z-Contrast Imaging of Interfaces. *Acta Metallurgica et Materialia* **1992**, *40*, S149–S159. [https://doi.org/10.1016/0956-7151\(92\)90275-J](https://doi.org/10.1016/0956-7151(92)90275-J).
- (31) Batson, P. E.; Dellby, N.; Krivanek, O. L. Sub-Ångstrom Resolution Using Aberration Corrected Electron Optics. *Nature* **2002**, *418* (6898), 617–620. <https://doi.org/10.1038/nature00972>.
- (32) Williams, D. B.; Carter, C. B. Lenses, Apertures, and Resolution. In *Transmission Electron Microscopy: A Textbook for Materials Science*; Williams, D. B., Carter, C. B., Eds.; Springer US: Boston, MA, 2009; pp 91–114. https://doi.org/10.1007/978-0-387-76501-3_6.
- (33) Brydson, R.; Brydson, R. *Aberration-Corrected Analytical Transmission Electron Microscopy*; John Wiley & Sons, Incorporated: Hoboken, UNITED KINGDOM, 2011.
- (34) MacLaren, I.; Ramasse, Q. M. Aberration-Corrected Scanning Transmission Electron Microscopy for Atomic-Resolution Studies of Functional Oxides. *International Materials Reviews* **2014**, *59* (3), 115–131. <https://doi.org/10.1179/1743280413Y.0000000026>.
- (35) Krivanek, O. L.; Corbin, G. J.; Dellby, N.; Elston, B. F.; Keyse, R. J.; Murfitt, M. F.; Own, C. S.; Szilagy, Z. S.; Woodruff, J. W. An Electron Microscope for the Aberration-Corrected Era. *Ultramicroscopy* **2008**, *108* (3), 179–195. <https://doi.org/10.1016/j.ultramic.2007.07.010>.
- (36) Krivanek, O. L.; Dellby, N.; Lupini, A. R. Towards Sub-Å Electron Beams. *Ultramicroscopy* **1999**, *78* (1), 1–11. [https://doi.org/10.1016/S0304-3991\(99\)00013-3](https://doi.org/10.1016/S0304-3991(99)00013-3).
- (37) Bleloch, A.; Lupini, A. Imaging at the Picoscale. *Materials Today* **2004**, *7* (12), 42–48. [https://doi.org/10.1016/S1369-7021\(04\)00570-X](https://doi.org/10.1016/S1369-7021(04)00570-X).
- (38) Pennycook, S. J.; Lupini, A. R.; Kadavanich, A.; McBride, J. R.; Rosenthal, S. J.; Puetter, R. C.; Yahil, A.; Krivanek, O. L.; Dellby, N.; Nellist, P. D. L.; Duscher, G.; Wang, L. G.; Pantelides, S. T. Aberration-Corrected Scanning Transmission Electron Microscopy: The Potential for Nano- and Interface Science: Dedicated to Professor Dr. Dr. h. c. Manfred Rühle on the Occasion of His 65th Birthday. *Zeitschrift für Metallkunde* **2003**, *94* (4), 350–357. <https://doi.org/10.3139/146.030350>.
- (39) Tanaka, N. Introduction to Fourier Transforms for TEM and STEM. In *Electron Nano-Imaging: Basics of Imaging and Diffraction for TEM and STEM*; Tanaka, N., Ed.; Springer Japan: Tokyo, 2017; pp 219–226. https://doi.org/10.1007/978-4-431-56502-4_15.

- (40) Williams, D. B.; Carter, C. B. Processing and Quantifying Images. In *Transmission Electron Microscopy: A Textbook for Materials Science*; Williams, D. B., Carter, C. B., Eds.; Springer US: Boston, MA, 2009; pp 549–578. https://doi.org/10.1007/978-0-387-76501-3_31.
- (41) Kim, Y.-M.; Jeong, J.-M.; Kim, J.-G.; Kim, Y.-J. Image Processing of Atomic Resolution Transmission Electron Microscope Images. *Image Processing* **2005**, 164–169.
- (42) Thomas, M. P.; Wanninayake, N.; Goonatilleke, M. D. A.; Kim, D. Y.; Guiton, B. S. Direct Imaging of Heteroatom Dopants in Catalytic Carbon Nano-Onions. *Nanoscale* **2020**, 12 (10), 6144–6152. <https://doi.org/10.1039/D0NR00335B>.
- (43) Williams, D. B.; Carter, C. B. X-Ray Spectrometry. In *Transmission Electron Microscopy: A Textbook for Materials Science*; Williams, D. B., Carter, C. B., Eds.; Springer US: Boston, MA, 2009; pp 581–603. https://doi.org/10.1007/978-0-387-76501-3_32.
- (44) Egerton, R. F. Electron Energy-Loss Spectroscopy in the TEM. *Rep. Prog. Phys.* **2008**, 72 (1), 016502. <https://doi.org/10.1088/0034-4885/72/1/016502>.
- (45) Egerton, R. F. An Introduction to EELS. In *Electron Energy-Loss Spectroscopy in the Electron Microscope*; Egerton, R. F., Ed.; Springer US: Boston, MA, 2011; pp 1–28. https://doi.org/10.1007/978-1-4419-9583-4_1.
- (46) Williams, D. B.; Carter, C. B. Elastic Scattering. In *Transmission Electron Microscopy: A Textbook for Materials Science*; Williams, D. B., Carter, C. B., Eds.; Springer US: Boston, MA, 2009; pp 39–51. https://doi.org/10.1007/978-0-387-76501-3_3.
- (47) Williams, D. B.; Carter, C. B. Inelastic Scattering and Beam Damage. In *Transmission Electron Microscopy: A Textbook for Materials Science*; Williams, D. B., Carter, C. B., Eds.; Springer US: Boston, MA, 2009; pp 53–71. https://doi.org/10.1007/978-0-387-76501-3_4.
- (48) Williams, D. B.; Carter, C. B. Electron Energy-Loss Spectrometers and Filters. In *Transmission Electron Microscopy: A Textbook for Materials Science*; Williams, D. B., Carter, C. B., Eds.; Springer US: Boston, MA, 2009; pp 679–698. https://doi.org/10.1007/978-0-387-76501-3_37.
- (49) Williams, D. B.; Carter, C. B. High Energy-Loss Spectra and Images. In *Transmission Electron Microscopy: A Textbook for Materials Science*; Williams, D. B., Carter, C. B., Eds.; Springer US: Boston, MA, 2009; pp 715–739. https://doi.org/10.1007/978-0-387-76501-3_39.
- (50) Williams, D. B.; Carter, C. B. Low-Loss and No-Loss Spectra and Images. In *Transmission Electron Microscopy: A Textbook for Materials Science*; Williams, D. B., Carter, C. B., Eds.; Springer US: Boston, MA, 2009; pp 699–713. https://doi.org/10.1007/978-0-387-76501-3_38.
- (51) Casu, A.; Sogne, E.; Genovese, A.; DiBenedetto, C.; Mozo, S. L.; Zuddas, E.; Falqui, F. P. and A. The New Youth of the *In Situ* Transmission Electron Microscopy. **2016**. <https://doi.org/10.5772/63269>.
- (52) Ramachandramoorthy, R.; Bernal, R.; Espinosa, H. D. Pushing the Envelope of *In Situ* Transmission Electron Microscopy. *ACS Nano* **2015**, 9 (5), 4675–4685. <https://doi.org/10.1021/acsnano.5b01391>.

- (53) Taheri, M. L.; Stach, E. A.; Arslan, I.; Crozier, P. A.; Kabius, B. C.; LaGrange, T.; Minor, A. M.; Takeda, S.; Tanase, M.; Wagner, J. B.; Sharma, R. Current Status and Future Directions for in Situ Transmission Electron Microscopy. *Ultramicroscopy* **2016**, *170* (Supplement C), 86–95. <https://doi.org/10.1016/j.ultramic.2016.08.007>.
- (54) McDowell, M. T.; Jungjohann, K. L.; Celano, U. Dynamic Nanomaterials Phenomena Investigated with in Situ Transmission Electron Microscopy: A Nano Letters Virtual Issue. *Nano Lett.* **2018**, *18* (2), 657–659. <https://doi.org/10.1021/acs.nanolett.8b00266>.
- (55) Navrotsky, A. Nanoscale Effects on Thermodynamics and Phase Equilibria in Oxide Systems. 10.
- (56) Kamino, T.; Saka, H. A Newly Developed High Resolution Hot Stage and Its Application to Materials Characterization. *Microscopy Microanalysis Microstructures* **1993**, *4* (2–3), 127–135. <https://doi.org/10.1051/mmm:0199300402-3012700>.
- (57) Kamino, T.; Yaguchi, T.; Sato, T.; Hashimoto, T. Development of a Technique for High Resolution Electron Microscopic Observation of Nano-Materials at Elevated Temperatures. *J Electron Microsc (Tokyo)* **2005**, *54* (6), 505–508. <https://doi.org/10.1093/jmicro/dfi072>.
- (58) Allard, L. F.; Bigelow, W. C.; Jose-Yacamán, M.; Nackashi, D. P.; Damiano, J.; Mick, S. E. A New MEMS-Based System for Ultra-High-Resolution Imaging at Elevated Temperatures. *Microscopy Research and Technique* **2009**, *72* (3), 208–215. <https://doi.org/10.1002/jemt.20673>.
- (59) Advanced TEM Solutions for In Situ Microscopy Characterization <https://www.protochips.com/> (accessed Apr 27, 2020).
- (60) Rai, D.; Kitamura, A.; Rosso, K. M.; Sasaki, T.; Kobayashi, T. Issues Concerning the Determination of Solubility Products of Sparingly Soluble Crystalline Solids: Solubility of HfO₂(Cr). *Radiochimica Acta* **2016**, *104* (8), 583–592. <https://doi.org/10.1515/ract-2015-2540>.
- (61) Post, K.; Robins, R. G. Thermodynamic Diagrams for the Vanadium-Water System at 298·15K. *Electrochimica Acta* **1976**, *21* (6), 401–405. [https://doi.org/10.1016/0013-4686\(76\)85115-8](https://doi.org/10.1016/0013-4686(76)85115-8).
- (62) Chauhan, A.; Chauhan, P. Powder XRD Technique and Its Applications in Science and Technology. *Journal of Analytical & Bioanalytical Techniques* **2014**, 1–5. <https://doi.org/10.4172/2155-9872.1000212>.
- (63) Reichelt, R. Scanning Electron Microscopy. In *Science of Microscopy*; Springer, New York, NY, 2007; pp 133–272. https://doi.org/10.1007/978-0-387-49762-4_3.
- (64) Williams, D. B.; Carter, C. B. The Instrument. In *Transmission Electron Microscopy: A Textbook for Materials Science*; Williams, D. B., Carter, C. B., Eds.; Springer US: Boston, MA, 2009; pp 141–171. https://doi.org/10.1007/978-0-387-76501-3_9.
- (65) Williams, D. B.; Carter, C. B. Diffraction in TEM. In *Transmission Electron Microscopy: A Textbook for Materials Science*; Williams, D. B., Carter, C. B., Eds.; Springer US: Boston, MA, 2009; pp 197–209. https://doi.org/10.1007/978-0-387-76501-3_11.

- (66) Zaefferer, S. New Developments of Computer-Aided Crystallographic Analysis in Transmission Electron Microscopy. *J Appl Cryst* **2000**, *33* (1), 10–25. <https://doi.org/10.1107/S0021889899010894>.
- (67) Williams, D. B.; Carter, C. B. Thinking in Reciprocal Space. In *Transmission Electron Microscopy: A Textbook for Materials Science*; Williams, D. B., Carter, C. B., Eds.; Springer US: Boston, MA, 2009; pp 211–219. https://doi.org/10.1007/978-0-387-76501-3_12.
- (68) McCusker, L. B.; Baerlocher, C. Using Electron Microscopy to Complement X-Ray Powder Diffraction Data to Solve Complex Crystal Structures. *Chem. Commun.* **2009**, No. 12, 1439–1451. <https://doi.org/10.1039/B821716E>.
- (69) Electron Diffraction and Crystallography. In *Transmission Electron Microscopy and Diffractometry of Materials*; Fultz, B., Howe, J. M., Eds.; Springer: Berlin, Heidelberg, 2008; pp 273–336. https://doi.org/10.1007/978-3-540-73886-2_6.
- (70) DoITPoMS - TLP Library Indexing Electron Diffraction Patterns <https://www.doitpoms.ac.uk/tlplib/diffraction-patterns/printall.php> (accessed May 18, 2020).
- (71) Zhou, W.; Greer, H. F. What Can Electron Microscopy Tell Us Beyond Crystal Structures? *European Journal of Inorganic Chemistry* **2016**, *2016* (7), 941–950. <https://doi.org/10.1002/ejic.201501342>.
- (72) Diffraction from Crystals. In *Transmission Electron Microscopy and Diffractometry of Materials*; Fultz, B., Howe, J. M., Eds.; Springer: Berlin, Heidelberg, 2008; pp 223–272. https://doi.org/10.1007/978-3-540-73886-2_5.
- (73) Wagner, J. M. *X-Ray Photoelectron Spectroscopy*; Nova Science Publishers, Incorporated: Hauppauge, UNITED STATES, 2010.
- (74) Zhou, X.; Rodriguez, E. E. Tetrahedral Transition Metal Chalcogenides as Functional Inorganic Materials. *Chem. Mater.* **2017**, *29* (14), 5737–5752. <https://doi.org/10.1021/acs.chemmater.7b01561>.
- (75) Hsu, F.-C.; Luo, J.-Y.; Yeh, K.-W.; Chen, T.-K.; Huang, T.-W.; Wu, P. M.; Lee, Y.-C.; Huang, Y.-L.; Chu, Y.-Y.; Yan, D.-C.; Wu, M.-K. Superconductivity in the PbO-Type Structure α -FeSe. *PNAS* **2008**, *105* (38), 14262–14264. <https://doi.org/10.1073/pnas.0807325105>.
- (76) Sines, I. T.; Vaughn II, D. D.; Misra, R.; Popczun, E. J.; Schaak, R. E. Synthesis of Tetragonal Mackinawite-Type FeS Nanosheets by Solvothermal Crystallization. *Journal of Solid State Chemistry* **2012**, *196* (Supplement C), 17–20. <https://doi.org/10.1016/j.jssc.2012.07.056>.
- (77) Kuhn, S. J.; Kidder, M. K.; Parker, D. S.; dela Cruz, C.; McGuire, M. A.; Chance, W. M.; Li, L.; Debeer-Schmitt, L.; Ermentrout, J.; Littrell, K. C.; Eskildsen, M. R.; Sefat, A. S. Structure and Property Correlations in FeS. *Physica C: Superconductivity and its Applications* **2017**, *534*, 29–36. <https://doi.org/10.1016/j.physc.2016.12.006>.
- (78) McQueen, T. M.; Williams, A. J.; Stephens, P. W.; Tao, J.; Zhu, Y.; Ksenofontov, V.; Casper, F.; Felser, C.; Cava, R. J. Tetragonal-to-Orthorhombic Structural Phase Transition at 90 K in the Superconductor Fe_{1.01}Se. *Phys. Rev. Lett.* **2009**, *103* (5), 057002. <https://doi.org/10.1103/PhysRevLett.103.057002>.

- (79) Bertaut, E. F.; Burlet, P.; Chappert, J. Sur l'absence d'ordre Magnétique Dans La Forme Quadratique de FeS. *Solid State Communications* **1965**, *3* (10), 335–338. [https://doi.org/10.1016/0038-1098\(65\)90090-6](https://doi.org/10.1016/0038-1098(65)90090-6).
- (80) Denholme, S. J.; Demura, S.; Okazaki, H.; Hara, H.; Deguchi, K.; Fujioka, M.; Ozaki, T.; Yamaguchi, T.; Takeya, H.; Takano, Y. Evidence for Non-Metallic Behaviour in Tetragonal FeS (Mackinawite). *Materials Chemistry and Physics* **2014**, *147* (1), 50–56. <https://doi.org/10.1016/j.matchemphys.2014.04.005>.
- (81) Lai, X.; Zhang, H.; Wang, Y.; Wang, X.; Zhang, X.; Lin, J.; Huang, F. Observation of Superconductivity in Tetragonal FeS. *J. Am. Chem. Soc.* **2015**, *137* (32), 10148–10151. <https://doi.org/10.1021/jacs.5b06687>.
- (82) Shu-Lin, Z.; Hui-Xian, W.; Cheng, D. Synthesis and Electrical Conductivity of Nanocrystalline Tetragonal FeS. *Chinese Phys. B* **2014**, *23* (8), 087203. <https://doi.org/10.1088/1674-1056/23/8/087203>.
- (83) Lin, H.; Li, Y.; Deng, Q.; Xing, J.; Liu, J.; Zhu, X.; Yang, H.; Wen, H.-H. Multiband Superconductivity and Large Anisotropy in FeS Crystals. *Phys. Rev. B* **2016**, *93* (14), 144505. <https://doi.org/10.1103/PhysRevB.93.144505>.
- (84) Borg, C. K. H.; Zhou, X.; Eckberg, C.; Campbell, D. J.; Saha, S. R.; Paglione, J.; Rodriguez, E. E. Strong Anisotropy in Nearly Ideal Tetrahedral Superconducting FeS Single Crystals. *Phys. Rev. B* **2016**, *93* (9), 094522. <https://doi.org/10.1103/PhysRevB.93.094522>.
- (85) Zhang, X.; Lai, X.; Yi, N.; He, J.; Chen, H.; Zhang, H.; Lin, J.; Huang, F. Synthesis, Crystal Structure and Physical Properties of [Li_{0.85}Fe_{0.15}OH][FeS]. *RSC Advances* **2015**, *5* (48), 38248–38253. <https://doi.org/10.1039/C5RA04037J>.
- (86) Pachmayr, U.; Fehn, N.; Johrendt, D. Structural Transition and Superconductivity in Hydrothermally Synthesized FeX (X = S, Se). *Chemical Communications* **2016**, *52* (1), 194–197. <https://doi.org/10.1039/C5CC07739G>.
- (87) Zhou, X.; Eckberg, C.; Wilfong, B.; Liou, S.-C.; K. Vivanco, H.; Paglione, J.; E. Rodriguez, E. Superconductivity and Magnetism in Iron Sulfides Intercalated by Metal Hydroxides. *Chem. Sci.* **2017**, *8* (5), 3781–3788. <https://doi.org/10.1039/C6SC05268A>.
- (88) Magomedov, M. On the Superconducting Transition Temperature for Metallic Nanocrystals. *Physics of the Solid State* **2003**, *45*, 1213–1218. <https://doi.org/10.1134/1.1594232>.
- (89) Rickard, D.; Luther, G. W. Chemistry of Iron Sulfides. *Chem. Rev.* **2007**, *107* (2), 514–562. <https://doi.org/10.1021/cr0503658>.
- (90) Jeong, H. Y.; Lee, J. H.; Hayes, K. F. Characterization of Synthetic Nanocrystalline Mackinawite: Crystal Structure, Particle Size, and Specific Surface Area. *Geochimica et Cosmochimica Acta* **2008**, *72* (2), 493–505. <https://doi.org/10.1016/j.gca.2007.11.008>.
- (91) Kwon, K. D.; Refson, K.; Bone, S.; Qiao, R.; Yang, W.; Liu, Z.; Sposito, G. Magnetic Ordering in Tetragonal FeS: Evidence for Strong Itinerant Spin Fluctuations. *Phys. Rev. B* **2011**, *83* (6), 064402. <https://doi.org/10.1103/PhysRevB.83.064402>.
- (92) Welz, D.; Rosenburg, M. Electronic Band Structure of Tetrahedral Iron Sulphides. *J. Phys. C: Solid State Phys.* **1987**, *20* (25), 3911. <https://doi.org/10.1088/0022-3719/20/25/018>.

- (93) Yang, X.; Du, Z.; Du, G.; Gu, Q.; Lin, H.; Fang, D.; Yang, H.; Zhu, X.; Wen, H.-H. Strong Coupling Superconductivity Revealed by Scanning Tunneling Microscope in Tetragonal FeS. *Physical Review B* **2016**, *94* (2). <https://doi.org/10.1103/PhysRevB.94.024521>.
- (94) Bai, P.; Zheng, S.; Chen, C.; Zhao, H. Investigation of the Iron–Sulfide Phase Transformation in Nanoscale. *Crystal Growth & Design* **2014**, *14* (9), 4295–4302. <https://doi.org/10.1021/cg500333p>.
- (95) Csákberényi-Malasics, D.; Rodriguez-Blanco, J. D.; Kis, V. K.; Rečnik, A.; Benning, L. G.; Pósfai, M. Structural Properties and Transformations of Precipitated FeS. *Chemical Geology* **2012**, *294–295*, 249–258. <https://doi.org/10.1016/j.chemgeo.2011.12.009>.
- (96) Boursiquot, S.; Mullet, M.; Abdelmoula, M.; Génin, J.-M.; Ehrhardt, J.-J. The Dry Oxidation of Tetragonal FeS_{1-x}mackinawite. *Phys Chem Min* **2001**, *28* (9), 600–611. <https://doi.org/10.1007/s002690100193>.
- (97) Shoesmith, D. W.; Taylor, P.; Bailey, M. G.; Owen, D. G. The Formation of Ferrous Monosulfide Polymorphs during the Corrosion of Iron by Aqueous Hydrogen Sulfide at 21°C. *J. Electrochem. Soc.* **1980**, *127* (5), 1007–1015. <https://doi.org/10.1149/1.2129808>.
- (98) Shoesmith, D. W.; Bailey, M. G.; Ikeda, B. Electrochemical Formation of Mackinawite in Alkaline Sulphide Solutions. *Electrochimica Acta* **1978**, *23* (12), 1329–1339. [https://doi.org/10.1016/0013-4686\(78\)80013-9](https://doi.org/10.1016/0013-4686(78)80013-9).
- (99) Wadia, C.; Wu, Y.; Gul, S.; Volkman, S. K.; Guo, J.; Alivisatos, A. P. Surfactant-Assisted Hydrothermal Synthesis of Single Phase Pyrite FeS₂ Nanocrystals. *Chem. Mater.* **2009**, *21* (13), 2568–2570. <https://doi.org/10.1021/cm901273v>.
- (100) Mourdikoudis, S.; Liz-Marzán, L. Oleylamine in Nanoparticle Synthesis. *Chemistry of Materials* **2013**, *25*. <https://doi.org/10.1021/cm4000476>.
- (101) Puentes, V. F.; Krishnan, K. M.; Alivisatos, A. P. Colloidal Nanocrystal Shape and Size Control: The Case of Cobalt. *Science* **2001**, *291* (5511), 2115–2117. <https://doi.org/10.1126/science.1058495>.
- (102) Lingane, J. J. Polarographic Investigation of Oxalate, Citrate and Tartrate Complexes of Ferric and Ferrous Iron. *J. Am. Chem. Soc.* **1946**, *68* (12), 2448–2453. <https://doi.org/10.1021/ja01216a002>.
- (103) Yoreo, J. J. D.; Vekilov, P. G. Principles of Crystal Nucleation and Growth. *Reviews in Mineralogy and Geochemistry* **2003**, *54* (1), 57–93. <https://doi.org/10.2113/0540057>.
- (104) Cubillas, P.; Anderson, M. W. Synthesis Mechanism: Crystal Growth and Nucleation. In *Zeolites and Catalysis*; John Wiley & Sons, Ltd, 2010; pp 1–55. <https://doi.org/10.1002/9783527630295.ch1>.
- (105) Penkova, A.; Chayen, N. E.; Saridakis, E.; Nanev, C.; IUCr. Nucleation of protein crystals in a wide continuous supersaturation gradient <http://scripts.iucr.org/cgi-bin/paper?ic0006> (accessed Sep 29, 2019). <https://doi.org/10.1107/S0907444902014166>.
- (106) Niu, Z.; Li, Y. Removal and Utilization of Capping Agents in Nanocatalysis. *Chem. Mater.* **2014**, *26* (1), 72–83. <https://doi.org/10.1021/cm4022479>.

- (107) Roberts, D. M.; Landin, A. R.; Ritter, T. G.; Eaves, J. D.; Stoldt, C. R. Nanocrystalline Iron Monosulfides Near Stoichiometry. *Scientific Reports* **2018**, *8* (1). <https://doi.org/10.1038/s41598-018-24739-8>.
- (108) Mycroft, J. R.; Bancroft, G. M.; McIntyre, N. S.; Lorimer, J. W.; Hill, I. R. Detection of Sulphur and Polysulphides on Electrochemically Oxidized Pyrite Surfaces by X-Ray Photoelectron Spectroscopy and Raman Spectroscopy. *Journal of Electroanalytical Chemistry and Interfacial Electrochemistry* **1990**, *292* (1), 139–152. [https://doi.org/10.1016/0022-0728\(90\)87332-E](https://doi.org/10.1016/0022-0728(90)87332-E).
- (109) Pratt, A. R.; Muir, I. J.; Nesbitt, H. W. X-Ray Photoelectron and Auger Electron Spectroscopic Studies of Pyrrhotite and Mechanism of Air Oxidation. *Geochimica et Cosmochimica Acta* **1994**, *58* (2), 827–841. [https://doi.org/10.1016/0016-7037\(94\)90508-8](https://doi.org/10.1016/0016-7037(94)90508-8).
- (110) Pratt, A. R.; Nesbitt, H. W.; muir, I. J. Generation of Acids from Mine Waste: Oxidative Leaching of Pyrrhotite in Dilute H₂SO₄ Solutions at PH 3.0. *Geochimica et Cosmochimica Acta* **1994**, *58* (23), 5147–5159. [https://doi.org/10.1016/0016-7037\(94\)90300-X](https://doi.org/10.1016/0016-7037(94)90300-X).
- (111) Mullet, M.; Boursiquot, S.; Abdelmoula, M.; Génin, J.-M.; Ehrhardt, J.-J. Surface Chemistry and Structural Properties of Mackinawite Prepared by Reaction of Sulfide Ions with Metallic Iron. *Geochimica et Cosmochimica Acta* **2002**, *66* (5), 829–836. [https://doi.org/10.1016/S0016-7037\(01\)00805-5](https://doi.org/10.1016/S0016-7037(01)00805-5).
- (112) Thomas, J. E.; Jones, C. F.; Skinner, W. M.; Smart, R. St. C. The Role of Surface Sulfur Species in the Inhibition of Pyrrhotite Dissolution in Acid Conditions. *Geochimica et Cosmochimica Acta* **1998**, *62* (9), 1555–1565. [https://doi.org/10.1016/S0016-7037\(98\)00087-8](https://doi.org/10.1016/S0016-7037(98)00087-8).
- (113) Jones, C. F.; LeCount, S.; Smart, R. St. C.; White, T. J. Compositional and Structural Alteration of Pyrrhotite Surfaces in Solution: XPS and XRD Studies. *Applied Surface Science* **1992**, *55* (1), 65–85. [https://doi.org/10.1016/0169-4332\(92\)90382-8](https://doi.org/10.1016/0169-4332(92)90382-8).
- (114) McIntyre, N. S.; Zetaruk, D. G. X-Ray Photoelectron Spectroscopic Studies of Iron Oxides. *Anal. Chem.* **1977**, *49* (11), 1521–1529. <https://doi.org/10.1021/ac50019a016>.
- (115) Pratt, A. R.; Nesbitt, H. W.; Mycroft, J. R. The Increased Reactivity of Pyrrhotite and Magnetite Phases in Sulphide Mine Tailings. *Journal of Geochemical Exploration* **1996**, *56* (1), 1–11. [https://doi.org/10.1016/0375-6742\(96\)00008-8](https://doi.org/10.1016/0375-6742(96)00008-8).
- (116) Han, C.; Bo, X.; Zhang, Y.; Li, M.; Guo, L. One-Pot Synthesis of Nitrogen and Sulfur Co-Doped Onion-like Mesoporous Carbon Vesicle as an Efficient Metal-Free Catalyst for Oxygen Reduction Reaction in Alkaline Solution. *Journal of Power Sources* **2014**, *272*, 267–276. <https://doi.org/10.1016/j.jpowsour.2014.08.104>.
- (117) Mykhailiv, O.; Brzezinski, K.; Sulikowski, B.; Olejniczak, Z.; Gras, M.; Lota, G.; Molina-Ontoria, A.; Jakubczyk, M.; Echegoyen, L.; Plonska-Brzezinska, M. E. Boron-Doped Polygonal Carbon Nano-Onions: Synthesis and Applications in Electrochemical Energy Storage. *Chemistry – A European Journal* **2017**, *23* (29), 7132–7141. <https://doi.org/10.1002/chem.201700914>.
- (118) Paraknowitsch, J. P.; Thomas, A. Doping Carbons beyond Nitrogen: An Overview of Advanced Heteroatom Doped Carbons with Boron, Sulphur and Phosphorus for

- Energy Applications. *Energy Environ. Sci.* **2013**, *6* (10), 2839–2855. <https://doi.org/10.1039/C3EE41444B>.
- (119) Choi, E. Y.; Kim, C. K. Fabrication of Nitrogen-Doped Nano-Onions and Their Electrocatalytic Activity toward the Oxygen Reduction Reaction. *Scientific Reports* **2017**, *7* (1), 4178. <https://doi.org/10.1038/s41598-017-04597-6>.
- (120) Yang, L.; Jiang, S.; Zhao, Y.; Zhu, L.; Chen, S.; Wang, X.; Wu, Q.; Ma, J.; Ma, Y.; Hu, Z. Boron-Doped Carbon Nanotubes as Metal-Free Electrocatalysts for the Oxygen Reduction Reaction. *Angewandte Chemie International Edition* **2011**, *50* (31), 7132–7135. <https://doi.org/10.1002/anie.201101287>.
- (121) Lin, Y.-C.; Teng, P.-Y.; Yeh, C.-H.; Koshino, M.; Chiu, P.-W.; Suenaga, K. Structural and Chemical Dynamics of Pyridinic-Nitrogen Defects in Graphene. *Nano Lett.* **2015**, *15* (11), 7408–7413. <https://doi.org/10.1021/acs.nanolett.5b02831>.
- (122) Wu, G.; Mack, N. H.; Gao, W.; Ma, S.; Zhong, R.; Han, J.; Baldwin, J. K.; Zelenay, P. Nitrogen-Doped Graphene-Rich Catalysts Derived from Heteroatom Polymers for Oxygen Reduction in Nonaqueous Lithium–O₂ Battery Cathodes. *ACS Nano* **2012**, *6* (11), 9764–9776. <https://doi.org/10.1021/nn303275d>.
- (123) Lin, Y.; Pan, X.; Qi, W.; Zhang, B.; Sheng Su, D. Nitrogen-Doped Onion-like Carbon: A Novel and Efficient Metal-Free Catalyst for Epoxidation Reaction. *Journal of Materials Chemistry A* **2014**, *2* (31), 12475–12483. <https://doi.org/10.1039/C4TA01611D>.
- (124) Li, M.; Liu, W.; Zhang, H.; Liang, Z.; Duan, P.; Yan, X.; Guan, P.; Xu, B.; Guo, J. Direct Imaging of Construction of Carbon Onions by Curling Few-Layer Graphene Flakes. *Physical Chemistry Chemical Physics* **2018**, *20* (3), 2022–2027. <https://doi.org/10.1039/C7CP07063B>.
- (125) Liu, Y.; Kim, D. Y. Enhancement of Capacitance by Electrochemical Oxidation of Nanodiamond Derived Carbon Nano-Onions. *Electrochimica Acta* **2014**, *139*, 82–87. <https://doi.org/10.1016/j.electacta.2014.07.040>.
- (126) Oku, T.; Schmid, G.; Suganuma, K. Formation of Carbon Onions with Pd Clusters in a High-Resolution Electron Microscope. *J. Mater. Chem.* **1998**, *8* (9), 2113–2117. <https://doi.org/10.1039/A802755B>.
- (127) Xiong, D.; Li, X.; Fan, L.; Bai, Z. Three-Dimensional Heteroatom-Doped Nanocarbon for Metal-Free Oxygen Reduction Electrocatalysis: A Review. *Catalysts* **2018**, *8* (8), 301. <https://doi.org/10.3390/catal8080301>.
- (128) Yang, X.-F.; Wang, A.; Qiao, B.; Li, J.; Liu, J.; Zhang, T. Single-Atom Catalysts: A New Frontier in Heterogeneous Catalysis. *Acc. Chem. Res.* **2013**, *46* (8), 1740–1748. <https://doi.org/10.1021/ar300361m>.
- (129) Liang, J.; Jiao, Y.; Jaroniec, M.; Qiao, S. Z. Sulfur and Nitrogen Dual-Doped Mesoporous Graphene Electrocatalyst for Oxygen Reduction with Synergistically Enhanced Performance. *Angewandte Chemie International Edition* **2012**, *51* (46), 11496–11500. <https://doi.org/10.1002/anie.201206720>.
- (130) Wu, Z.; Song, M.; Wang, J.; Liu, X. Recent Progress in Nitrogen-Doped Metal-Free Electrocatalysts for Oxygen Reduction Reaction. *Catalysts* **2018**, *8* (5), 196. <https://doi.org/10.3390/catal8050196>.
- (131) Palkar, A.; Melin, F.; Cardona, C. M.; Elliott, B.; Naskar, A. K.; Edie, D. D.; Kumbhar, A.; Echegoyen, L. Reactivity Differences between Carbon Nano Onions

- (CNOs) Prepared by Different Methods. *Chemistry – An Asian Journal* **2007**, *2* (5), 625–633. <https://doi.org/10.1002/asia.200600426>.
- (132) Tang, C.; Zhang, Q. Nanocarbon for Oxygen Reduction Electrocatalysis: Dopants, Edges, and Defects. *Advanced Materials* **2017**, *29* (13), 1604103. <https://doi.org/10.1002/adma.201604103>.
- (133) Wu, G.; Nelson, M.; Ma, S.; Meng, H.; Cui, G.; Shen, P. K. Synthesis of Nitrogen-Doped Onion-like Carbon and Its Use in Carbon-Based CoFe Binary Non-Precious-Metal Catalysts for Oxygen-Reduction. *Carbon* **2011**, *49* (12), 3972–3982. <https://doi.org/10.1016/j.carbon.2011.05.036>.
- (134) Wanninayake, N.; Ai, Q.; Zhou, R.; Hoque, M. A.; Herrell, S.; Guzman, M. I.; Risko, C.; Kim, D. Y. Understanding the Effect of Host Structure of Nitrogen Doped Ultrananocrystalline Diamond Electrode on Electrochemical Carbon Dioxide Reduction. *Carbon* **2020**, *157*, 408–419. <https://doi.org/10.1016/j.carbon.2019.10.022>.
- (135) Wanninayake, N.; Qianxiang, A.; Thomas, M.; Kodithuwakku, U. S.; Hoque, A.; Guzman, M. I.; Guiton, B.; Risko, C.; Kim, D. Y. Nitrogen and Sulfur Co-Doped Carbon Nano-Onions for Efficient Electrochemical Conversion of Carbon Dioxide. *Meet. Abstr.* **2019**, *MA2019-01* (31), 1591–1591.
- (136) Iijima, S. Direct Observation of the Tetrahedral Bonding in Graphitized Carbon Black by High Resolution Electron Microscopy. *Journal of Crystal Growth* **1980**, *50* (3), 675–683. [https://doi.org/10.1016/0022-0248\(80\)90013-5](https://doi.org/10.1016/0022-0248(80)90013-5).
- (137) Kuznetsov, V. L.; Chuvilin, A. L.; Butenko, Y. V.; Mal'kov, I. Yu.; Titov, V. M. Onion-like Carbon from Ultra-Disperse Diamond. *Chemical Physics Letters* **1994**, *222* (4), 343–348. [https://doi.org/10.1016/0009-2614\(94\)87072-1](https://doi.org/10.1016/0009-2614(94)87072-1).
- (138) Hachtel, J. A.; Idrobo, J. C.; Chi, M. Sub-Ångstrom Electric Field Measurements on a Universal Detector in a Scanning Transmission Electron Microscope. *Advanced Structural and Chemical Imaging* **2018**, *4* (1), 10. <https://doi.org/10.1186/s40679-018-0059-4>.
- (139) Ma, R.; Lin, G.; Zhou, Y.; Liu, Q.; Zhang, T.; Shan, G.; Yang, M.; Wang, J. A Review of Oxygen Reduction Mechanisms for Metal-Free Carbon-Based Electrocatalysts. *npj Comput Mater* **2019**, *5* (1), 1–15. <https://doi.org/10.1038/s41524-019-0210-3>.
- (140) Šljukić, B.; Banks, C. E.; Compton, R. G. An Overview of the Electrochemical Reduction of Oxygen at Carbon-Based Modified Electrodes. *Journal of the Iranian Chemical Society* **2005**, *2* (1), 1–25. <https://doi.org/10.1007/BF03245775>.
- (141) Chen, J.-F.; Mao, Y.; Wang, H.-F.; Hu, P. Theoretical Study of Heteroatom Doping in Tuning the Catalytic Activity of Graphene for Triiodide Reduction. *ACS Catal.* **2016**, *6* (10), 6804–6813. <https://doi.org/10.1021/acscatal.6b01242>.
- (142) Ramaswamy, N.; Mukerjee, S. Fundamental Mechanistic Understanding of Electrocatalysis of Oxygen Reduction on Pt and Non-Pt Surfaces: Acid versus Alkaline Media. *Advances in Physical Chemistry* **2012**, *2012*, 1–17. <https://doi.org/10.1155/2012/491604>.
- (143) Zhang, J.; Xia, Z.; Dai, L. Carbon-Based Electrocatalysts for Advanced Energy Conversion and Storage. *Science Advances* **2015**, *1* (7), e1500564. <https://doi.org/10.1126/sciadv.1500564>.

- (144) Deng, H.; Li, Q.; Liu, J.; Wang, F. Active Sites for Oxygen Reduction Reaction on Nitrogen-Doped Carbon Nanotubes Derived from Polyaniline. *Carbon* **2017**, *112*, 219–229. <https://doi.org/10.1016/j.carbon.2016.11.014>.
- (145) Ohno, S.; Zevalkink, A.; Takagiwa, Y.; Bux, S. K.; Snyder, G. J. Thermoelectric Properties of the $\text{Yb}_9\text{Mn}_{4.2-x}\text{Zn}_x\text{S}_9$ Solid Solutions. *J. Mater. Chem. A* **2014**, *2* (20), 7478–7483. <https://doi.org/10.1039/C4TA00539B>.
- (146) Dresselhaus, M. S.; Chen, G.; Ren, Z. F.; Dresselhaus, G.; Henry, A.; Fleurial, J.-P. New Composite Thermoelectric Materials for Energy Harvesting Applications. *JOM* **2009**, *61* (4), 86–90. <https://doi.org/10.1007/s11837-009-0058-y>.
- (147) Ma, J. M.; Clarke, S. M.; Zeier, W. G.; Vo, T.; Allmen, P. V.; Snyder, G. J.; Kaner, R. B.; Fleurial, J.-P.; Bux, S. K. Mechanochemical Synthesis and High Temperature Thermoelectric Properties of Calcium-Doped Lanthanum Telluride $\text{La}_{3-x}\text{Ca}_x\text{Te}_4$. *J. Mater. Chem. C* **2015**, *3* (40), 10459–10466. <https://doi.org/10.1039/C5TC01648G>.
- (148) Matthes, C. S. R.; Woerner, D. F.; Hendricks, T. J.; Fleurial, J.-P.; Oxnevad, K. I.; Barklay, C. D.; Zakrajsek, J. F. Next-Generation Radioisotope Thermoelectric Generator Study. In *2018 IEEE Aerospace Conference*; 2018; pp 1–9. <https://doi.org/10.1109/AERO.2018.8396738>.
- (149) Bux, S. K.; Blair, R. G.; Gogna, P. K.; Lee, H.; Chen, G.; Dresselhaus, M. S.; Kaner, R. B.; Fleurial, J.-P. Nanostructured Bulk Silicon as an Effective Thermoelectric Material. *Advanced Functional Materials* **2009**, *19* (15), 2445–2452. <https://doi.org/10.1002/adfm.200900250>.
- (150) Bux, S. K.; Fleurial, J.-P.; Kaner, R. B. Nanostructured Materials for Thermoelectric Applications. *Chem. Commun.* **2010**, *46* (44), 8311–8324. <https://doi.org/10.1039/C0CC02627A>.
- (151) Bux, S. K.; Yeung, M. T.; Toberer, E. S.; Snyder, G. J.; Kaner, R. B.; Fleurial, J.-P. Mechanochemical Synthesis and Thermoelectric Properties of High Quality Magnesium Silicide. *J. Mater. Chem.* **2011**, *21* (33), 12259–12266. <https://doi.org/10.1039/C1JM10827A>.
- (152) Holgate, T. C.; Bennett, R.; Hammel, T.; Caillat, T.; Keyser, S.; Sievers, B. Increasing the Efficiency of the Multi-Mission Radioisotope Thermoelectric Generator. *Journal of Electronic Materials* **2015**, *44* (6), 1814–1821. <https://doi.org/10.1007/s11664-014-3564-9>.
- (153) Fleurial, J.-P. Thermoelectric Power Generation Materials: Technology and Application Opportunities. *JOM* **2009**, *61* (4), 79–85. <https://doi.org/10.1007/s11837-009-0057-z>.
- (154) Dresselhaus, M. S.; Chen, G.; Tang, M. Y.; Yang, R. G.; Lee, H.; Wang, D. Z.; Ren, Z. F.; Fleurial, J.-P.; Gogna, P. New Directions for Low-Dimensional Thermoelectric Materials. *Advanced Materials* **2007**, *19* (8), 1043–1053. <https://doi.org/10.1002/adma.200600527>.
- (155) Snyder, G. J.; Christensen, M.; Nishibori, E.; Caillat, T.; Iversen, B. B. Disordered Zinc in Zn_4Sb_3 with Phonon-Glass and Electron-Crystal Thermoelectric Properties. *Nature Materials* **2004**, *3* (7), 458–463. <https://doi.org/10.1038/nmat1154>.
- (156) Snyder, G. J.; Toberer, E. S. Complex Thermoelectric Materials. In *Materials for Sustainable Energy*; Co-Published with Macmillan Publishers Ltd, UK, 2010; pp 101–110. https://doi.org/10.1142/9789814317665_0016.

- (157) Clarke, S. M.; Ma, J. M.; Huang, C.-K.; Allmen, P. A. von; Vo, T.; Kaner, R. B.; Bux, S. K.; Fleurial, J.-P. Optimizing Thermoelectric Efficiency of La₃-XTe₄ with Calcium Metal Substitution. *MRS Online Proceedings Library Archive* **2013**, *1490*, 83–88. <https://doi.org/10.1557/opl.2013.25>.
- (158) Kim, K. T.; Koo, H. Y.; Lee, G.-G.; Ha, G. H. Synthesis of Alumina Nanoparticle-Embedded-Bismuth Telluride Matrix Thermoelectric Composite Powders. *Materials Letters* **2012**, *82*, 141–144. <https://doi.org/10.1016/j.matlet.2012.05.053>.
- (159) Poudel, B.; Hao, Q.; Ma, Y.; Lan, Y.; Minnich, A.; Yu, B.; Yan, X.; Wang, D.; Muto, A.; Vashaee, D.; Chen, X.; Liu, J.; Dresselhaus, M. S.; Chen, G.; Ren, Z. High-Thermoelectric Performance of Nanostructured Bismuth Antimony Telluride Bulk Alloys. *Science* **2008**, *320* (5876), 634–638. <https://doi.org/10.1126/science.1156446>.
- (160) Kim, H.-S.; Kang, S. D.; Tang, Y.; Hanus, R.; Snyder, G. J. Dislocation Strain as the Mechanism of Phonon Scattering at Grain Boundaries. *Mater. Horiz.* **2016**, *3* (3), 234–240. <https://doi.org/10.1039/C5MH00299K>.
- (161) Aldrich, D. E.; Fan, Z. Microstructural Characterisation of Interpenetrating Nickel/Alumina Composites. *Materials Characterization* **2001**, *47* (3), 167–173. [https://doi.org/10.1016/S1044-5803\(01\)00183-8](https://doi.org/10.1016/S1044-5803(01)00183-8).
- (162) Toprak, M.; Zhang, Y.; Muhammed, M. Chemical Alloying and Characterization of Nanocrystalline Bismuth Telluride. *Materials Letters* **2003**, *57* (24–25), 3976–3982. [https://doi.org/10.1016/S0167-577X\(03\)00250-7](https://doi.org/10.1016/S0167-577X(03)00250-7).
- (163) Kim, W.; Zide, J.; Gossard, A.; Klenov, D.; Stemmer, S.; Shakouri, A.; Majumdar, A. Thermal Conductivity Reduction and Thermoelectric Figure of Merit Increase by Embedding Nanoparticles in Crystalline Semiconductors. *Physical Review Letters* **2006**, *96* (4). <https://doi.org/10.1103/PhysRevLett.96.045901>.
- (164) Faleev, S. V.; Léonard, F. Theory of Enhancement of Thermoelectric Properties of Materials with Nano-inclusions. *Phys. Rev. B* **2008**, *77* (21), 214304. <https://doi.org/10.1103/PhysRevB.77.214304>.
- (165) Zhan, G.-D.; Kuntz, J. D.; Mukherjee, A. K.; Zhu, P.; Koumoto, K. Thermoelectric Properties of Carbon Nanotube/Ceramic Nanocomposites. *Scripta Materialia* **2006**, *54* (1), 77–82. <https://doi.org/10.1016/j.scriptamat.2005.09.003>.
- (166) Kim, K. T.; Choi, S. Y.; Shin, E. H.; Moon, K. S.; Koo, H. Y.; Lee, G.-G.; Ha, G. H. The Influence of CNTs on the Thermoelectric Properties of a CNT/Bi₂Te₃ Composite. *Carbon* **2013**, *52*, 541–549. <https://doi.org/10.1016/j.carbon.2012.10.008>.
- (167) Zide, J. M. O.; Vashaee, D.; Bian, Z. X.; Zeng, G.; Bowers, J. E.; Shakouri, A.; Gossard, A. C. Demonstration of electron filtering to increase the Seebeck coefficient in In_{0.53}Ga_{0.47}As/In_{0.53}Ga_{0.28}Al_{0.19}As superlattices. *Phys. Rev. B* **2006**, *74* (20), 205335. <https://doi.org/10.1103/PhysRevB.74.205335>.
- (168) May, A. F.; Toberer, E. S.; Saramat, A.; Snyder, G. J. Characterization and analysis of thermoelectric transport in n-type Ba₈Ga_{16-x}Ge_{30+x}. *Phys. Rev. B* **2009**, *80* (12), 125205. <https://doi.org/10.1103/PhysRevB.80.125205>.
- (169) May, A. F.; Fleurial, J.-P.; Snyder, G. J. Thermoelectric Performance of Lanthanum Telluride Produced via Mechanical Alloying. *Physical Review B* **2008**, *78* (12). <https://doi.org/10.1103/PhysRevB.78.125205>.

- (170) Cheikh, D.; Hogan, B. E.; Vo, T.; Von Allmen, P.; Lee, K.; Smiadak, D. M.; Zevalkink, A.; Dunn, B. S.; Fleurial, J.-P.; Bux, S. K. Praseodymium Telluride: A High-Temperature, High-ZT Thermoelectric Material. *Joule* **2018**, *2* (4), 698–709. <https://doi.org/10.1016/j.joule.2018.01.013>.
- (171) Cheikh, D.; Lee, K.; Peng, W.; Zevalkink, A.; Fleurial, J.-P.; Bux, S. K. Thermoelectric Properties of Scandium Sesquitelluride. *Materials* **2019**, *12* (5), 734. <https://doi.org/10.3390/ma12050734>.
- (172) May, A. F.; Fleurial, J.-P.; Snyder, G. J. Optimizing Thermoelectric Efficiency in $\text{La}_{3-x}\text{Te}_4$ via Yb Substitution. *Chem. Mater.* **2010**, *22* (9), 2995–2999. <https://doi.org/10.1021/cm1004054>.
- (173) Wang, Y.; Chong, X.; Hu, Y.-J.; Shang, S.-L.; Drymiotis, F. R.; Firdosy, S. A.; Star, K. E.; Fleurial, J.-P.; Ravi, V. A.; Chen, L.-Q.; Liu, Z.-K. An Alternative Approach to Predict Seebeck Coefficients: Application to $\text{La}_{3-x}\text{Te}_4$. *Scripta Materialia* **2019**, *169*, 87–91. <https://doi.org/10.1016/j.scriptamat.2019.05.014>.
- (174) Ma, J. M.; Bux, S. K.; Fleurial, J.-P.; Ravi, V. A.; Firdosy, S. A.; Star, K.; Kaner, R. B. High Performance High Temperature Thermoelectric Composites with Metallic Inclusions. US9640746B2, May 2, 2017.
- (175) Lan, Y.; Poudel, B.; Ma, Y.; Wang, D.; Dresselhaus, M. S.; Chen, G.; Ren, Z. Structure Study of Bulk Nanograined Thermoelectric Bismuth Antimony Telluride. *Nano Lett.* **2009**, *9* (4), 1419–1422. <https://doi.org/10.1021/nl803235n>.
- (176) Patterson, J. H.; Herrera, B.; Nelson, G. B.; Steinkruger, F. J.; Matlack, G. M.; Pavone, D. *Long-Term Exposure of $^{238}\text{PuO}_2$ to a Terrestrial Environment*; LA--9487-MS; Los Alamos National Lab., 1982.
- (177) Whiting, C. E.; Du, M.; Felker, L. K.; Wham, R. M.; Barklay, C. D.; Kramer, D. P. Kinetics of the High Temperature Oxygen Exchange Reaction on $^{238}\text{PuO}_2$ Powder. *Journal of Nuclear Materials* **2015**, *467*, 770–777. <https://doi.org/10.1016/j.jnucmat.2015.10.020>.
- (178) Iyore, O. D.; Lee, T. H.; Gupta, R. P.; White, J. B.; Alshareef, H. N.; Kim, M. J.; Gnade, B. E. Interface Characterization of Nickel Contacts to Bulk Bismuth Tellurium Selenide. *Surface and Interface Analysis* **2009**, *41* (5), 440–444. <https://doi.org/10.1002/sia.3046>.
- (179) Schmidt, M.; Siebert, W.; Bagnall, K. W. *The Chemistry of Sulphur, Selenium, Tellurium and Polonium: Pergamon Texts in Inorganic Chemistry*; Elsevier, 2013.
- (180) Greenwood, N. N.; Earnshaw, A. *Chemistry of the Elements*; Elsevier, 2012.
- (181) Marczenko, Z.; Balcerzak, M. Chapter 49 - Tellurium. In *Analytical Spectroscopy Library*; Marczenko, Z., Balcerzak, M., Eds.; Separation, Preconcentration and Spectrophotometry in Inorganic Analysis; Elsevier, 2000; Vol. 10, pp 412–417. [https://doi.org/10.1016/S0926-4345\(00\)80113-3](https://doi.org/10.1016/S0926-4345(00)80113-3).
- (182) Fleer, N. A.; Thomas, M. P.; Andrews, J. L.; Waetzig, G. R.; Gonzalez, O.; Liu, G.-W.; Guiton, B. S.; Banerjee, S. Epitaxial Stabilization versus Interdiffusion: Synthetic Routes to Metastable Cubic HfO_2 and HfV_2O_7 from the Core–Shell Arrangement of Precursors. *Nanoscale* **2019**, *11* (44), 21354–21363. <https://doi.org/10.1039/C9NR07316G>.
- (183) Navrotsky, A.; Mazeina, L.; Majzlan, J. Size-Driven Structural and Thermodynamic Complexity in Iron Oxides. *Science* **2008**, *319* (5870), 1635–1638.

- (184) Martinolich, A. J.; Neilson, J. R. Toward Reaction-by-Design: Achieving Kinetic Control of Solid State Chemistry with Metathesis. *Chem. Mater.* **2017**, *29* (2), 479–489. <https://doi.org/10.1021/acs.chemmater.6b04861>.
- (185) Parija, A.; Waetzig, G. R.; Andrews, J. L.; Banerjee, S. Traversing Energy Landscapes Away from Equilibrium: Strategies for Accessing and Utilizing Metastable Phase Space. *J. Phys. Chem. C* **2018**, *122* (45), 25709–25728. <https://doi.org/10.1021/acs.jpcc.8b04622>.
- (186) Sun, W.; Dacek, S. T.; Ong, S. P.; Hautier, G.; Jain, A.; Richards, W. D.; Gamst, A. C.; Persson, K. A.; Ceder, G. The Thermodynamic Scale of Inorganic Crystalline Metastability. *Science Advances* **2016**, *2* (11), e1600225. <https://doi.org/10.1126/sciadv.1600225>.
- (187) Hudak, B. M.; Depner, S. W.; Waetzig, G. R.; Talapatra, A.; Arroyave, R.; Banerjee, S.; Guiton, B. S. Real-Time Atomistic Observation of Structural Phase Transformations in Individual Hafnia Nanorods. *Nature Communications* **2017**, *8*, 15316. <https://doi.org/10.1038/ncomms15316>.
- (188) De Jesus, L. R.; Andrews, J. L.; Parija, A.; Banerjee, S. Defining Diffusion Pathways in Intercalation Cathode Materials: Some Lessons from V2O5 on Directing Cation Traffic. *ACS Energy Lett.* **2018**, *3* (4), 915–931. <https://doi.org/10.1021/acsenerylett.8b00156>.
- (189) Powell, A. E.; Hodges, J. M.; Schaak, R. E. Preserving Both Anion and Cation Sublattice Features during a Nanocrystal Cation-Exchange Reaction: Synthesis of Metastable Wurtzite-Type CoS and MnS. *J. Am. Chem. Soc.* **2016**, *138* (2), 471–474. <https://doi.org/10.1021/jacs.5b10624>.
- (190) Schaak, R. E.; Mallouk, T. E. Perovskites by Design: A Toolbox of Solid-State Reactions. *Chemistry of Materials* **2002**, *14* (4), 1455–1471. <https://doi.org/10.1021/cm010689m>.
- (191) Bianco, E.; Butler, S.; Jiang, S.; Restrepo, O. D.; Windl, W.; Goldberger, J. E. Stability and Exfoliation of Germanane: A Germanium Graphane Analogue. *ACS Nano* **2013**, *7* (5), 4414–4421. <https://doi.org/10.1021/nm4009406>.
- (192) Cultrara, N. D.; Wang, Y.; Arguilla, M. Q.; Scudder, M. R.; Jiang, S.; Windl, W.; Bobev, S.; Goldberger, J. E. Synthesis of 1T, 2H, and 6R Germanane Polytypes. *Chemistry of Materials* **2018**, *30* (4), 1335–1343. <https://doi.org/10.1021/acs.chemmater.7b04990>.
- (193) Robertson, J. High Dielectric Constant Oxides. *Eur. Phys. J. Appl. Phys.* **2004**, *28* (3), 265–291. <https://doi.org/10.1051/epjap:2004206>.
- (194) Robertson, J.; Wallace, R. M. High-K Materials and Metal Gates for CMOS Applications. *Materials Science & Engineering, R, Materials Science and Engineering R, Materials Science and Engineering R: Reports* **2015**, *88*, 1–41. <https://doi.org/10.1016/j.mser.2014.11.001>.
- (195) Wang, J.; Li, H. P.; Stevens, R. Hafnia and Hafnia-Toughened Ceramics. *J Mater Sci* **1992**, *27* (20), 5397–5430. <https://doi.org/10.1007/BF00541601>.
- (196) Zhao, X.; Vanderbilt, D. First-Principles Study of Structural, Vibrational, and Lattice Dielectric Properties of Hafnium Oxide. *Phys. Rev. B* **2002**, *65* (23), 233106. <https://doi.org/10.1103/PhysRevB.65.233106>.

- (197) Batra, R.; Tran, H. D.; Ramprasad, R. Stabilization of Metastable Phases in Hafnia Owing to Surface Energy Effects. *Appl. Phys. Lett.* **2016**, *108* (17), 172902. <https://doi.org/10.1063/1.4947490>.
- (198) Zhou, B.; Shi, H.; Zhang, X. D.; Su, Q.; Y. Jiang, Z. The Simulated Vibrational Spectra of HfO₂ Polymorphs. *Journal of Physics D Applied Physics* **2014**, *47*. <https://doi.org/10.1088/0022-3727/47/11/115502>.
- (199) Lu, C.-H.; Raitano, J. M.; Khalid, S.; Zhang, L.; Chan, S.-W. Cubic Phase Stabilization in Nanoparticles of Hafnia-Zirconia Oxides: Particle-Size and Annealing Environment Effects. *Journal of Applied Physics* **2008**, *103* (12), 124303. <https://doi.org/10.1063/1.2936983>.
- (200) Kita, K.; Kyuno, K.; Toriumi, A. Permittivity Increase of Yttrium-Doped HfO₂ through Structural Phase Transformation. *Appl. Phys. Lett.* **2005**, *86* (10), 102906. <https://doi.org/10.1063/1.1880436>.
- (201) Tang, J.; Fabbri, J.; Robinson, R. D.; Zhu, Y.; Herman, I. P.; Steigerwald, M. L.; Brus, L. E. Solid-Solution Nanoparticles: Use of a Nonhydrolytic Sol–Gel Synthesis To Prepare HfO₂ and Hf_xZr_{1-x}O₂ Nanocrystals. *Chem. Mater.* **2004**, *16* (7), 1336–1342. <https://doi.org/10.1021/cm049945w>.
- (202) Turquat, C. Structural Investigation of Temperature-Induced Phase Transitions in HfV₂O₇. *The European Physical Journal Applied Physics* **2000**, *10* (April 2000), 15–27. <https://doi.org/10.1051/epjap>.
- (203) Evans, J. S. O. Negative Thermal Expansion Materials. *J. Chem Soc., Dalton Trans.*, **1999**, 3317–3326. <https://doi.org/10.1039/A904297K>.
- (204) Buchanan, R. C. Properties of Hot-Pressed Zirconium Pyrovanadate Ceramics. *Journal of The Electrochemical Society* **1983**, *130* (9), 1905. <https://doi.org/10.1149/1.2120121>.
- (205) Korthuis, V.; Khosrovani, N.; Sleight, A. W.; Roberts, N.; Dupree, R.; Warren, W. W. Jr. Negative Thermal Expansion and Phase Transitions in the ZrV₂-XP_xO₇ Series. *Chem. Mater.* **1995**, *7* (2), 412–417. <https://doi.org/10.1021/cm00050a028>.
- (206) Fleer, N. A.; Pelcher, K. E.; Zou, J.; Nieto, K.; Douglas, L. D.; Sellers, D. G.; Banerjee, S. Hybrid Nanocomposite Films Comprising Dispersed VO₂ Nanocrystals: A Scalable Aqueous-Phase Route to Thermochromic Fenestration. *ACS Appl. Mater. Interfaces* **2017**, *9* (44), 38887–38900. <https://doi.org/10.1021/acsami.7b09779>.
- (207) Fleer, N. A.; Pelcher, K. E.; Nieto, K.; Braham, E. J.; Zou, J.; Horrocks, G. A.; Naoi, Y.; Depner, S. W.; Schultz, B. J.; Amano, J.; Sellers, D. G.; Banerjee, S. Elucidating the Crystallite Size Dependence of the Thermochromic Properties of Nanocomposite VO₂ Thin Films. *ACS Omega* **2018**, *3* (10), 14280–14293. <https://doi.org/10.1021/acsomega.8b02093>.
- (208) Capron, N.; Broqvist, P.; Pasquarello, A. Migration of Oxygen Vacancy in HfO₂ and across the HfO₂/SiO₂ Interface: A First-Principles Investigation. *Appl. Phys. Lett.* **2007**, *91* (19), 192905. <https://doi.org/10.1063/1.2807282>.
- (209) Chen, T.-J.; Kuo, C.-L. Oxygen Vacancy Formation and the Induced Defect States in HfO₂ and Hf-Silicates – A First Principles Hybrid Functional Study. *Microelectronics Reliability* **2014**, *54* (6), 1119–1124. <https://doi.org/10.1016/j.microrel.2013.10.013>.

- (210) Turquat, C.; Leroux, C.; Roubin, M.; Nihoul, G. Vanadium-Doped Hafnia: Elaboration and Structural Characterization. *Solid State Sciences* **1999**, *1* (1), 3–13. [https://doi.org/10.1016/S1293-2558\(00\)80060-6](https://doi.org/10.1016/S1293-2558(00)80060-6).
- (211) Garvie, R. C. The Occurrence of Metastable Tetragonal Zirconia as a Crystallite Size Effect. *J. Phys. Chem.* **1965**, *69* (4), 1238–1243. <https://doi.org/10.1021/j100888a024>.
- (212) Chevalier, J.; Gremillard, L.; Virkar, A. V.; Clarke, D. R. The Tetragonal-Monoclinic Transformation in Zirconia: Lessons Learned and Future Trends. *Journal of the American Ceramic Society* **2009**, *92* (9), 1901–1920. <https://doi.org/10.1111/j.1551-2916.2009.03278.x>.
- (213) Depner, S. W.; Cultrara, N. D.; Farley, K. E.; Qin, Y.; Banerjee, S. Ferroelastic Domain Organization and Precursor Control of Size in Solution-Grown Hafnium Dioxide Nanorods. *ACS Nano* **2014**, *8* (5), 4678–4688. <https://doi.org/10.1021/nm501632d>.
- (214) Ushakov, S. V.; Brown, C. E.; Navrotsky, A. Effect of La and Y on Crystallization Temperatures of Hafnia and Zirconia. *Journal of Materials Research* **2004**, *19* (3), 693–696. <https://doi.org/10.1557/jmr.2004.19.3.693>.
- (215) Parija, A.; Waetzig, G. R.; Andrews, J. L.; Banerjee, S. Traversing Energy Landscapes Away from Equilibrium: Strategies for Accessing and Utilizing Metastable Phase Space. *Journal of Physical Chemistry C* **2018**, *122* (45), 25709–25728. <https://doi.org/10.1021/acs.jpcc.8b04622>.
- (216) Braham, E. J.; Andrews, J. L.; Alivio, T. E. G.; Flier, N. A.; Banerjee, S. Stabilization of a Metastable Tunnel-Structured Orthorhombic Phase of VO₂ upon Iridium Doping. *Physica Status Solidi (A) Applications and Materials Science* **2018**, *215* (16), 1–9. <https://doi.org/10.1002/pssa.201700884>.
- (217) Sun, W.; Kitchaev, D. A.; Kramer, D.; Ceder, G. Non-Equilibrium Crystallization Pathways of Manganese Oxides in Aqueous Solution. *Nature Communications* **2019**, *10* (1), 1–9. <https://doi.org/10.1038/s41467-019-08494-6>.
- (218) Chen, B. R.; Sun, W.; Kitchaev, D. A.; Mangum, J. S.; Thampy, V.; Garten, L. M.; Ginley, D. S.; Gorman, B. P.; Stone, K. H.; Ceder, G.; Toney, M. F.; Schelhas, L. T. Understanding Crystallization Pathways Leading to Manganese Oxide Polymorph Formation. *Nature Communications* **2018**, *9* (1), 2553. <https://doi.org/10.1038/s41467-018-04917-y>.
- (219) Korthuis, V.; Khosrovani, N.; Sleight, A. W.; Roberts, N.; Dupree, R.; Warren, W. W. Negative Thermal Expansion and Phase Transitions in the ZrV_{2-x}P_xO₇ Series. *Chemistry Mater.* **1995**, *7* (2), 412–417. <https://doi.org/10.1021/cm00050a028>.

VITA

MELONIE P. THOMAS

EDUCATION

July 2010 – December 2014	Bachelor of Science, Special Degree in Chemistry (Honors) University of Peradeniya, Sri Lanka
---------------------------------	---

PROFESSIONAL EXPERIENCE

TEACHING EXPERIENCE

Fall 2015 Fall 2016	Graduate Teaching Assistant (Organic Chemistry Laboratory I), University of Kentucky, Lexington, KY, USA
Fall 2015 Spring 2016 Spring 2017	Graduate Teaching Assistant (Organic Chemistry Laboratory II), University of Kentucky, Lexington, KY, USA
January 2015- June 2015	Graduate Teaching Assistant (General Chemistry Laboratory I), University of Peradeniya, Sri Lanka

RESEARCH EXPERIENCE

August 2015 -Present	Graduate Research Assistant , University of Kentucky, Lexington, Ky, USA
-------------------------	--

January
2017-
Present

Advisor: Dr. Beth S. Guiton

Graduate Research Assistant, Center for Nanophase Materials
Sciences, Oak Ridge National Laboratory (ORNL), TN, USA

Advisor: Dr. Beth S. Guiton

Mentors: Dr. Karren L. More, Dr. David A. Cullen

PEER-REVIEWED PUBLICATIONS

1. **M. P. Thomas**,[#] N. Wanninayake,[#] M. De Alwis Goonatilekea, D. Y. Kim,^{*} and Beth S. Guiton^{*}, “Direct Imaging of Heteroatom Dopants in Catalytic Carbon Nano-Onions” Nanoscale,12, 6144 (2020) ^{#denotes equal contribution}
2. M. Olagunju, X. Poole, P. Blackwelder, **M. P. Thomas**, B. S. Guiton, D. Shukla, J. L. Cohn, B. Surnar, S. Dhar, E. Zahran, L. G. Bachas and M. R. Knecht^{*}, “Size-controlled SrTiO₃ nanoparticles photodecorated with Pd co-catalysts for photocatalytic organic dye degradation” ACS Appl. Nano Mater. (2020) *ASAP*
3. L. Yu, B. M. Hudak, A. Ullah, **M. P. Thomas**, C. C. Porter, A. Thisera, R. H. Pham, M. De Alwis Goonatileke and B. S. Guiton^{*}, “Unveiling the Microscopic Origins of Phase Transformations: An *in situ* TEM Perspective” Chemistry of Materials, 32, 2, 639 (2020)
4. S. K. Gupta, J. P. Zuniga, M. Abdou, **M. P. Thomas**, M. De Alwis Goonatileke, B. S. Guiton and Y. Mao^{*}, “Lanthanide-Doped Lanthanum Hafnate Nanoparticles as Multicolor Phosphors for Warm White Lighting and Scintillators” Chemical Engineering Journal, 379,122314 (2020)
5. N. Fleer, **M. P. Thomas**, J. Andrews, G. R. Waetzig, O. Gonzalez, G.-W. Liu, B. S. Guiton^{*} and S. Banerjee^{*}, “Epitaxial Stabilization versus Interdiffusion: Synthetic Routes to Metastable Cubic HfO₂ and HfV₂O₇ from the Core—Shell Arrangement of Precursors” Nanoscale,11, 21354 (2019)

6. J.P. Zuniga, S. K. Gupta, M. Abdou, H. A. De Santiago, A. A. Puretzky, **M. P. Thomas**, B. S. Guiton, J. Liu and Y. Mao*, “Size, Structure, and Luminescence of Nd₂Zr₂O₇ Nanoparticles by Molten Salt Synthesis” Journal of Material Science, **19**, 12411 (2019)
7. L. Yu, R. Han, X. Sang, J. Liu, **M. P. Thomas**, B. M. Hudak, A. Patel, K. Page, and B. S. Guiton*, “Shell-Induced Ostwald Ripening: Simultaneous Structure, Composition, and Morphology Transformations during the Creation of Hollow Iron Oxide Nanocapsules” ACS Nano **12**, 9051 (2018)
8. **M. P. Thomas**, A. Ullah, R. Pham, H. Djieutedjeu, and B. S. Guiton*, “Morphology Controlled Hydrothermal Synthesis of FeS Nanoplatelets”, ACS Crystal Growth and Design (*accepted manuscript*).
9. E. Cali, G. Kerherve, F. Naufal, K. Kousi, D. Neagu, E.I. Papaioannou, **M. P. Thomas**, B. S. Guiton, I.S. Metcalfe, J.T.S. Irvine, and D.J. Payne*, “Exsolved Iridium Nanoparticles on Strontium Titanate for Catalytic Applications”, ACS Applied Materials & Interfaces (*accepted manuscript*)

SIGNIFICANT AWARDS AND HONORS

2019	Outstanding Graduate Student Research Award Department of Chemistry, University of Kentucky
2019	KY NSF EPSCoR Super Collider Outstanding Poster Presentation – Distinction
2018	Dean’s Competitive Graduate Fellowship University of Kentucky, College of Arts and Sciences
2017	Outstanding Oral Qualifier Award University of Kentucky, Department of Chemistry
2017	Oak Ridge Chapter of ASM/Center for Materials Processing Student Night Third place poster in graduate student section